Design and experimental testing of components for the replacement of dangerous radiological sources in geological studies

by

Long Vo

B.S., Kansas State University, 2014

AN ABSTRACT OF A DISSERTATION

submitted in partial fulfillment of the requirements for the degree

DOCTOR OF PHILOSOPHY

Alan Levin Department of Mechanical and Nuclear Engineering
Carl R. Ice College of Engineering

KANSAS STATE UNIVERSITY
Manhattan, Kansas

2020

Abstract

One of the vulnerabilities faced in modern society is the accidental or intentional dispersal of significant quantities of radionuclides into the environment. The term “dirty bomb” refers to a conventional explosive coupled with one or more radionuclides. When detonated, dirty bombs can cause immediate injuries and exposes the intended target as well as bystanders to radiation.

Soon after the terrorist attacks of September 11, 2001, the United States Government commissioned a National Academy of Sciences study to consider the issues of radionuclide sources use. The study reported over 5,000 devices containing nearly 55,000 high-activity radionuclide sources are licensed as of 2008 in the United States. A significant quantity was used for medical applications (e.g. cancer therapy, sterilization, irradiation of blood) and industrial applications (e.g. gauging, well logging for exploration of oil and gas). Among the sources identified as dangerous were ^{137}Cs and Am-Be, primarily used in well logging applications.

In 2014, the National Nuclear Security Administration awarded North Carolina State University (NCSU) a five year $25M grant to develop next generation leaders with practical experience in technical fields related to nonproliferation. The Consortium for Nonproliferation Enabling Capabilities was established. Kansas State University (KSU) is a member CNEC and was studying the replacement of dangerous radiological sources (RDRS) in well logging. RDRS prioritized the search for the replacements or alternative sources in well logging applications. Medical sources stay at fixed facilities and physical security can be enhanced to deter theft. The main objective was to produce experimental data for testing the Monte Carlo Library Least Squares (MCLLS) method. The main objective entailed the constructions of benchmarking test facilities and a prototype tool to collect radiation measurements. Experiments were designed to explore the utility of deuterium-tritium (D-T) accelerators in well logging applications.

Deuterium-tritium (D-T) neutron generators have shown promising utility for oil and gas exploration. Test facilities were constructed for a ThermoFisher B322 D-T accelerator to emit neutrons within a 2500-gallon test chamber. Various materials were placed in the effectively infinite test chamber and around a tube inside the chamber. The tube acted as a borehole containing a prototype logging tool. The prototype collected neutron and gamma interactions with various samples: water, sand, limestone, saline or known mixtures of those materials. The test facilities and the prototype were used to benchmark radiation transport codes. The potential of compact accelerator neutron generators for well logging applications was explored.

Pulsing capability of compact accelerators presented time as a domain for analysis. An experimentally derived parameter $\nu\Sigma_a$ (μs^{-1}) exhibited a nearly linear correlation with hydrogen index (HI) of the contents inside the test chamber. The value $\nu\Sigma_a$ is determined by the macroscopic neutron absorption cross section of the materials inside the test chamber and the neutron speed *v*. The measured apparent decay time constant $\tau_a(\mu s) = \frac{1}{\nu\Sigma_a}$ was found to be free of noise from borehole effects. The measured decay time constant of 2.2 MeV from hydrogen was verified by calculations of the macroscopic cross section for water, sand, and saline samples. The novel approach to derive the macroscopic neutron absorption cross section of a medium from decaying isotopes was introduced in this dissertation. Other factors such as the formation type (composition and density) and salinity (neutron absorber) were also studied. The observations and their significance warranted compact D-T accelerator as a viable alternative for radionuclide sources in well logging. The results in this study also impact non-destructive testing of bulk materials in general.

Design and experimental testing of components for the replacement of dangerous radiological sources in geological studies

by

Long Vo

B.S., Kansas State University, 2014

A DISSERTATION

submitted in partial fulfillment of the requirements for the degree

DOCTOR OF PHILOSOPHY

Alan Levin Department of Mechanical and Nuclear Engineering
Carl R. Ice College of Engineering

KANSAS STATE UNIVERSITY
Manhattan, Kansas

2020

Approved by:

Co-Major Professor
William L. Dunn

Approved by:

Co-Major Professor
Walter J. McNeil

Abstract

One of the vulnerabilities faced in modern society is the accidental and intentional dispersal of significant quantities of radionuclides into the environment. The term “dirty bomb” refers to a conventional explosive coupled with one or more radionuclides. When denotated, dirty bomb causes immediate injuries and exposes the intended target as well as bystanders to radiation.

Soon after the terrorist attacks of September 11, 2001, the United States Government commissioned a National Academy of Sciences study to consider the issues of radionuclide sources use. The study reported over 5,000 devices containing nearly 55,000 high-activity radionuclide sources are licensed as of 2008 in the U.S. A significant quantity was used for medical applications (e.g. cancer therapy, sterilization, irradiation of blood) and industrial applications (e.g. gauging, well logging for exploration of oil and gas). Among the sources identified as dangerous were ^{137}Cs and Am-Be, primarily used in the well logging applications.

In 20014, the National Nuclear Security Administration awarded North Carolina State University (NCSU) a five year $25M grant to develop next generation leaders with practical experience in technical fields related to nonproliferation. The Consortium for Nonproliferation Enabling Capabilities was established. Kansas State University (KSU) is a member CNEC and was studying the replacement of dangerous radiological sources (RDRS) in well logging. RDRS prioritized the search for the replacements or alternative sources in well logging applications. Medical sources stay at fixed facilities and physical security can be enhanced to deter theft. The main objective was to produce experimental data for the Monte Carlo Library of Least Squares (MCLLS) method. The main objective entailed the constructions of benchmarking test facilities and a prototype tool to collect radiation measurements. Experiments were designed to explore the utility of deuterium-tritium (D-T) accelerator in well logging applications.

Deuterium-tritium (D-T) neutron generator showed promising utility for oil and gas exploration. Test facilities were constructed for a ThermoFisher B322 D-T accelerator to irradiate a 2500-gallon test chamber. Various materials were placed in the effectively infinite test chamber and around a tube inside the chamber. The tube acted as a borehole containing a prototype logging tool. The prototype collected neutron and gamma interactions with various samples: water, sand, limestone, saline or known mixtures of those materials. The test facilities and the prototype were used to benchmark radiation transport codes. The potential of compact accelerator neutron generators for well logging applications was explored.

Pulsing capability of compact accelerators presented time as a domain for analysis. An experimentally derived parameter $\nu\Sigma_a$ (μs^{-1}) exhibited a nearly linear correlation with hydrogen index (HI) of the contents inside the test chamber. The value $\nu\Sigma_a$ is determined by the macroscopic neutron absorption cross section of the materials inside the test chamber and the neutron speed *v*. The measured apparent decay time constant $\tau_a(\mu s) = \frac{1}{\nu\Sigma_a}$ was found to be free of noise from borehole effects. The measured decay time constant of 2.2 MeV from hydrogen was verified by calculations of the macroscopic cross section for water, sand, and saline samples. The novel approach to derive the macroscopic neutron absorption cross section of a medium from decaying isotopes was introduced in this dissertation. Other factors such as the formation type (composition and density) and salinity (neutron absorber) were also studied. The observations and their significance warranted compact D-T accelerator as a viable alternative for radionuclide sources in well logging. The results in this study also impact non-destructive testing of bulk materials in general.

Acknowledgements

I would like to thank my mom and brother for the unconditional support during my education pursuit. Thank you Tanya Le and Hai Vo-Le for believing in me when I didn't.

A thank-you to my co-major advisors Dr. Dunn and Dr. McNeil for the continual guidance, the patience, the encouragement, and the overall interest in my professional development.

A thank-you to Dr. Bahadori for the late evenings and early mornings, in the office answering my questions and brainstorming ideas.

Another thank-you to Dr. Vogel for the counsel during my stay at Los Alamos National Laboratory and the continued interest in my development thereafter.

I would like to acknowledge all my colleagues at Kansas State University: Sanchit Sharma, Maria Pinilla, Aaron Hellinger, Diego Laramore, Nathan Hines, and Nathanael Simrl for having their fingerprints on this work.

I would also like to acknowledge my colleagues from NCSU: Vincent DiNoVa and Aaron Feinberg for the collaborations.

Thank you to all the undergraduate students: Alan Reinke, Alexi Rojas, and Ryan Ullrich in supporting the mission.

Thank you to the Environmental Health and Safety, Ronald Bridges and Maria Catanach, for the support.

Lastly, I acknowledge the support of the Consortium for Nonproliferation Enabling Capabilities through North Carolina State University. The CNEC collaboration is funded by the National Nuclear Security Administration through Award DE-NA0002576..

Table of Contents

List of Tables

List of Figures

1 Introduction to Well Logging

What is well logging? The first subsection offers background information regarding the formation of sedimentary rocks and the accumulation of hydrocarbons. The second subsection guides readers through the nuclear methods currently employed by earth scientists and well log analysts. The final subsection details the motivation of RDRS and the objectives of this dissertation.

1.1 Oil and Gas Formations

Hydrocarbons such as methane, propane, and butane are deposited in sedimentary rocks, deep within the earth's crust. There are two theories about hydrocarbons' origin, one organic and one inorganic. The inorganic theory states that hydrogen and carbon form hydrocarbons under extreme pressure and temperature of the earth's subsurface. The most widely accepted theory is the organic theory, which states that hydrocarbons are from plants and animals that were once living on this planet. The organic theory is accepted by more scientists based on the evidence of ancient seas in the earth's crust and at the top of mountains. For example, at the Konza Prairie Biological Station in Manhattan, Kansas, many rocks containing brachiopods, bryozoans, and other marine fossils can be found. These lifeforms lived here about 250 million years ago when the shallow seas covered Kansas during the Permian Period. The fact is that the earth's surface is constantly

changing (e.g., crust movements, weather erosion). As a result, sedimentary rocks are formed containing layers of hydrocarbon deposits.

Besides hydrocarbons, other fluids such as water, saline and air are found inside sedimentary rocks. Typical rock formations that often contain hydrocarbons are shale, dolomite, and sandstone. Inside these formations, fluids naturally separate when not disturbed, forming a column of gas at the top, then liquid at a deeper depth, and finally saline at the bottom. The separation is not uniform and salt domes occur when sedimentary layers are intruded by saline from the bottom, forming a vertical column of salt through the sediments. Most often hydrocarbons are found under impervious salt domes because impervious salt domes act as storage for hydrocarbons. The fluids trapped inside the pores of a formation can be measured and identified. The pore size can be measured by porosity tools. Porosity is the volume of space between aggregate particles per the total volume of the formation. The porosity of formations ranges from 3% to the very rare 40%. Typically encountered porosity is around 20% and these formations are likely recently formed. As formations age, their density increases and the permeability decreases. Figure 1.1 illustrates the cross-sectional area of spherical aggregates inside the test chamber and in cubic packing. The blue represents water occupying the porous space.

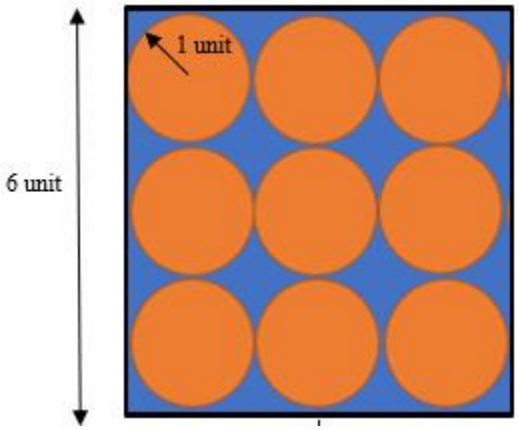

Figure 1.1 Cubic packing in a square tank.

A cubic tank that fits 27 spheres of radius 1 unit perfectly in cubic packing has porosity value of 47.6%. Sometimes porosity is expressed in porosity unit (p.u.) and a porosity unit equals to 1%. The porosity unit *p* for the Figure 1.1 is calculated by the expression

$$p = \frac{V_{tank} - V_{spheres}}{V_{tank}} \times 100\% \quad (1.1)$$

where V_{tank} is the volume of the tank and $V_{spheres}$ is the volume of 27 spheres combined. Because the porous volume is completely filled with water, the 47.6% porosity can be used to quantify the water volume V_{Water} if the spheres' volume $V_{spheres}$ was unknown

$$V_{Water} = 0.476 V_{tank} \quad (1.2).$$

The type of rocks and minerals hosting the hydrocarbons and other fluids affects the mapping and characterization of the formation. For example, the presence of clay or shale alters the hydrogen index (HI) reading of a formation and can result in incorrect porosity estimates. Clay is an alumina silicate, rarely found in pure form, and often contains hydrogen. Hydrogen Index is the measure of the formation's hydrogen density per unit volume compared to water hydrogen density per unit volume. Using the example from Figure 1.1 again as an example for HI calculation (assuming no hydrogen is in the formation matrix or the spheres), the hydrogen density per unit volume H_{bulk} of the tank in Figure 1.2 is

$$H_{bulk} = \frac{f_H \rho_{H_2O} V_{water}}{V_{tank}} = 47.6\% \frac{f_H \rho_{H_2O} V_{tank}}{V_{tank}} \quad (1.3)$$

where f_H is the mass percent of hydrogen in water (11.19%) and ρ_{H_2O} is the density of water (1 g/cc). If the tank did not have any aggregates and is filled with just water, then $V_{water} = V_{tank}$ and the hydrogen density per unit volume H_{H_2O} for that scenario is

$$H_{H_2O} = \frac{f_H \rho_{H_2O} V_{tank}}{V_{tank}} \quad (1.4).$$

The hydrogen index of the tank in Figure 1.1 is then

$$HI = \frac{H_{bulk}}{H_{H_2O}} = 46.7\% \quad (1.5).$$

When the only fluid in the formation is water and the formation is completely saturated with water, then porosity equals HI. In other words, the volume of water added to a tank per tank's volume is HI. Formation pores contain different types of fluid. Porosity unit is a measure of the pore size—not a quantification of fluids within those pores. When the fluid in those pores is a hydrocarbon gas then the HI is very low. In practice, other well measurements such as density and resistivity are used in conjunction to determined hydrocarbon volume. Figure 1.2 display tank with a different aggregate formation, rhombohedral packing 26% porosity. Table lists various packing arrangements and their porosity.

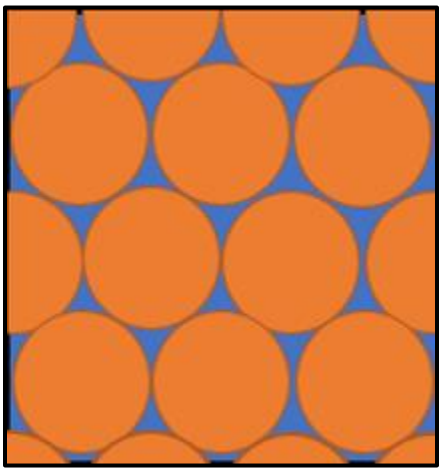

Figure 1.2 Rhombohedral packing in a square tank.

Table 1.1 Packing arrangements and their porosity.

Grain Packing	Porosity (p.u.)
Cubic	47.6
Hexagonal	39.5
Orthorhombic	39.5
Tetragonal	30.2
Rhombohedral	26.0
Triclinic	26.0

The fluid separation in a formation is not perfect so some saline can be trapped in porous layers along with liquid and gas hydrocarbons. The presence of saline strongly affects the nuclear measurements used to map and characterize the hydrocarbon reservoirs because salt has a large thermal neutron capture cross section.. Accurate mapping and characterization of a formation is crucial for a successful extraction. The successful extraction also depends on the permeability factor. Permeability measurements lets well logging scientists know if the hydrocarbons can be extracted from a formation. Knowing the gas, liquid, saline ratio, and the type of formation aids scientists in selecting the right driving force to deliver pressure for the formation. The driving force pumps out hydrocarbons. The correct driving force produces the most hydrocarbons. In practice, reservoirs are complex and analyzing them requires many types of measurements.

There are indirect methods of locating hydrocarbon formations including sonar, gravity, magnetic, and infrared meter. The direct methods of locating hydrocarbons are direct drilling, bright spot seismic signal, core sampling, electronic and nuclear logging. Electronic tools such as those measuring resistivity are largely sensitive to the fluid contents within a formation, but not the mineral types. Data from all the direct and indirect methods are combined to form subsurface

maps in depth and cross-sectional area. A conceptual model is then constructed. The next steps after locating a reservoir are to determine the financial feasibility and to obtain landowner's permission. More general and history information can be obtained from the book by Berger and Anderson [1]. The textbook by Ellis and Singer is an excellent guide for the aspiring earth scientist [2]. The handbook by Serra provides practical information for well logging interpretations [3]. The IAEA provides a handbook of nuclear data for borehole and mineral analysis that is useful for the interpretation of wells [4]. IAEA also published a report on neutron generators and the associated analytical methods [5]. In this dissertation, only nuclear logging is examined. Nuclear logging uses a variety of gamma-ray (denoted by γ), alpha-particle (denoted by α), and neutron (denoted by n) radionuclide sources, which have been deemed dangerous to the public safety.

1.2 Nuclear Measurements in Well Logging

1.2.1 Conventional Gamma Ray Measurements

Fundamentals of nuclear science and engineering is a good textbook and nuclear concepts presented here can be found there [6]. A detection and measurement of radiation guide can be found in a textbook by Tsoulfanadis [7]. Gamma rays have two principles uses in well logging. The first principle use relies on the measurement of natural gamma rays to distinguish shale from non-shale. The second principle use relies on the measurements of an artificial gamma source to infer density and lithology.

1. Distinction between shale or non-shale and estimate of shale volume:

Shale is fine grain sedimentary rocks containing large amount clay minerals. Shale types are identified by the decay of natural radiation from ^{40}K, ^{232}Th, and ^{238}U. Potassium is among the top eight most abundance elements in the earth's crust in percent weight [8]. Minerals containing

potassium are found in many sedimentary rocks. For example, Sylvite has 52.44 weight % potassium and Langbeinite has 18.84 weight % [3]. The decay of the number of radioactive nuclides is expressed in the equation below

$$N(t) = N_o e^{-\lambda t}, \tag{1.6}$$

where *N(t)* is the radiation number of nuclides after time *t* and λ is the decay constant. The number of nuclides at *t=0* is N_o. The half-life of a radioactive source is

$$t_{\frac{1}{2}} = \frac{\ln(2)}{\lambda} \tag{1.7}$$

The half-life of potassium is 1.3×10^9 years. With such a long half-life, the activity of potassium changes very little in measurements collected within hours, days or even months. Activity of ^{40}K, ^{232}Th, and ^{238}U are considered background radiations because they have half-life values in the order 10^9 years.

The measured activity of a radiation source *S* follows Poisson distribution. As the radiation occurrence increases, the Poisson distribution becomes more symmetric. The standard deviation or uncertainty σ of a measurement is the square root of the counts *N* collected by a sensor

$$\sigma = \sqrt{N} \tag{1.8}$$

The expression from equation (1.8) can be written as a percentage of total counts *N* as $\sigma_{\%} = \frac{\sqrt{N}}{N} = \frac{1}{\sqrt{N}}$. Because the total counts detected *N* varies proportionally with time *t* (the duration of the measurement) and source strength *S*, the uncertainty $\sigma_{\%}$ inversely correlates with source strength *S* and measurement time *t*.

$$\sigma_{\%} \propto \frac{1}{\sqrt{St}} \tag{1.9}.$$

2. Lithology and bulk density:

The second use of gamma radiation is for the identification of lithology and bulk density. The ^{137}Cs source is typically employed. The 662 keV gamma rays from ^{37}Cs interact with the rocks via Compton scatter and photoelectric effect. The gamma rays are detected and measured with at least one NaI(Tl) sensor. Electron-rich materials or high-Z materials have larger propensity to attenuate photons via photoelectric effect. The photoelectric index measurement infers the lithology and density by estimating the atomic number (lithology). The count rate detected in the photoelectric effect region is related to both lithology and density. The count rate of Compton scattered gamma rays in the sensor is a function primarily of electron density, which is roughly proportional to physical density.

See Figure 1.3 for the regions of dominance from the three possible interactions. Below the blue line are elements with atomic number less than sulfur (common elements found in earth minerals are below the blue line). The red line represents the gamma energy 662 keV. The probability of interaction for gamma radiations is related to the total mass attenuation coefficient $\frac{\mu(E)}{\rho}$. A parallel beam with 10% of the original intensity passing through a target thickness *x*, without interacting is expressed by the following equation:

$$0.10 = e^{-\mu(E)x} \qquad (1.10).$$

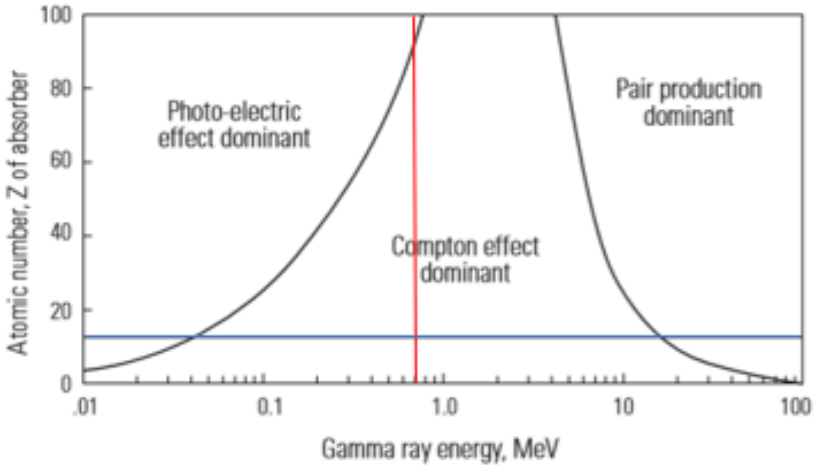

Figure 1.3 Regions of dominance interactions for 662 keV gamma rays. Original source: [9]. Figure adapted from source: [2].

The total mass attenuation coefficients for Z=1 to 92 were published in the reference [10]. For a compound material the linear attenuation coefficient is a sum of mass attenuation coefficients $\left(\frac{\mu(E)}{\rho}\right)_i$ for each constituent, weighted by the constituent's weight fraction ω_i.

$$\left(\frac{\mu(E)}{\rho}\right)_{compound} = \sum \omega_i \left(\frac{\mu(E)}{\rho}\right)_i \quad (1.11).$$

From equation (1.10) and (1.11), density and composition are inferred by the intensity of gamma rays measured from sensor.

Density and lithology of a matrix can be used to infer the porosity p expressed by the following equation

$$p = \frac{V_{pore}}{V_{bulk}} = \frac{V_{bulk} - V_{matrix}}{V_{bulk}} = \frac{V_{bulk} - (\frac{W_{dry}}{\rho_{matrix}})}{V_{bulk}} \quad (1.12),$$

where V_{pore} is the volume of the pore and V_{bulk} is the volume of the bulk formation (rock matrix and fluids in pores). W_{dry} is the dry weight of the rock matrix and ρ_{matrix} is density of the rock matrix. Photoelectric effect and Compton scatter provide the estimates for W_{dry} and ρ_{matrix}.

A parameter called electron density index ρ_e relates bulk density to atomic number is defined as

$$\rho_e \stackrel{\text{def}}{=} 2\frac{Z}{A}\rho_{bulk} \quad (1.13).$$

ρ_{bulk} is the density of the formation matrix and its content. In the absence of pores and water, ρ_e is the same as p_{bulk} because Z/A is roughly 1/2 for most elements other than hydrogen; Thus, for a porous matrix filled with hydrocarbon, ρ_e value deviates from ρ_{bulk}. Table 1.2 below list the most common minerals found in formations and water, along with their values for ρ_{bulk} and ρ_e. Notice the difference between bulk density and electron density index for water but not in the minerals.

Table 1.2 Bulk density and electron density for common mineral and water. Data adapted from source [2].

Name	**Molecular Weight**	$\boldsymbol{\rho_{bulk}}$ **(g/cc)**	$\boldsymbol{\rho_e}$	$\frac{\lvert\boldsymbol{\rho_e - \rho_{bulk}}\rvert}{\boldsymbol{\rho_{bulk}}} \times \mathbf{100\%}$
Calcite ($CaCO_3$)	100.09	2.710	2.708	0.074
Dolomite ($CaCO_3$ $MgCO_3$)	184.42	2.870	2.864	0.209
Quartz (SiO_2)	60.09	2.654	2.650	0.151
Water (H_2O)	18.02	1.000	1.110	11.00

Pair production is another gamma ray interaction, but the threshold is 1,022 keV, above that of 662 keV gamma rays. Pair production is not a mechanism typically used in density and lithology estimates.

1.2.2 Conventional Neutron Measurements

Neutrons interact primarily with nuclei whereas photons interact primarily with electrons. The relevant neutron-nuclei interactions in well logging are elastic scatter, inelastic scatter, and radiative capture. A good description of these interaction types can be found in a textbook reference [11]. New generation logging tools often employ a D-T neutron generator and utilize the neutron-induced gamma rays from inelastic scattering and radiative capture to estimate composition [12]. An assessment was published comparing the alternative technologies to ^{137}Cs for bulk density measurement [13]. The drawback of using D-T for density is that it is not always accurate because of the complex neutron and gamma interactions with matter. Neutrons are typically used for porosity measurements. Because a neutron and a hydrogen nucleus have nearly the same mass, hydrogen nuclei have a propensity to slow down neutrons. The mass of a neutron is 1.0086654 atomic mass unit (u) and the mass of proton is 1.007276 u. The presence of hydrogen-rich materials in a formation strongly affects the energy transfer of neutrons to the formation.

Conventional Am-Be radionuclide sources irradiate the underground and one or two thermal neutron sensor responses are used to estimate the porosity. When two thermal neutron sensors are used, the method is called Compensated Neutron Porosity Logging (CNPL). One thermal neutron sensor is at the "Near" location , in between the neutron source and the "Far" thermal neutron sensor [14]. The distances are measured from the source to the sensor (r_N and r_F correspond to Near and Far distances).The ratio of gross counts between the Near and Far sensors correspond to porosity

$$R = \frac{\Phi_{r_N}}{\Phi_{r_F}} = Ke^{\frac{(r_N - r_F)}{L_M}}, \tag{1.14}$$

where L_M is the migration length and K is a constant approximately equals to r_N/r_F.

In search for Am-Be alternatives, many researchers have studied the response of *R* when coupled with various accelerator-based neutron sources via simulations, e.g. [15], [16], [17]. Others have studied Dense Plasma Focus for material characterization [18]. The simulation studies have unanimously concluded that D-T underperform in neutron porosity tool at Am-Be source-to-sensor distances. D-T neutron generators have been tested in the field as a neutron/density tool [19]. A D-T porosity tool employed epithermal neutron sensors was also reported in [19]. The D-T porosity tool was sensitive to hydrogen index and was not affected by thermal absorber presence. A method to improve the sensitivity of a D-T porosity tool was reported [20]. The performance can also be improved by increasing the source-to-sensor distances in D-T logging tool [21]. However, the longer distances make the tool longer and impair maneuverability in complex wells. The advantages of using D-T are high neutron yield and high neutron energy 14.1 MeV. The high neutron yield significantly reduces the porosity measurement time [15]. High yield enhances the precision of D-T measurement.

The D-D accelerator neutron generator showed great porosity sensitivity in a study, even greater sensitivity than Am-Be [22]. The disadvantages are low neutron yield and low energy 2.2 MeV. Low energy neutron travels smaller distances result in less neutron arriving at the sensors and consequently poor statistics. Poor statistics reduces the precision of D-D. The precision problem is further compounded by the low neutron yield. Nominal yield outputs for D-D and D-T were reported in a study [23]. The nominal yield output for D-T is approximately ×100 more than that of D-D. Table 1.1 lists the power requirement to produce 10^7 neutron per second at two accelerating energy. The lower power requirement for D-T is because of the large probability of interaction. The large probability of interaction 4280 mb at 100 keV results in larger neutron yield for D-T. The D-T reactions produces nominally 2 to 3 orders of magnitude more yield than D-D

[13].The currently available information supports the claim that D-T accelerator neutron generator is a viable alternative to Am-Be radionuclides in neutron porosity logging. In practice, a D-T neutron generator can produce multiple well log parameters [24] e.g. density measurement, porosity, mineralogy, total organic carbon.

Table 1.3 D-D and D-T power requirement to produce 10^7 neutrons per second. Data adapted from source [23].

Incident particle Energy (keV)	D-T Beam Power (Watts)	D-D Beam Power (Watts)
100	0.03	8
150	0.02	5

Absolute elemental composition estimates can be determined with the oxide closure model, published in 1988 by Grau [25]. The oxide closure model is a model for converting prompt neutron induced gamma, "net capture" and "net inelastic-scatter", into the absolute weighted concentrations. The assumption is that the sum of all contributions is near unity and sedimentary rocks are oxides. The oxide closure models must satisfy "net inelastic scatter" and "net capture" yields. The oxide closure model would satisfy the constraints if the model were chosen correctly. A correct model reasonably estimates weight fractions of constituents such as SiO_2, TiO_2, $CaCO_3$. The oxide closure model approach uses only the net counts in the full-energy peaks.

Another method in determining formation characteristics employing neutron is the thermal capture estimate. In this method, thermal neutron capture rate of the formation is related to the formation and its content, such that porosity unit can be derived. The capture rate for sand and limestone are relatively the same and the capture rate for the fluid such as water and hydrocarbon are close to each other. The thermal neutron capture rate for saline is much larger than that of sand,

limestone, and water and the difference correlates with the salt concentration in saline. Much of the research for thermal capture rates have been using neutrons and bulk capture gamma rays to extract porosity [2] [3] [26]. Capture tools have been employed in the well logging industry. The use of D-T generator coupled with a thermal neutron sensor and two gamma sensors was reported in the reference [27]. The tool used under capture sigma principles are often referred to as sigma tools. The authors in the reference used counts in both neutron and gamma-ray sensors to acquire sigma values. Sigma logging provided water saturation measurement that was independent of resistivity (sigma tools are used in cased hole). In open hole, sigma logging when used with resistivity measurement provided salinity estimate. The log of neutron absorption rate provides solution to saturation determination, oil-water contact solution, and detection of gas behind cased hole. Saturation is the measure of water volume per pore's volume S_W and is described in terms of macroscopic absorption cross section Σ_{a} and porosity p

$$\Sigma_{\mathrm{a}} = (1-p)\Sigma_{\mathrm{a\_matrix}} + pS_W\Sigma_{\mathrm{a\_W}} + p(1-S_W)\Sigma_{\mathrm{a\_H}}\,, \tag{1.15}$$

where $\Sigma_{\mathrm{a\_matrix}}$ is the macroscopic cross section for the rock matrix, $\Sigma_{\mathrm{a\_W}}$ is the macroscopic cross section for water, and $\Sigma_{\mathrm{a\_H}}$ is the macroscopic cross section for hydrocarbon. In other words, saturation indicates how much of the porous volume is saturated with water and how much is hydrocarbon.

Fast neutron cross section analysis have been reported in the references [28] and [29]. The focus of this dissertation was on the thermal capture rate of neutron and gamma rays. The novel scientific contribution from this dissertation is the isotopic time dependent analysis, particularly the process of obtaining Σ_{a} via the measured decay time of 2.2 MeV prompt gamma rays from hydrogen. The decay of 2.2 MeV reflects the thermal capture rate of the formation matrix and its

content. Because of the prompt emission, fraction of nanosecond, the time delay causes by observing 2.2 MeV is negligible on the microsecond scale. Knowing the neutron capture rate and intensity of the capture signatures, it is possible to infer information about the borehole environments, e.g. lithology, density, porosity, salinity . Effects of these macroscopic cross section are observed via the decay rate of 2.2 MeV. Experimentally derived macroscopic cross sections are confirmed by calculations of the macroscopic cross section capture for sand, saline, and water samples. The analyses and results are in Chapter 3.

1.3 Motivation

Radionuclide sources have contributed significantly to the advancement of society. Their use in medical imaging e.g. [30], [31], product sterilization e.g. [32], [33], nondestructive testing e.g. [34], [35], and radio-tracing e.g. [36], [37] are but a few examples of the beneficial applications of radionuclides. Some of the attributes that make these radionuclide sources beneficial may also be used for nefarious purposes.

1.3.1 The Replacement of Dangerous Radiological Sources (RDRS)

Following September 11, 2001, nations have reconsidered the wide distribution of dangerous radionuclide sources because of their potential use in radiological dispersal devices or "dirty bombs". The United States National Research Council (NRC) conducted a study to consider the current radionuclide source uses. The result of the NRC study was published in 2008 in a comprehensive report [38]. This report identified two radiological sources, ^{137}Cs and Am-Be, as among the most dangerous due to their widespread use, particularly in well logging. Refer to Table 1.3 for some of the sources identified. NRC reported approximately 5,000 devices containing nearly 55,000 high-activity radiation sources are licensed for use today in the United States.

Table 1.4. Condensed list of dangerous sources identified by the NRC. Data adapted from source: [38].

Radioactive Sources	Half-life (year)	Energy (MeV)	Principal Application	U.S. Inventory (Ci)
^{137}Cs	30.2	0.662 γ	Well Logging	2,800,000
^{60}Co	5.3	1.173, 1.333 γ	Irradiators	198,000,000
^{241}Am	432.2	5.64 α	Well Logging	6,482
^{252}Cf	2.6	2.0 n	Well Logging	7
Am-Be	432.2	5.0 n	Well Logging	N/A

More than 99% of these sources are Cs137, Co60, Am241 and Iridium192. These sources have half-life from ranging from 5 years to 432 years. The radionuclide ^{137}Cs is often made of CsCl, which is highly soluble in water. The ^{137}Cs source is the most important contributor to environmental dose received by human. The high solubility of CsCl increases the water pollution risk significantly if dispersed to the environment. Cesium chloride salt can be easily dispersed in dirty bombs. When in solution, it can be taken up by plants and assimilated by animals because of its chemical similarity to the essential nutrient potassium. ^{137}Cs has a strong tendency to attach to common clay and minerals found in most soil and sediments. ^{137}Cs is used in many density tools in well logging. At the time of this report the U.S has no permanent disposal pathways. Refer to the reference [39] for more information on ^{137}Cs.

The radionuclide ^{241}Am emits 5.49 MeV α particles and 59.5 keV X rays from the daughter ^{237}Np. The alpha particles from americium interact with beryllium and neutrons are produced. Am-Be sources emit neutrons with kinetic energy from thermal to about 10 MeV and mean energy of 4.2 MeV. Am-Be also emits 4.4 MeV gamma rays. Thus, Am-Be sources pose both an internal and external threat to humans. Spectra of neutrons emission for Am-Be and D-T are found in the reference by IAEA [4].

Advancement of accelerators in recent years has brought more attention to their uses. The vigorous efforts are shown by increasingly compact neutron generating accelerator technologies such as D-D and D-T neutron generator. The concept of compact laser-driven sources is being developed by Vogel [40]. Neutron generators and the related analytical methods were summarized in the book published by IAEA [5].

1.3.2 The Objectives:

In 2014, the National Nuclear Security Administration awarded North Carolina State University (NCSU) a five year $25M grant to develop next generation leaders with practical experience in technical fields related to nonproliferation. The Consortium for Nonproliferation Enabling Capabilities (CNEC) was established. One of four thrust areas focused on the Replacement of Dangerous Radiological Sources (RDRS). Kansas State University (KSU) leads the RDRS thrust area within CNEC. Portable and transportable sources of activities greater than 1 Curie were the focus of this study. This leads to a search for ^{137}Cs and Am-Be sources' replacement. Due to their essential functions in medical services and low dispersibility, ^{60}Co and ^{192}Ir sources did not require immediate attention. These sources stay at fixed facilities and increased physical security can deter theft. Toward that direction, the objectives of this dissertation are:

1. to design and construct facilities and a prototype tool that enable studies relevant to the replacement of dangerous radionuclide sources.
2. to design experiments and to collect data that can be used to evaluate methods for replacing dangerous radiological sources.

A well logging prototype was designed and manufactured to collect measurements inside a large 2500-gallon cubic test chamber filled with the following materials: sand, limestone, water,

saline, and known mixtures of those. Water was a surrogate for hydrocarbons. The objective of RDRS is to deliver experimental data to North Carolina State University to benchmark a Monte Carlo Library Least Squares (MCLLS) analysis. MC was utilized to simulate experiments in radiation transport for design and analysis of sensor responses [41] and to solve inverse problems e.g. [42], [43], [44] such as the one here: using MCLLS to determine density and composition of bulk media [45]. The experimental data were also used to benchmark Monte Carlo N-Particle Transport Code (MCNP) and Geant4 simulations. MCNP is a MC-based software package for the simulation of nuclear processes in a user-defined geometry. MCNP is export-controlled and requires permission to use [46]. MCNP was used to design the test facilities and obtain preliminary results. Geant4 is short for GEometry ANd Tracking and it is also a MC-based transport code. Geant4 use is unrestricted [47]. Geant4 was used to simulate sensor responses. Once benchmarked, the simulation codes can produce simulations with various neutron sources. To sum up, the RDRS objectives are to

1. deliver large data sets obtained from facilities developed at KSU to NCSU for MCLLS studies.
2. deliver large data sets for MCNP and Geant4 benchmarking purposes.
3. analyze data to infer the utility of D-T generator sources for oil well logging.

2 Benchmark Facilities and Tool

There are many commercially available nuclear tools. Each has its own proprietary components, calibration, and interpretation algorithms. However, all the tools can be grouped into two major categories based on the use of gamma (density/lithology) or neutron (e.g. porosity, lithology, sigma tools). The main difference between the two categories are the type of sources and sensors used. The prototype logging tool was designed and constructed with the intention to study the fundamentals involving the density and porosity measurements. The prototype tool needed to be versatile in design for ease of exchanging various components (different type of sources and sensors) and various configurations (source-to-sensor distances). Test facilities were constructed to experiment with the tool. Section 2.1 details the construction of the benchmark facilities, description of the samples and the experimental procedure. Section 2.2 details the construction of the benchmarking tool including source description, the data acquisition system, and sensors.

2.1 Benchmark Facilities

The facilities were designed and constructed with the emphasis on:

1. Creating a safe testing environment
2. Creating infrastructure that produces high quality, comprehensive, repeatable data sets

3. Incorporating a large level of flexibility that would maximize the scientific reach and impact

A shielding plan was created and implemented at the facilities. The shielding plan was reviewed by the Environment Health and Safety services and approved by the State of Kansas. The plan allowed radiation workers to operate the D-T neutron generator without dosimetry even when the test chamber is empty. Refer to reference [48] for Pinilla's design study of the facilities. Working spaces included: the experimental room (room 107), and the control room (room 101), a storage unit (room 106), and a staging area/loading dock (room 102). Refer to Figure 2.1 for the facilities layout. The experiments were set up in room 107 but the control and manipulation of the equipment were executed in room 101, a safe distance away from the neutron sources where personal dosimetry was not necessary.

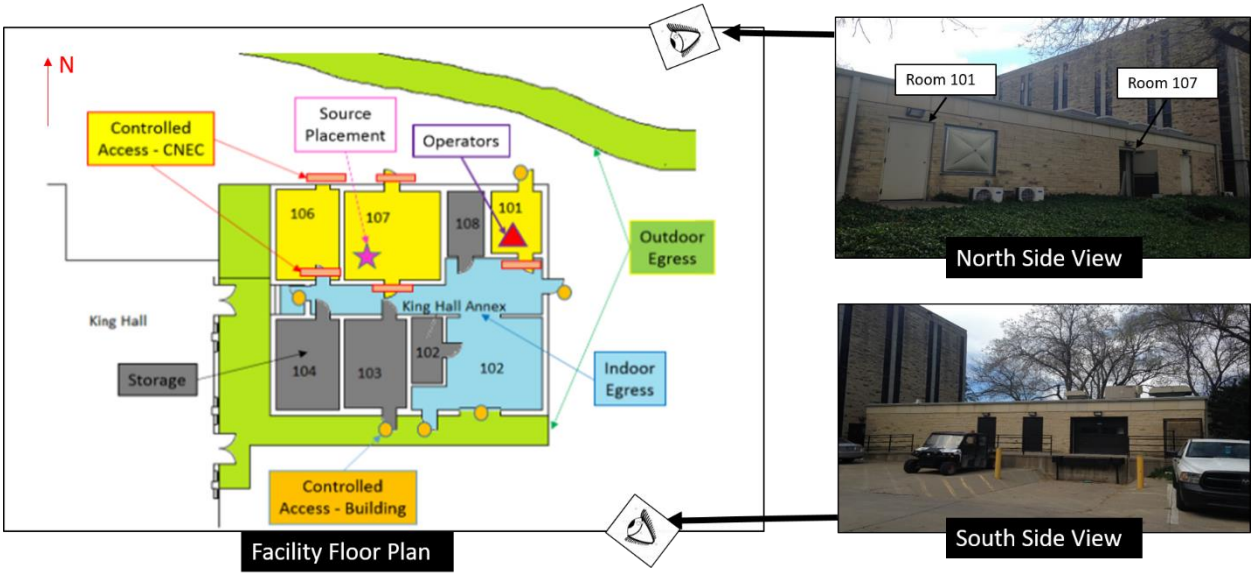

Figure 2.1 Facilities layout.

Small 20-ounce samples of each experiment's material were stored in room 106, along with job tools and back-up electronic equipment. Sand and limestone samples are loaded from the loading dock on the South side of room 102, as seen in Figure 2.2. The aggregates were loaded

onto conveyor belt system and the system moves the aggregates from the loading dock through the facilities and into the test chamber. Water and saline samples are taken from a tap water source and salt was added to the tap water to create a saline solution. The saline solution was kept near homogenous by water pumps constantly mixing until the experiment begins. A large heavy-duty vacuum truck was used to remove the wet aggregates at the end of an experiment. For water and saline samples, the test chamber drain valve allowed for easy removal of the liquid samples.

Figure 2.2 Loading area for sand and limestone.

The experimental room houses a test chamber, a diagram of which is shown in Figure 2.3. MCNP was used to estimate the effectively infinite volume of various bulk media and lead to the present dimension of the test chamber. The test chamber is open at the top for sample loading. An aluminum pipe centers horizontally through the tank, and the pipe representing a borehole wall. The chamber held mixtures of sand, limestone, water, and saline. Pumps were used to ensure the fluid samples were homogenous. The tool collected measurements from inside the aluminum pipe. The test chamber, when filled, simulates an underground environment for the well logging applications.

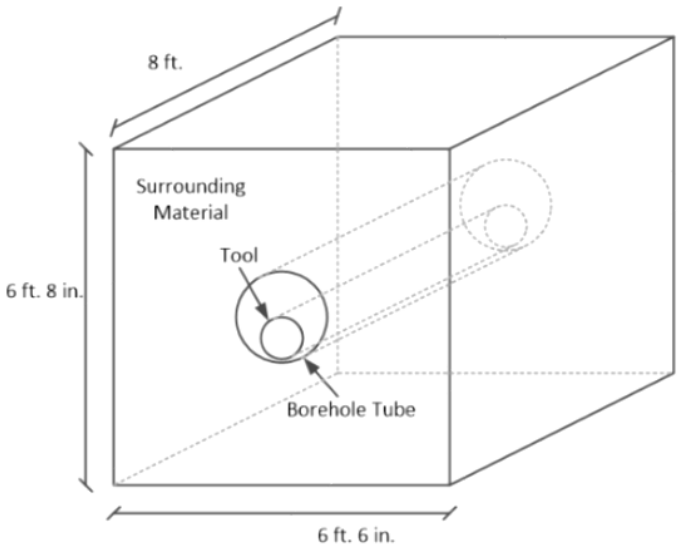

Figure 2.3 Large 2500-gallon test chamber.

The experimental room has a half-ton crane, shown in Figure 2.4 right . The half-ton crane can move heavy equipment from outside to inside the test chamber. The borehole has a cap that can be seen in Figure 2.5 left. the cap was made from borated polyethylene to prevent direct neutron streaming the entrance shown in Figure 2.4 right. Large slabs of borated polyethylene and plastic were also installed on the opposite end of the borehole to prevent direct neutron streaming into the hallway.

Figure 2.4 The experimental room contains the test chamber.

The aluminum borehole pipe is visible when the test chamber is empty. The pipe can be seen in Figure 2.5 right. The borehole tube is made from aluminum and is suspended at the center of the test chamber. The tube is watertight. Liquids can be drained from the test chamber by a valve located at the bottom of the chamber.

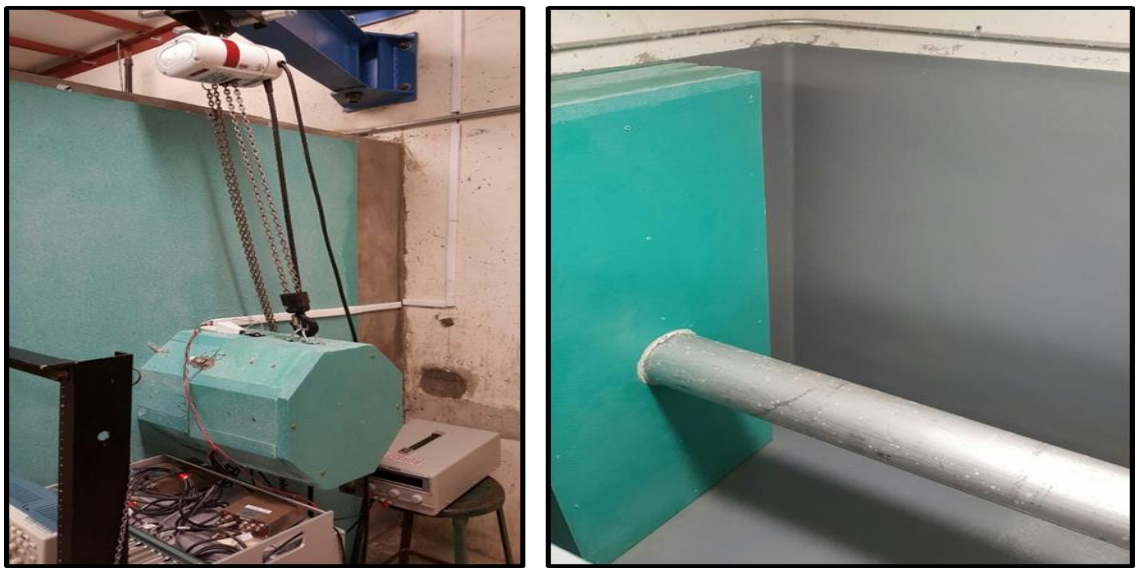

Figure 2.5 Borehole cap (left) and inside the test chamber (right).

The filling procedure was to:

- Fill the tank with sand
- Collect measurements for “Nearly dry sand”
- Add water into the sand. The amount of water added was recorded in percentage of the test chamber total volume (15% for first sand-water mixture experiment). This is the “Partially Saturated Sand” experiment
- Collect measurements with sand at 15% moisture, in which only the bottom half of chamber had water.
- Add more water in to sand and filled to 30%. The is the “Fully Saturated Sand” experiment.

- Collect measurement with sand at 30% moisture.

The filling procedure was similar for limestone except that the limestone did not have a measurement where only half of the tank was filled with water. The two limestone experiments were nearly dry state or fully saturated state. All samples were considered semi homogenous except for the "Partially Saturated Sand" experiment, where sand was at 15% moisture (abbreviated Sand(15%)) as indicated in Table 2.1. In that experiment, only the bottom half of the test chamber had water. The experimental scenarios were under normal conditions of one atmosphere and controlled temperature of 70 Fahrenheit. In the field, formations are complex and are exposed to extreme pressure and temperature. In Chapter 1, it was concluded that HI and porosity were the same for a homogenous rock matrix filled with water. The amount of water added to the samples in listed Table 2.1 was used to calculate the porosity of the test chamber. Moisture content added to the tank was recorded in Table 2.1 as percent volume so it can be considered as HI or porosity.

Table 2.1 Experiments overview

Experiment	Homogeneous sample (y or n)	Moisture content (%volume)	Density (g/cc)	Measurement Time (s)
Nearly Dry Sand	y	~0	1.6	3,259.983
Nearly Dry Limestone	y	>0	2.5	3,259.985
Partially Saturated Sand	n	15	1.7	3,259.753
Fully Saturated Sand	y	30	1.8	3,259.984
Fully Saturated Limestone	y	63	3.2	3,259.986
Water	y	100	1	3,259.975
Saline (3.6%wt)	y	~100	1.04	3,259.754
Saline(7.2%wt)	y	~100	1.07	3,259.982

The facilities and all equipment were controlled at a safe distance from the neutron sources, in the control room 101. The control room features were:

1. Video surveillance,
2. Two-way audio,
3. Warning lights throughout facilities,
4. Enabling switch, and
5. Instant kill switches at entries,

Visual and audio connections between the experimental and control room prevented inadvertent entries. Inside the control room is the operator's station where all activities within the facilities can be monitored. The facilities features are manipulated from the operator station, as shown in Figure 2.6. The prototype tool and the generator are each manipulated on a dedicated computer.

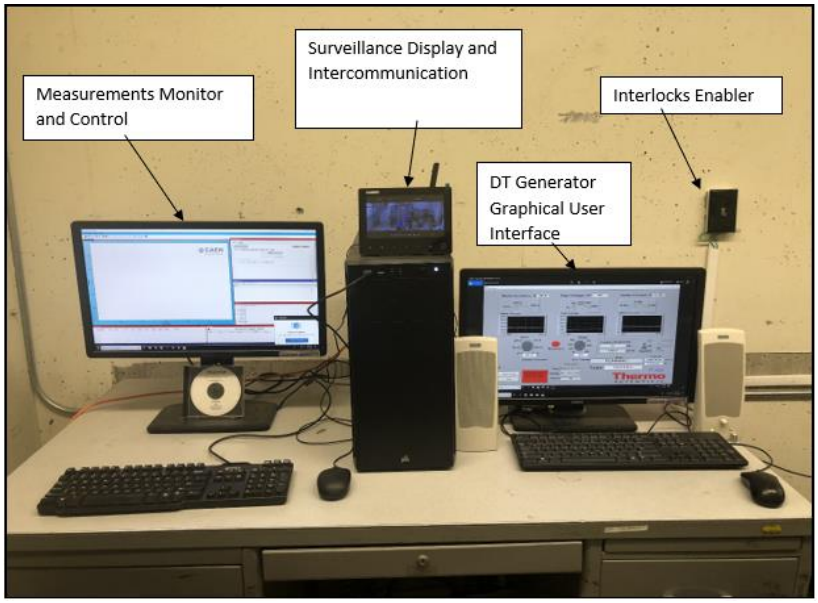

Figure 2.6 Operator's working station.

To begin an experiment, the interlocks enabler must be actuated; All doors must be closed, and the borehole cap must be in place. Risk from inadvertent entries is mitigated by having instant kill switches on all doors into the experimental room. The electrical circuit was designed such that if any door were opened at any time during the experiment, the generator shut off and halt neutron production. A procedure was drafted for the experiments. The steps in the procedure are listed below, in chronological order:

- 1st Calibration (duration: 5 min)
- Pre-Background (duration: 120 min)
- 2nd Calibration (duration: 5 min)
- Live-DT Measurement (duration: 60 min)
- 3rd Calibration (duration: 5 min)
- Post-Background (multiple measurements)

2.2 Benchmark tool

The tool sensors and source were housed within a five-inch diameter tube made of aircraft-grade aluminum 6061. The outer housing tube was made to enclose the skeleton internal structure. The skeleton is shown in Figure 2.7. The tool skeleton was also made from the same aircraft-grade aluminum. The outer housing of the tool was not used at the facilities for ease of on-the-flight adjustments. The dimensions in Figure 2.7 were measured from the target of the D-T neutron generator.

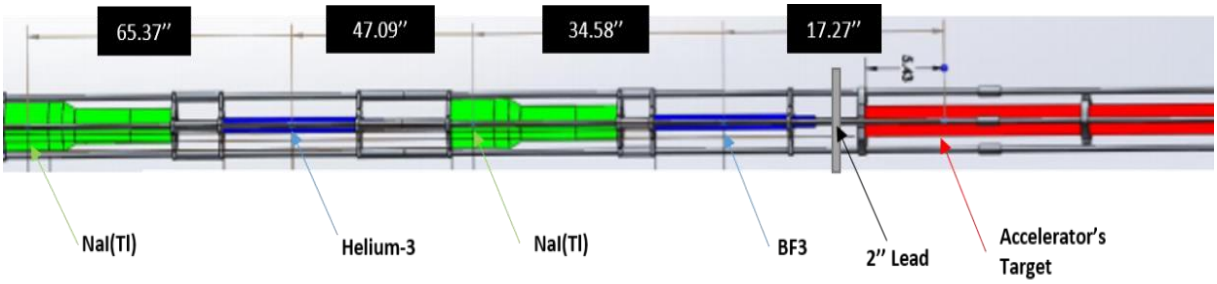

Figure 2.7 The SolidWorks model shows the tool skeleton with its components exposed

The tool was 7 ft long with the neutron generator installed. The sensors and source are cylindrical and placed concentric along a common axis. The sensors and source were held in place by brackets on four railings equally spaced from the said common axis. The earth's extreme underground pressure and temperature limit the selections of sensors. Commonly used thermal neutron sensors are ^{3}He gas-filled counters but their supply is limited. A BF_3 sensor was studied along with the ^{3}He sensor. For gamma rays, the standard NaI(Tl) sensor was chosen for this study. The needs for new well logging sensors were discussed in reference [49]. Some examples of geochemical commercial tools with newer gamma sensor technologies are tabulated in Table 2.2. These new tools utilize high-resolution sensors $LaBr_3$ and BGO.

Table 2.2 Commercial geochemical tools

	FLeX [50]	**GEM** [51]	**Litho Scanner** [12]
Company	**Baker Hughes**	**Halliburton**	**Schlumberger**
Introduction year	2006	2009	2012
Neutron source	PNG	Am-Be	PNG
Diameter	4.9 in	4.8 in	4.5 in
Sensor	3-in BGO	3-in BGO	$LaBr_3$
Capture elements	Ca, Cl, Fe, Gd, H, Mg, S, Si, Ti	Ca, Cl, Fe, Gd, H, Mg, S, Si, Ti	Ca, Cl, Fe, Gd, H, Mg, Na, S, Si, Ti

$LaBr_3$ and BGO sensors are newer technologies compared to NaI(Tl) sensors. They were studied in Hou's dissertation for well logging applications [52]. $LaBr_3$ and BGO have some advantages over NaI(Tl), e.g. better energy resolution, higher density. $LaBr_3$ was a very attractive option and its light yield was constant over a wide range of temperature. The minor drawbacks were that $LaBr_3$ is radioactive itself and expensive. Performance for various inorganic scintillators were reviewed in the reference [53]. The review of BGO showed that its light yield deteriorates more than that of NaI(Tl) as a function of increasing temperature.

NaI(Tl) sensors were standardized and affordable. They perform better under extreme temperature. NaI(Tl) crystals can be grown into large sizes and shapes. For these reasons, the NaI(Tl) sensors were chosen as gamma spectrometers for the prototype. Though NaI(Tl) has good efficiency and light yield, the material lacks in energy resolution. The lower energy resolution of NaI(Tl) was suitable for preliminary studies of the inverse MCLLS approach. The lower resolution made it relatively simpler to fit variables to the entire spectrum. High resolution sensors produced more distinguishable peaks. High resolution sensors enable estimates of elemental atomic density.

Mitra has published a method to correct temperature dependence of pulse height collection in NaI(Tl) sensors. Experimental spectra studied at one temperature may be shifted to represent the same spectra at another temperature [54]. The temperature shift method could be used to explore what the NaI(Tl) response would be like in extreme temperature without actual tests.

Activation of the sensors contribute to the result and need to be accounted for. Activation of NaI(Tl) sensors has been studied, e.g. [55], [56]. From the reference, Ellis investigated a large NaI(Tl) sensor 50×100×100 mm crystal enclosed in 0.8 mm thick aluminum housing. Ellis listed the NaI(Tl) activation signatures with their decay mode and the subsequent γ rays released, Table 2.3.

Table 2.3 Activation of the NaI(Tl) sensors. Data adapted from [55]

Component	Reaction	Decay Mode	Threshold (keV)	Half-life	γ rays (keV)
Scintillator	$^{127}I(n,\gamma)^{128}I$	β-	None	24.99 min	442.9
Scintillator	$^{23}Na(n,\gamma)^{24}Na$	β-	None	14.96 h	1368.6 2754.0
Casing	$^{27}Al(n,\gamma)^{28}Al$	β-	None	134.5 s	1778.9
Casing	$^{27}Al(n,p)^{28}Al$	β-	1896.31	9.46 min	843.8 1014.5

Iodine was the most significant contributor to the activation. Minor contributions were observed from sodium and thallium. The sodium contribution persists for a longer time than the iodide contribution and can accumulate over multiple irradiations. A significant contribution from the aluminum casing was observed (approximately one fifth of iodide) via two mechanism, one with half-life of 9 minutes and the other 134.5 seconds. Aluminum was a major element in sensors' casings, the prototype structure, and the borehole wall—all of which might be problematic in high pulse repetitions.

2.2.1 ThermoFisher B322 D-T Pulsed Neutron Generator

Two mobile and compact neutron sources were available for testing: one Am-Be source and one ThermoFisher B322 D-T pulsed neutron generator (PNG). Figure 2.8 exhibits a picture of the Am-Be source. This source was used in preliminary studies for the development of MCNP codes. For result regarding Am-Be simulations and experiments refer the reference [57].

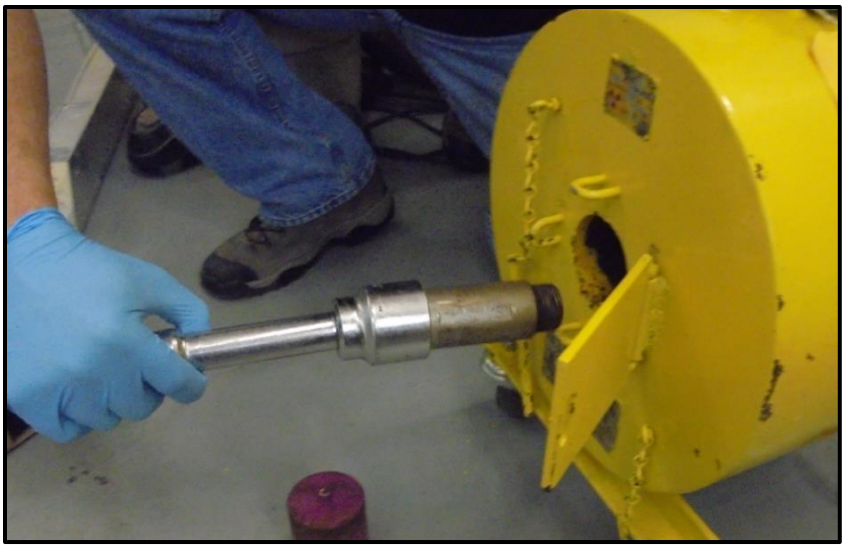

Figure 2.8 The 5 Ci Am-Be source going out of the lead container.

The D-T generator produces up to 1×10^9 neutrons per second, with a pulse repetition frequency of 1kHz and a 10% duty cycle. The generator contains an accelerator labeled as "161DT". The outer housing of the accelerator was filled with sulfur hexafluoride to 110 psig after it was delivered to KSU. Shipping with high pressure gas was prohibited. The accelerator housing was cylindrical, with 2-inch diameter and 40-inch length. A direct current supply of 200 V and 24 μA powered a control board that communicated with the accelerator and a computer. The control board on the left of Figure 2.9 drove the voltage and current to the generator. The computer sends a message that lets operator knows when the generator is online. Once online, the generator is ready to produce neutrons. The accelerator settings were set to 40 kV and 40 μA. The neutron yield for the experiments here were approximately 1×10^6 neutrons per second.

Figure 2.9 The B322 PNG with the control board attached

The neutron flux at 100 cm radially from the target was calculated by ThermoFisher using MCNP and the radial flux is shown in Figure 2.10. The flux was normalized at 90º to the direction of the deuteron's acceleration. The 0º direction was the direction toward the sensors and the 180º direction was away from the sensor.

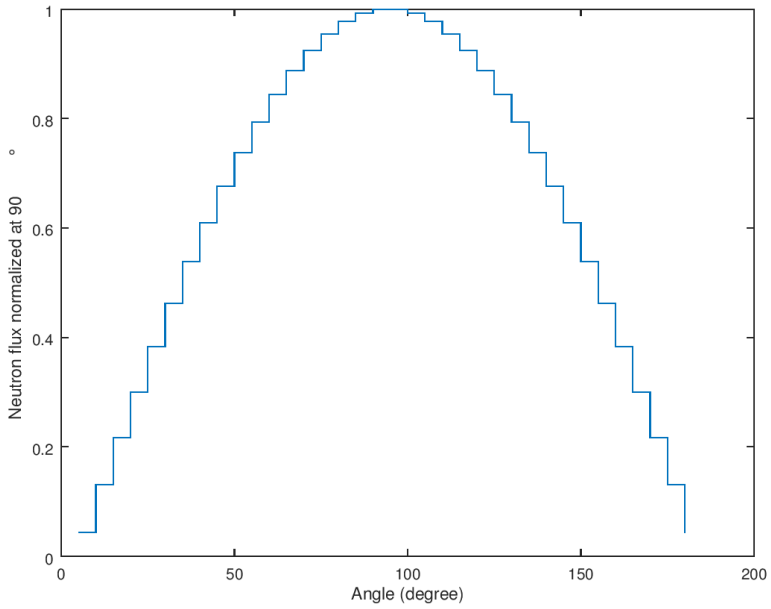

Figure 2.10 Neutron flux at 100 cm away from the target, normalized at 90º

The neutron generator was controlled via the ThermoFisher Graphical User Interface (GUI) software. The GUI window captured from a computer screen is shown in Figure 2.11. When the

experiment begins, the generator takes approximately 45 seconds to create the first neutron pulse. At 55 seconds into the experiment, stable neutron yield is observed. The indicator of stable neutron yield was observed through beam current variation. The GUI displays three real-time windows that show the beam current, the high voltage, and getter current reading. The beam current vs. time plot offers an indication of the ion beam stability, which is directly related to the neutron yield stability. The accelerator was driven by a Siglent waveform generator, which has two outputs. One output sends a signal to the accelerator to initiate neutron pulses and the other output simultaneously sends a signal to a CAEN DT5730 digitizer to record a time stamp for the start of each neutron pulses. The generator can only be operated at 1 kHz and 10% duty cycle, hence, the Siglent waveform generator delivered driving pulses of 1kHz frequency and pulse duration of 100 μs. The signal collection and processing components are described in the detail in the next section.

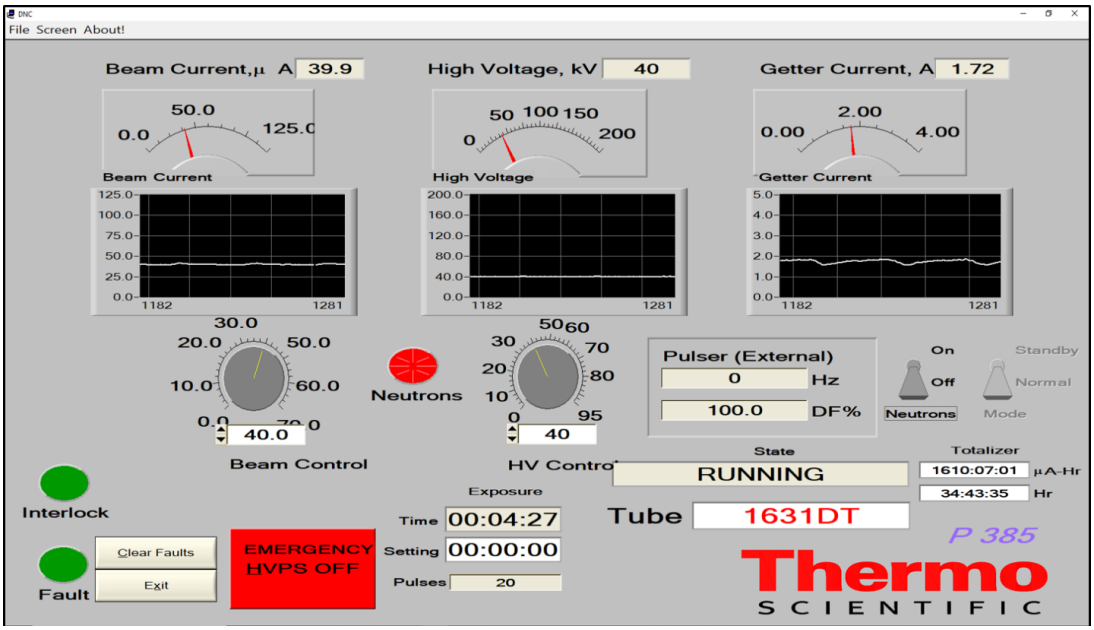

Figure 2.11 ThermoFisher DNCII graphical user interface for the D-T PNG.

The generator produced neutrons for 60 minutes during each experiment. The 60-minute duration was called the "Live-DT Measurement". The total allotted time for each measurement

was more than five hours. The experimental procedure allotted time for calibrations and background measurements. The steps in the procedure are listed below, in chronological order:

- 1st Calibration (duration: 5 min)
- Pre-Background (duration: 120 min)
- 2nd Calibration (duration: 5 min)
- Live-DT Measurement (duration: 60 min)
- 3rd Calibration (duration: 5 min)
- Post-Background (multiple measurements)

2.2.2 The Data Acquisition

The NIM voltage supply, shaping time and gain for each sensor were important for sensor calibration and are listed in Table 2.4. The module settings were never changed. The fine gain was adjusted digitally via the Multichannel Analyzer (MCA) software to position the 1.28 MeV peak at channel 260 out of 2,048 channels for every single experiment.

Table 2.4. NIM bin module settings.

	Near NaI(Tl)	**Far NaI(Tl)**	**Near BF_3**	**Far ^3He**
Voltage supply (V)	690	520	1690	1150
Shaping time (μs)	0.5	0.5	1	1
Module Gain (x)	1.6	1.3	10	10

The NIM components produced analog signals from radiation events. The analog signals were sent to a CAEN DT5730 MCA digitizer. The digitizer integrated the signal and produced a

corresponding channel value for pulse height. The pulse height values corresponded to energies of the incident radiations. The check source of ^{22}Na emits gamma radiation of known energies at 511 keV and 1.28 MeV and these known energies were used to calibrate the sensors. The calibration is plotted in Figure 2.12 for the Near and Far NaI(Tl) sensors. Other known energies such has 2.2 MeV from hydrogen prompt capture, 1.46 MeV natural gamma from potassium, and 6.1 MeV inelastic scatter gamma from oxygen were used in the calibration plot shown in Figure 2.12.

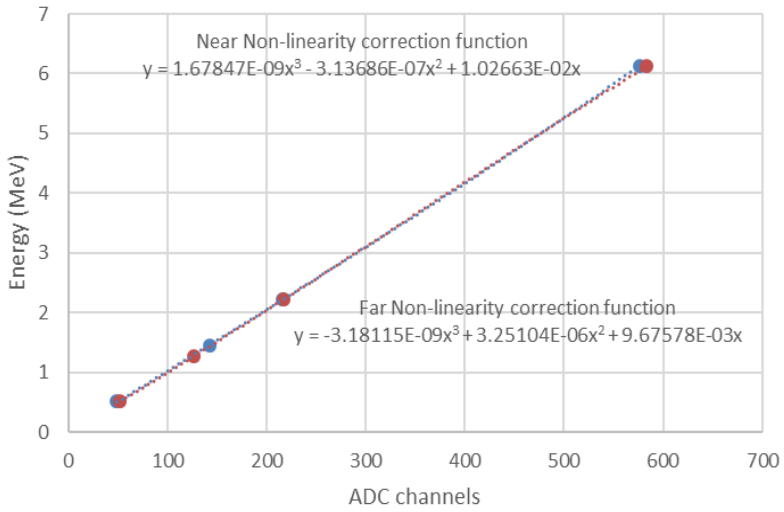

Figure 2.12 Non-linearity energy correction functions for the Near and Far sensors

The response of the Near NaI(Tl) detector with and without the non-linear correction were plotted and shown in Figure 2.13. A linear channel to energy function was applied to the blue normalized at 511 keV. The red plot used the non-linear correction from Figure 2.12.

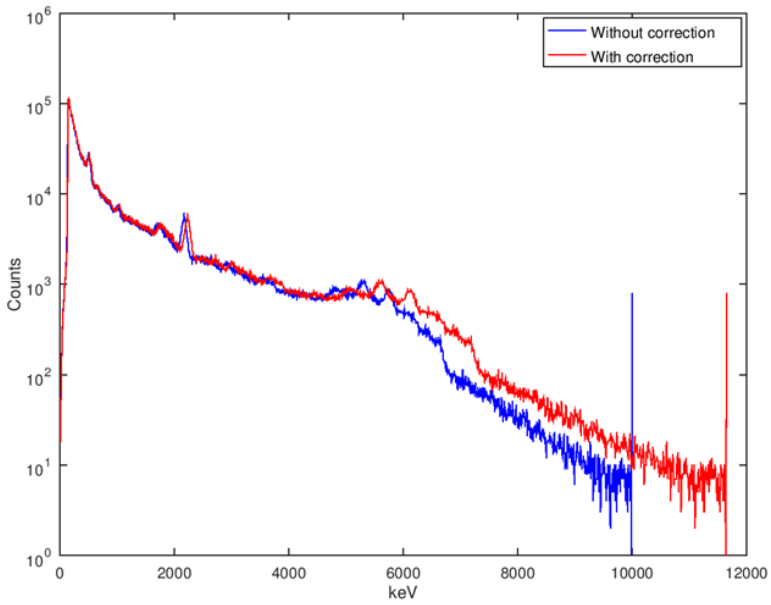

Figure 2.13 Near NaI(Tl) responses with and without non-linear correction.

Besides energy, the digitizer also recorded the detection time. For every radiation event, a timestamp was generated along the event's pulse height. This operating mode is called list mode. The digitizer can save waveforms for each incident radiation for post-processing, but this feature was not necessary for this work. If a dual-particle sensor were used, the waveforms would be beneficial in discriminating the particles. The waveform outputs contained the most information about the radiation events collected whereas list mode only returns pulse height and timestamp. The waveforms and pulse heights can be recorded every 2 ns or at a frequency of 500 MHz.

The digitizer can process up to eight channels simultaneously. Four channels were occupied by the neutron and gamma sensors. The fifth channel was occupied by a Siglent waveform generator. This fifth channel recorded the reference timestamp for each D-T neutron pulse. The Siglent waveform generator had two outputs. One output (square pulse) went to the D-T generator to initiate neutron pulses and the other output (tail pulse) went to the digitizer to record

the timestamp of those pulses. This setup creates a reference time for the induced events. The time an event registered in a sensor can be referenced to the time a neutron pulse was created.

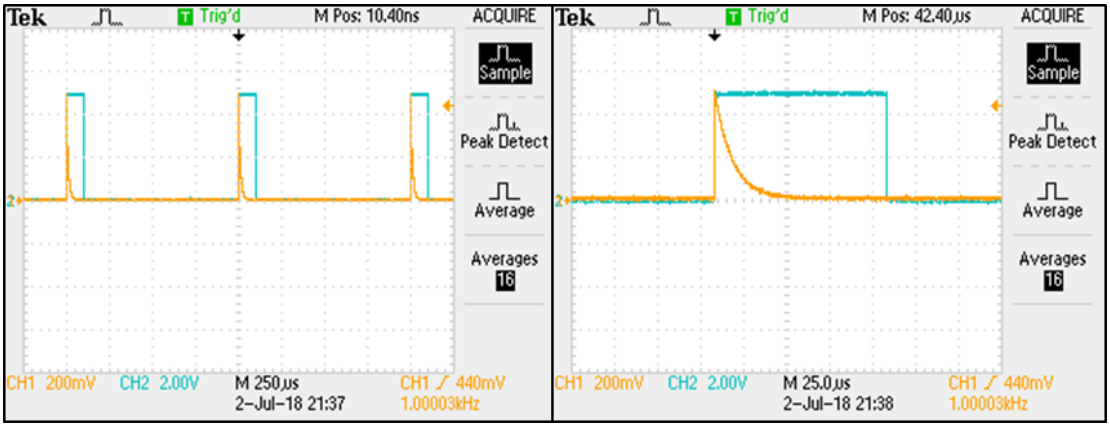

Figure 2.14 Siglent waveform generator outputs as seen on oscilloscope. Left: oscilloscope display shows the repetitions occurring at 1,000 µs. Right: oscilloscope display shows the timestamp was placed at the start of the neutron pulse.

The two Siglent waveforms can be viewed in Figure 2.14. The left oscilloscope display shows the two signals repeated three times on a 250 µs grid. The right oscilloscope display shows a square pulse and a tail pulse on a 25 µs grid. The teal signal (square pulse) persisted for 100 µs then ceased for the next 900 µs. The orange signal (tail pulse) was logged into the digitizer as the time the neutron pulse was initiated. The two signals were always within 20 ns of each other. The tail pulse trails the square pulse by 20 ns. The entire data acquisition scheme is shown in Figure 2.15.

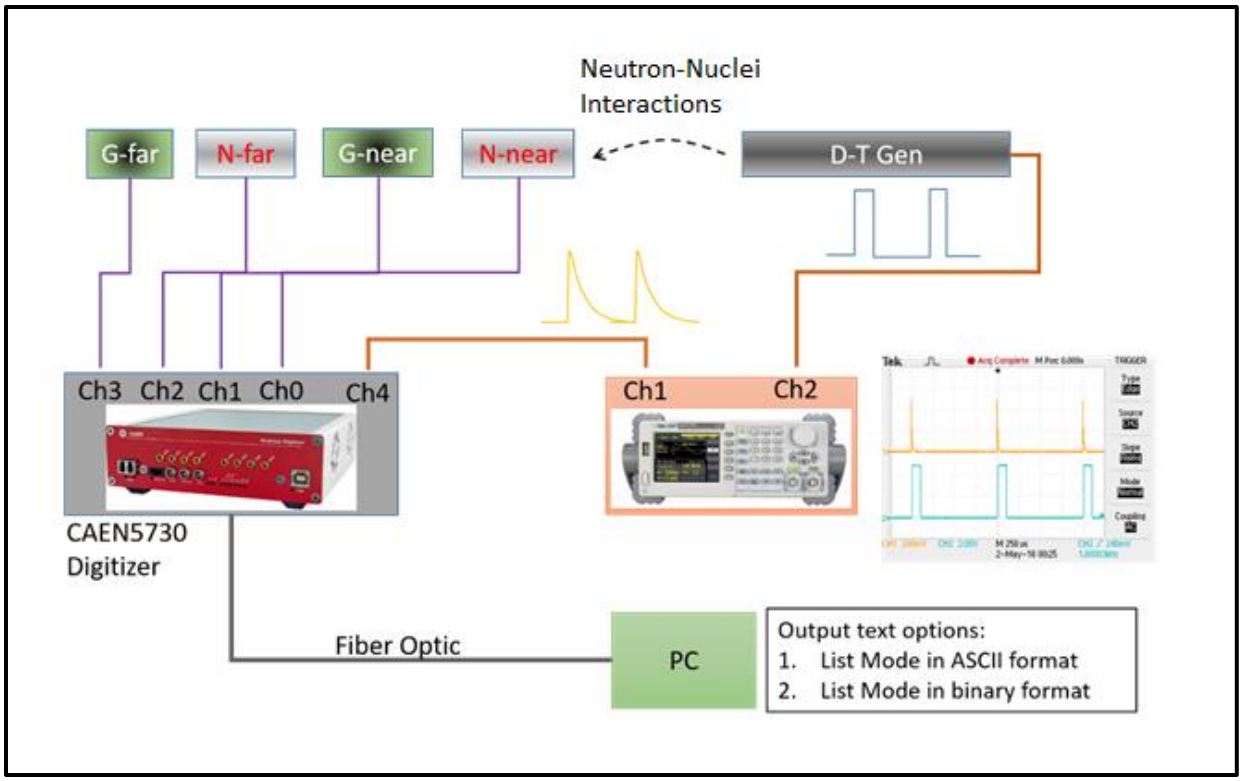

Figure 2.15 Overall schematic of the data acquisition system.

The user manual described how the list mode data was printed. A list was created for the five channels occupied in the digitizer (four lists for the four sensors' responses and one list was for the tail pulse signal). Figure 2.16 displays a list for the Near NaI(Tl) on the left called "Events list" and a list for the tail pulses from the waveform generator on the right called the "Triggers list". Each list has three columns. The first column in each list was index (1,2,3…). The next two are a column for timestamps and a column for energies. The second column in each list was a timestamp, ranging from 0 to 2^{31} unit; each unit increment was 2 ns. The third column listed channel number, ranging from 1 to 16,384 channels. List mode recorded pulse height in maximum ADC channel of 16,384. Whereas in calibration, the number of channels used was 2,048. The difference in channel can be linearly scaled down without consequences. The energies in the trigger list was preset at approximately 6,770. Only the timestamps were of interest in the trigger

list. Rejected events were assigned a value of -32768. This collection scheme permitted analyses of radiation events with respect to energy and time.

	Events list
1	990985713 2374
2	1204979649 2726
3	1305476485 2932
4	1342423986 416
5	1670964547 -32768
6	1972904434 215
7	229908075 397
8	393453902 2391
9	467451720 2658
10	813441274 -32768

	Triggers list
1	65175 6773
2	565160 6768
3	1065144 6767
4	1565128 6769
5	2065113 6770
6	2565097 6771
7	3065082 6768
8	3565066 6771
9	4065051 6772
10	4565035 6772

Figure 2.16 List-mode outputs for a sensor (left) and the trigger list (right).

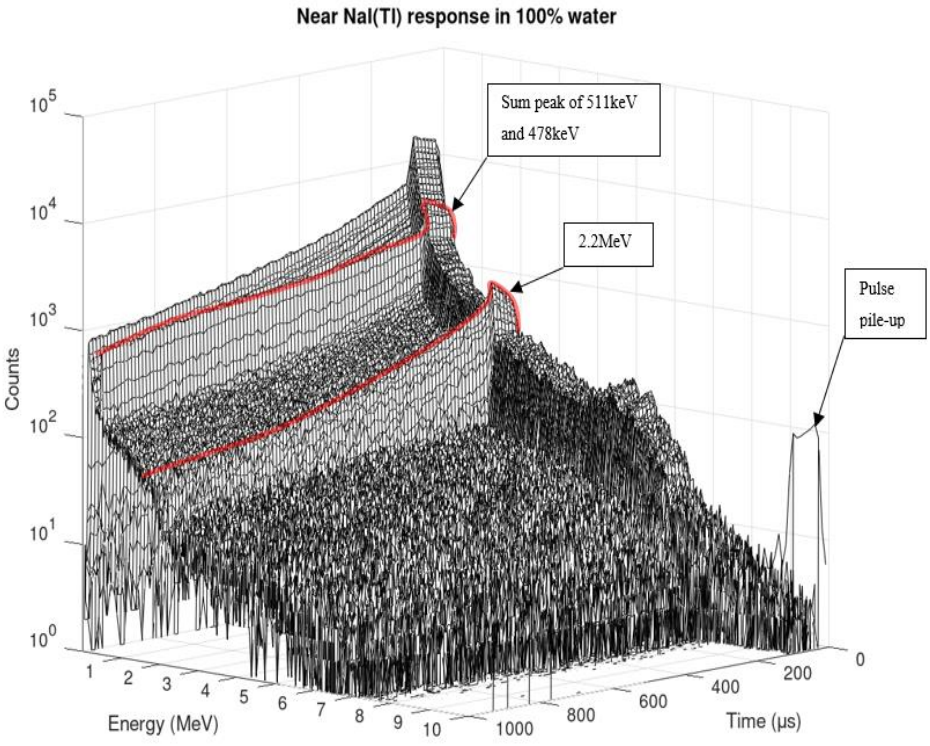

Figure 2.17 3D response of NaI(Tl) in water.

The events registered in the sensors can be plotted as a function of counts vs. time and energy. The plot in Figure 2.17 illustrated the Near NaI(Tl) sensor response in water as a function

of both time and energy. In the Figure 2.17, hydrogen prompt capture at 2.2 MeV and sum peak of 511 keV annihilation and 478 keV boron capture were observed. A sum peak is a convolution of peaks due to their proximity. The convoluted peak was a result of the low energy resolution of NaI(Tl) sensor. The energy resolution of NaI(Tl) as FWHM(%) vs. incident energy was plotted in Figure 2.18.

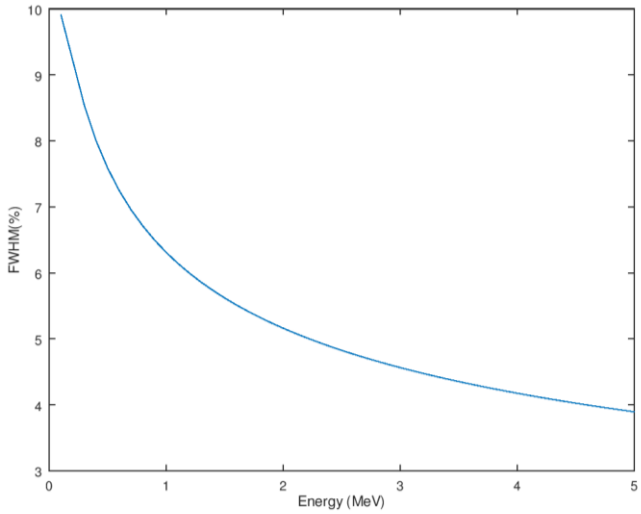

Figure 2.18 Energy resolution of NaI(Tl) sensor. Semi-empirical formula were obtained from [58]

The 3D response from the sand (5%) was also plotted and was shown in Figure 2.19. The 1.78 MeV peak in the sand sample was determined to be a peak from both aluminum capture (n,γ) and silicon (n,p) reactions—both reactions produced the same energy of 1.78 MeV.

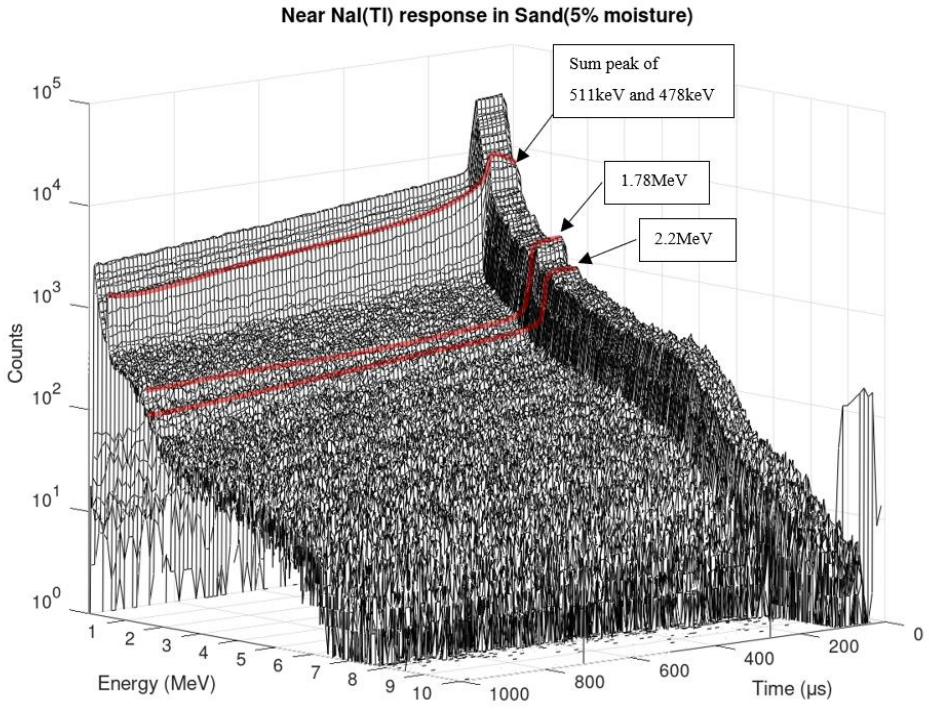

Figure 2.19 3D response of NaI(Tl) in sand.

The next chapter details the analyses of the sensors' responses. The analysis included studies of neutrons and the neutron-induced gamma radiation. The peaks identified in Figure 2.17 and 2.19 were analyzed. Neutron population was also studied and the 3D responses for neutron sensors can be found in the appendix. The results are in the next chapter.

3 Spectral and Time-Dependent Analyses

Spectroscopy is an important aspect of radiation analysis. Spectral features can be used to reveal an isotopes atomic density. Using the calibration between known energies and ADC channel from Figure 2.12, radiation events can be plotted as a function of energy *E*. Natural background radiations infer the composition of formation and can be found in the Appendix. The distribution of the energies collected during irradiation also infers information about the source as well as the medium. The subsections in this chapter detail the spectral analysis and progress on to the time dependent analyses—but first, the repeatability needed to be verified to gain a level of confidence in the data collected. The water sample was irradiated and measured in three repetitions. The time-dependent responses were plotted in Figure 3.1.

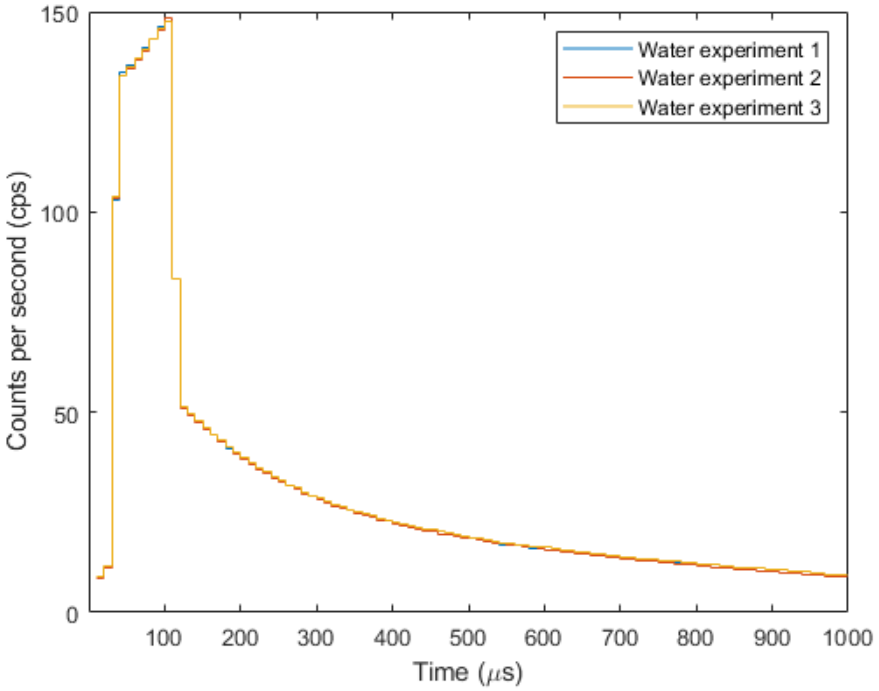

Figure 3.1 Time-dependent plots for the three water experiments.

3.1 Repeatability

The time-dependent plots for repeated measurements of a water sample were shown in Figure 3.1 and they appeared to be in good agreement. There was no reason to believe that a different water sample from the same source would have yielded a different result; so only one water sample was studied, and it was irradiated on three different occasions. The error associated with these measurements depended on the variability of the measurement system and the neutron source. The repeatability study explores variance between measured responses. The variance analysis was necessary in expressing the accuracy and preciseness of the result. The standard deviation in each ADC channel was calculated as followed:

$$c_{1i} = counts\ in\ the\ channel\ i\ from\ the\ 1st\ water\ experiment$$

$$c_{2i} = counts\ in\ the\ channel\ i\ from\ the\ 2nd\ water\ experiment$$

$$c_{3i} = counts\ in\ the\ channel\ i\ from\ the\ 3rd\ water\ experiment$$

where $\overline{c_i} = \frac{c_{1i}+c_{2i}+c_{3i}}{3}$ and $i = 1,2,3,4 \ldots 1000$. The value $\overline{c_i}$ is the average counts between the three water experiments in the *i* channel. The maximum ADC channel recorded in list mode is 16,384. For the analyses herein, the counts are re-binned into 1,000 ADC channels. The standard deviation is then estimated by least-square fitting the Gaussian function to the data points $x_i = [c_{1i},\ c_{2i},\ c_{3i}]$ in each channel *i*,

$$f(x) = \frac{A}{\sqrt{2\pi\sigma_i^2}} e^{\frac{-(x_i-\overline{c_i})^2}{2\sigma_i^2}} \tag{3.1}$$

such that the residuals are minimized. There are two unknowns: *A* is the scaling factor and σ is the standard deviation. Figure 3.2 showed the standard deviations for each ADC channel expressed as percentage of $\overline{c_i}$

$$\sigma(\%) = \frac{\sigma_i(channel)}{\overline{c_i}(channel)} \times 100\% \tag{3.2}$$

For the range of 1 to 700 ADC channel, the standard deviation was typically less than 10% for each channel. The standard deviations were much higher for the channel 700 and above because of lower number counts in those channels.

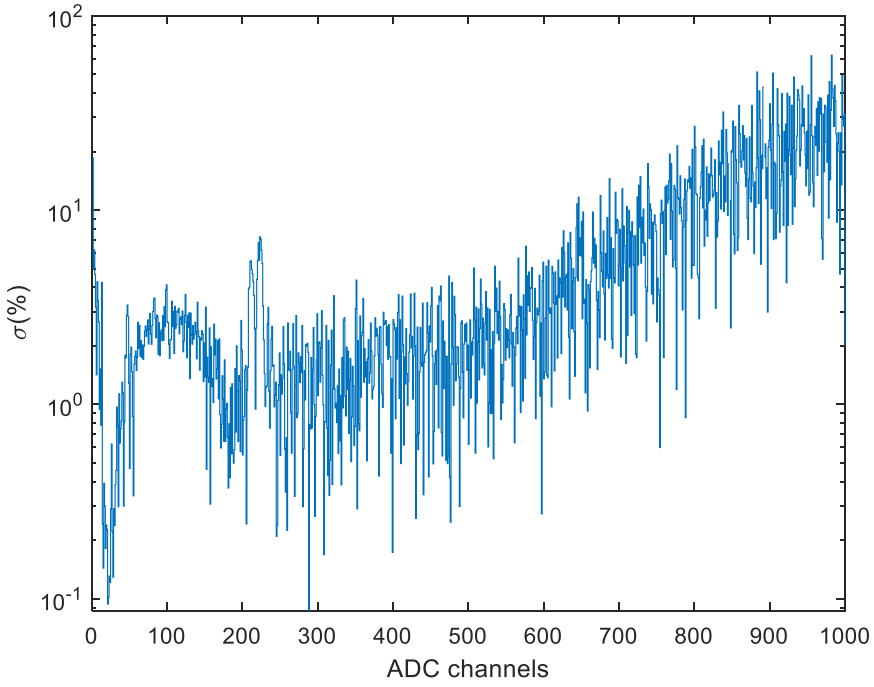

Figure 3.2 Repeatability study – Standard deviation as a function of ADC channel.

The standard deviations for each 10-μs bin was similarly calculated and the result was presented in Figure 3.3. In the period of 1,000 μs, the standard deviation for each 10-μs bin was less than 3%. The plot in Figure 3.3 looks different than the plot in Figure 3.2 because of prompt and delayed gamma ray emissions. For instance, some gamma rays such as one from oxygen neutron-inelastic scatter at 6.13 MeV were prompt emission and would appear in the first 100 μs.

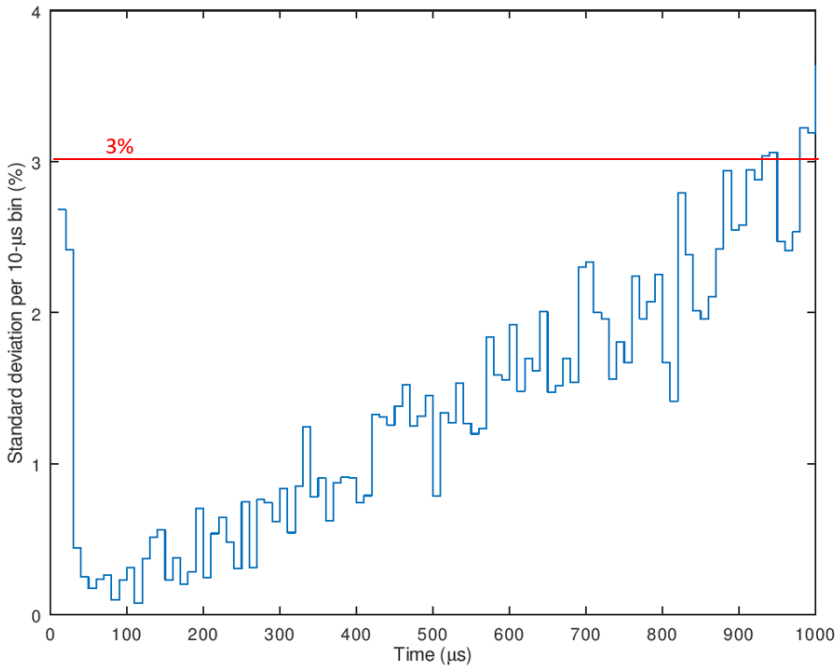

Figure 3.3 Repeatability study – standard deviation as function of time.

Prompt inelastic reactions were expected to dominate in the first 100 µs and thermal capture reactions were expected to dominate the last 900 µs. Depending on the amount of neutron moderator presence, significant thermal capture gamma rays can also be recorded in the first 100 µs. Refer to Figure 3.4 where spectra were generated from different time regions. Hydrogen prompt capture 2.2 MeV persisted in all three different temporal regions of this water sample while oxygen inelastic scatter gamma ray 6.1 MeV diminished after the first 100 µs. The threshold neutron energy for oxygen inelastic scatter to occur is 8.5 MeV. Inelastic scatter gamma rays 6.1 MeV were dominant in the 0-120 µs time region and completely disappear in the later temporal regions 130-560 and 570-1,000 µs. Fast neutrons influenced the oxygen inelastic scatter intensity, while water moderated fast neutrons. The competing processes governed the intensity of inelastic scatter 6.17 MeV gamma.

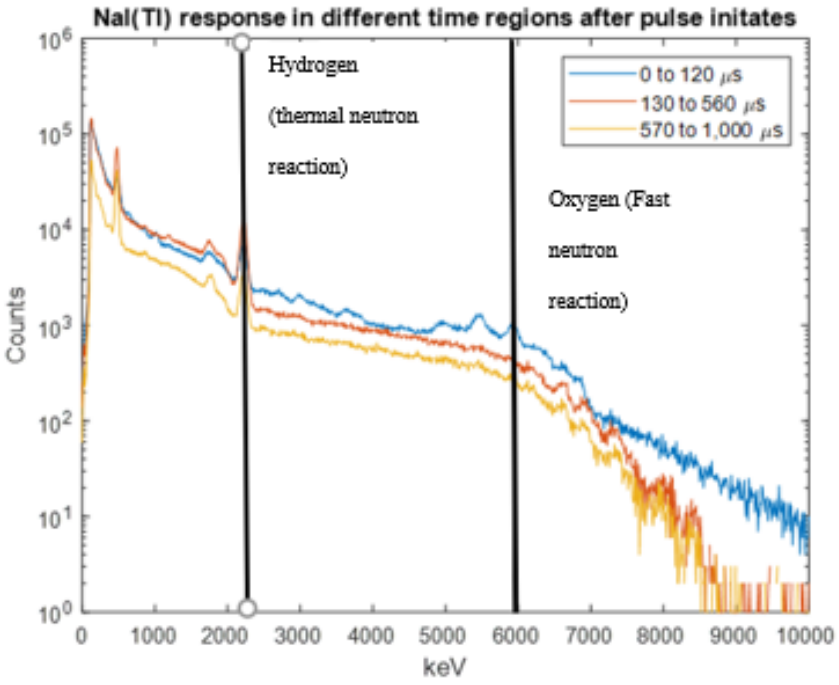

Figure 3.4 Spectra from 3 temporal regions for water.

3.2 Macroscopic Capture Cross Section and Decay Time Constant

Neutrons can lose significant energy when colliding with a hydrogen nucleus., On average a neutron loses 50% of its energy in a collision with hydrogen. The term α is called the collision parameter and is defined by the mass number of the target nucleus

$$\alpha \equiv \left(\frac{A-1}{A+1}\right)^2 \tag{3.3}.$$

Because of the low atomic mass, hydrogen slows neutron down via elastic scatter. High atomic mass nuclei slow neutrons down via both elastic and inelastic scattering. On average a neutron loses about 14% of its energy when scattered by a carbon nucleus. Neutron loses less energy when colliding with heavy nuclei [11] than with lighter nuclei. Thus, in the presence of hydrogen, neutrons lose more energy per collision leading to high thermal neutron populations in the borehole environment. As the speed of neutron v decreases, the probability of absorption

increases; capture cross sections are generally proportional to $1/v$. The rate that a formation absorbs neutrons can be inferred by a thermal neutron sensor. The neutron absorption rate at a fixed sensor location can be expressed as a function of time *t.* Analogous to radioactive decay, the manner to which thermal neutron are absorbed can be predicted by the following expression:

$$N(t) = N_o e^{-v\Sigma_a t} \tag{3.4}$$

where $N_o$is the initial number of thermal neutrons at t = 0, Σ_a is the macroscopic thermal cross section and v is thermal neutron speed (220,000 cm per second). $N(t)$ is the number of thermal neutrons after some time *t.* The macroscopic cross section for a compound is

$$\Sigma_a = \sum_1^n \sigma_{ia} N_i \tag{3.5}$$

where n is the number of different elements in the compound, σ_{ia} is the microscopic absorption cross section (barn or square centimeter) of element *i*, and *N* is the atomic number density (atom per cubic centimeter). For well logging, the effective total microscopic cross section is defined as $\sigma_{total} = \sigma_{elastic} + \sigma_{inelastic} + \sigma_{absorption}$. The $\sigma_{absorption}$ is the sum of all the neutron absorption reactions, e.g. (*n,γ*) or (*n,pγ*). The decay time constant associated with thermal capture of a formation can be calculated by the following expression:

$$\tau_D = \frac{1}{v\Sigma_a} = \frac{4550}{\Sigma_a}\ (\mu s) \tag{3.6}$$

The capture cross section Σ_a is in capture unit (c.u.) in equation (3.6). A c.u. is $1000 \times cm^2/cm^3$, cross-sectional area per unit volume. Various capture cross sections and decay time constants at room temperature are listed in reference [2]. The Table 3.1 below lists some materials' capture cross section and decay time constant. By measuring the capture cross section information about atom density can be calculated. The "Handbook on Nuclear Data for Borehole Logging and

Mineral Analysis" provides a collection of data for well logging purposes, including the capture cross section [4].

Table 3.1 Capture cross section and decay time constants. Source [2].

Material	Σ_a **(c.u.)**	τ_D (μs)
Sand	4.26	1,086
Limestone	7.07	643
Limestone(20% water)	10.06	452
Water	22	206
Saline (26%wt)	125	36

Saline data from the Table 3.1 shows a large capture cross section for saline. The large capture cross section Σ_a in saline can be attributed to its chlorine concentration. Refer to Figure 3.5 for the thermal neutron capture in water as function of salinity. The lines in the Figure 3.5 indicate the levels of salinity and the corresponding capture cross sections of the two saline samples in this dissertation. The Figure 3.5 predicted that the 3.6%wt saline would have $\Sigma_a \cong 36\ c.u.$ and the 7.2%wt would have $\Sigma_a \cong 49\ c.u.$.

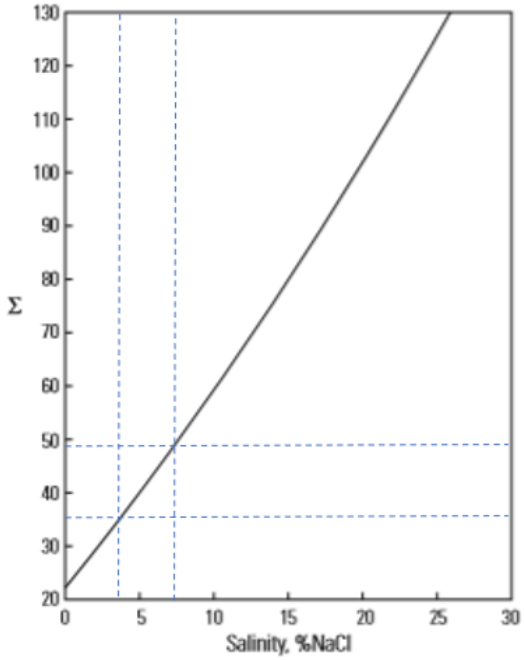

Figure 3.5 Thermal capture (c.u.) as a function of salinity in weight percent. Adapted from Source [2].

The challenge with measuring capture cross section is the diffusion of thermal neutrons. At any given time, the neutron population is both diffusing and being captured, the diffusion influenced the calculated τ_D in the experiment. In the experiments, the measured time decay constant is an apparent decay time called τ_a. The apparent decay time constant τ_a is a sum of the intrinsic decay time constant $\tau_{int} = \tau_D$ and the diffusion time τ_{diff}:

$$1/\tau_a = 1/\tau_{int} + 1/\tau_{diff} \tag{3.7}$$

where $1/\tau_{int} = \nu\Sigma_{\mathrm{a}}$ and $1/\tau_{diff} = -D\nu\frac{\nabla^2 N}{N}$. In a homogenous medium, τ_{diff} depends on the source-to-sensor distance and the diffusion coefficient D (inverse correlation with τ_{diff}). Diffusion coefficient D decreases as porosity increases, as seen in Figure 3.6. The equation describing the local (at the sensor location) capture and diffusion of neutron population is:

$$\frac{1}{N}\frac{\partial N}{\partial t} = -\nu\Sigma_{\mathrm{a}} + D\nu\frac{\nabla^2 N}{N} \tag{3.8}.$$

In practice, without diffusion correction, the value of the measured τ_a would appear larger than the intrinsic value τ_{int}. Three different rock formations such as limestone, sandstone, and dolomite have different diffusion coefficients at low porosity, but their diffusion coefficients converge as porosity increases. Refer to Figure 3.6 for the diffusion coefficients of various formations and porosity.

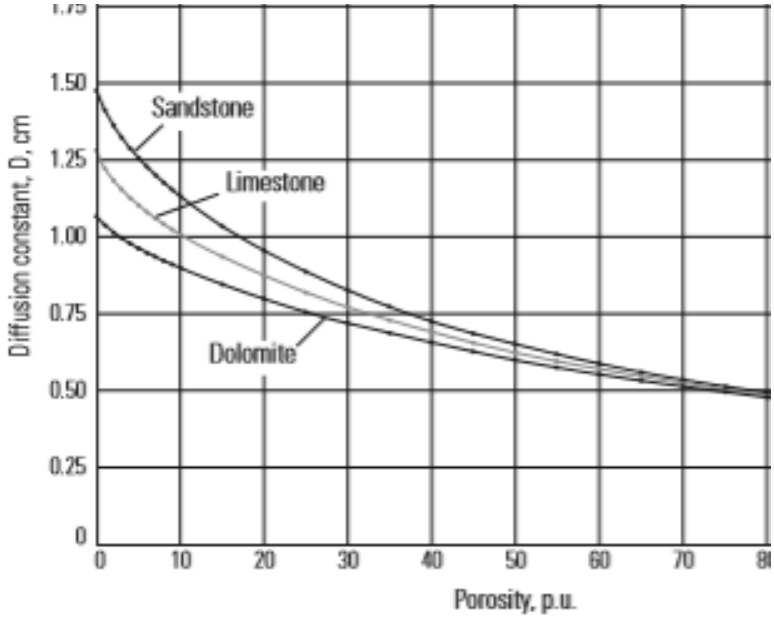

Figure 3.6 Diffusion coefficients for various water bearing formations. Figure adapted from source [2]

If the Σ_a of the formation is much greater than the Σ_a of the borehole then the borehole would act as a neutron sink (this is called the borehole effects). The borehole effect makes it difficult to obtain the formation capture cross section, as seen in Figure 3.7 where A_{BH} is the activity component from borehole and A_F is the activity component from the formation.

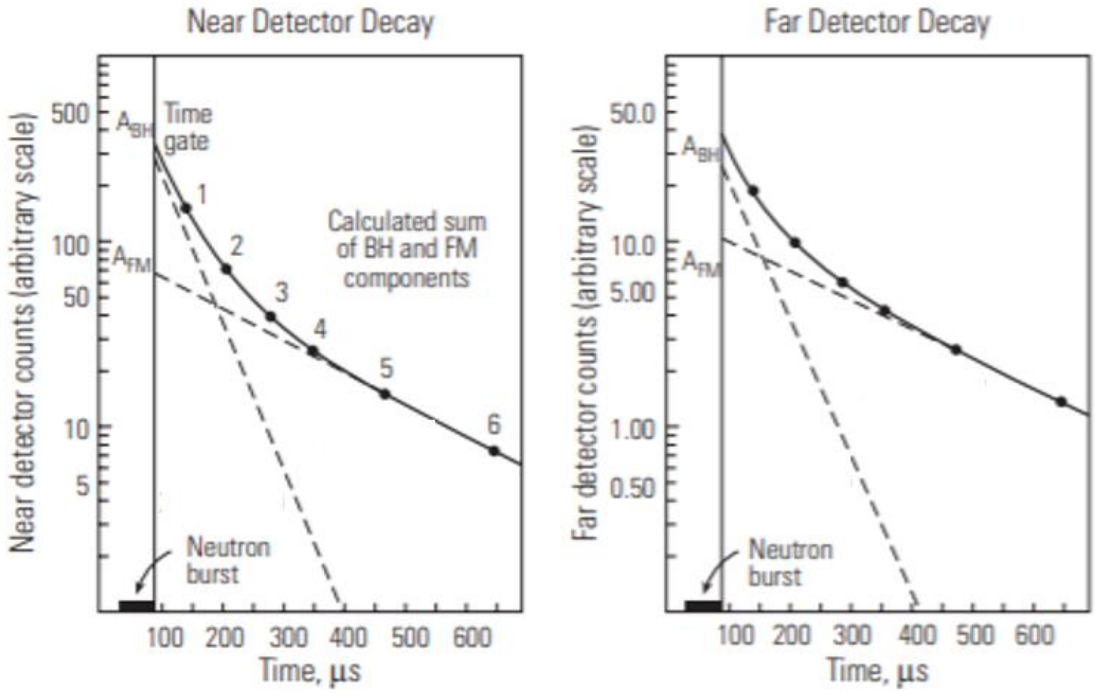

Figure 3.7 Components of the decaying counts the Near and Far sensors. Figure adapted from source [59].

In the experiments performed here, the aluminum borehole wall was filled with only air. The capture cross section for dry air in capture unit was calculated as 0.076 c.u. and capture cross section for aluminum in capture unit was 14.4 c.u.. The calculation for air was executed with the values of atomic density and thermal capture cross sections in the Table 3.2 below.

Table 3.2 Macroscopic capture cross sections calculated for various materials from experiments.

	Atomic density (atoms/cc)	**Thermal Capture (barn)**	$\boldsymbol{\Sigma_a(c.u.)}$	$\boldsymbol{\tau_{int}(\mu s)}$
Air(0.0013g/cc)	0.025E21	3.04	0.076	161,644
Aluminum (2.7g/cc)	6.026E22	0.233	14.4	316
Sand(1.6g/cc)	1.7E22	0.1689	5.7	798
Water(1g/cc)	3.343E22	0.3320	22.2	205

The air capture cross section was much less than the experimental formations' capture cross sections. The effects of τ_{int} and τ_{diff} were illustrated by the Near BF_3 sensor responses plotted in Figure 3.8. The Near BF_3 response in Sand(5%) had smaller τ_{diff} than water's τ_{diff}. The smaller difference in capture cross section between borehole and formation resulted in the quick drop of thermal neutrons after 100 μs in the sand sample. The borehole effects can be seen in the water and limestone samples in Figure 3.8. Water displays high activity from the borehole, where the bore acted as a neutron source. Water is expected to decay faster than sand and limestone as seen in Table 3.1. However, in the Figure 3.8 water is shown to decay at a slower rate. In fact, the thermal neutron population was observed to be increasing after 100 μs for water. Water had a higher value of τ_{diff} which resulted in thermal neutron population persisting after 100 μs near the sensor location. The cloud of thermal of neutrons stayed near the source in water because of small diffusion coefficient *D*. The cloud of thermal neutrons diffuses outward faster in sand and limestone.

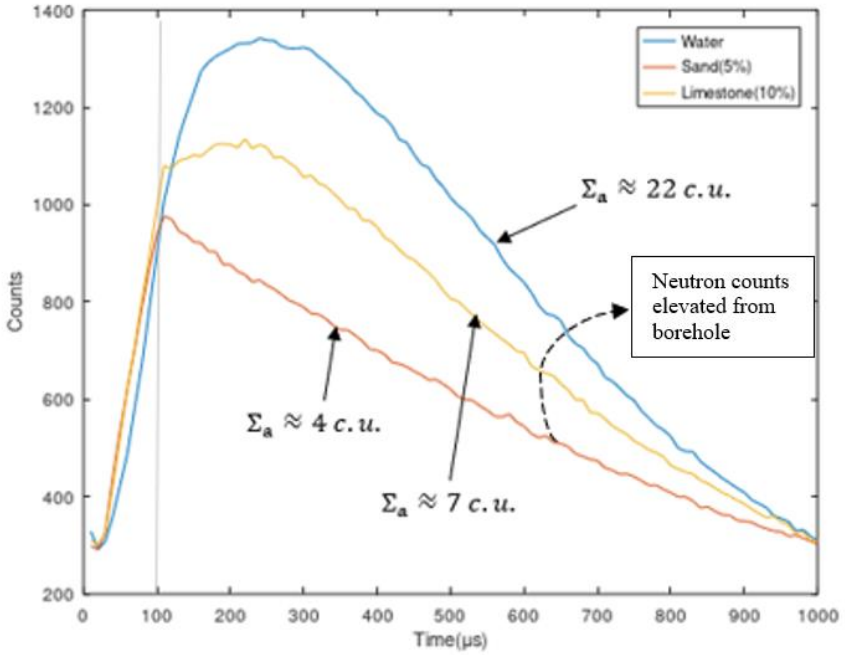

Figure 3.8 Time distribution of thermal neutrons at the Near BF_3 for water, sand, and limestone.

The borehole effect can also be observed in the case of high salinity, as seen in the Figure 3.9. In saline experiments, the thermal neutron population strongly depends on τ_{int} of the thermal capture of chlorine. In presence of strong absorbers, the apparent decay time constant τ_a became smaller because τ_{int} is much smaller. When τ_{int} is lower, the measured τ_a is strongly influenced by the undesirable borehole effect. In Figure 3.9, the borehole effect can also be seen with saline via the rising thermal neutron counts after 100 μs. Higher salt concentration increases the borehole effect to the measured τ_a.

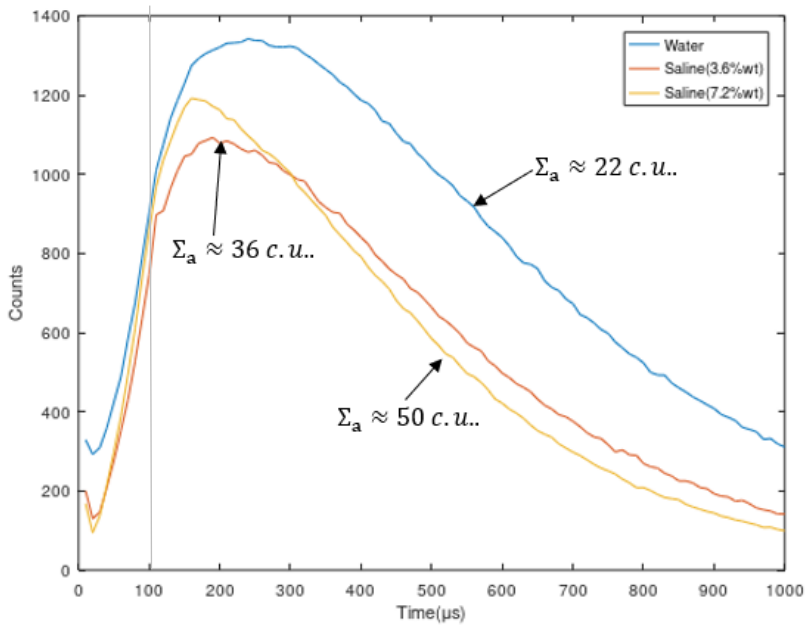

Figure 3.9 Time distribution of thermal neutrons at the Near BF_3 for water and saline at two concentrations.

How much borehole effect contribute to the thermal neutron population after 100 μs also depends on the location of the neutron sensor. The Figure 3.10 below illustrates how absorption and diffusion influenced the Far thermal neutron response. At the Far location, sensors were less influenced by borehole effects. Neutron counts immediately drops after 100 μs. The drawback at Far sensor location is the large uncertainty in capture cross section estimate because fewer counts

arrived there. Notice the intensity of the water sample, less counts arrived at the Far location for water sample compared to sand and limestone samples. In contrast, at the Near location, the sensor had more counts for water than sand and limestone. This is a result of the smaller diffusion coefficient *D* and larger capture cross section Σ_a of water.

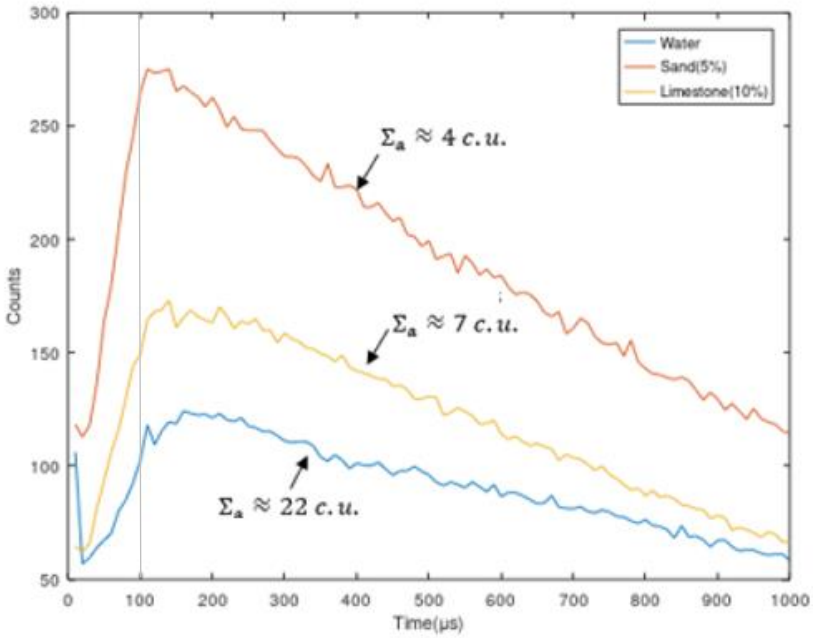

Figure 3.10 Time distribution of thermal neutrons at the Far ^{3}He for water, sand, and limestone.

The salinity effects can also be observed at the Far sensor. Because of large difference of Σ_a in air (borehole) vs. water and saline (formation), the borehole effect persists at the Far location, as seen in Figure 3.11. The neutron population can be seen rising after 100 μs because of larger capture cross section difference between the borehole and formation. The borehole effect is more dominant in the case of high salt concentration as compared to low salt concentration.

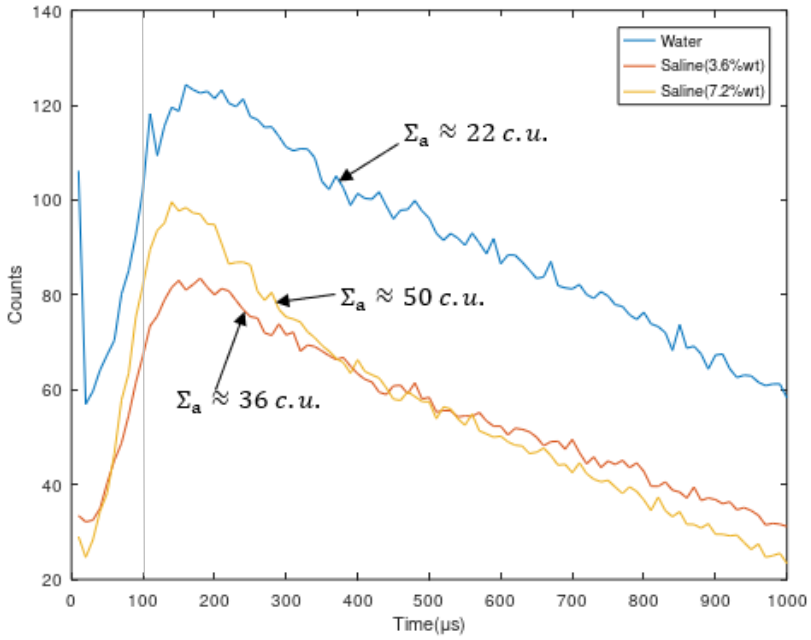

Figure 3.11 Time distribution of thermal neutrons at the Far ^{3}He for water and saline at two concentrations.

In the next section, capture gamma rays are observed and used to estimate capture cross sections. Decay of bulk capture gamma rays have been studied previously. Patents have been reported for measuring τ_{int} or Σ_a from neutron and bulk capture gamma rays decay to produce porosity estimate, e.g. patent US4721853A [60], US4947040A [61] in late 1980s. Refer to Figure 3.12 for a sample of bulk gamma rays decay with time gates at the bottom. The patents reported the use of time gates and interpretation processes using those time gates. For example, the counts *N(t)* in within two time gates t_1 and t_2 are used to estimate Σ_a

$$\frac{N(t_2)}{N(t_1)} = e^{-v\Sigma_a\,(t_2 - t_1)} \tag{3.9}.$$

Early gates are plagued by borehole effect, so the patented technologies are the processes of separating the signals from borehole and formation. Patent US4721853A described a method that employed variable duty cycle generator to produce a short neutron pulse and a long neutron pulse. The time gates after the long and short pulse were correlated to produce sigma Σ_a. Patent

US4947040A follows up on the previous patent by converting the Σ_a into porosity by isolating the borehole effect from the decay of thermal neutrons. A recent patent US10437813 in 2019 [62] claimed to use time gates to isolate thermal capture gamma from inelastic gamma and producing multiple sigma values to estimate elemental concentrations. The inventor cited Grau's work [25] in this patent.

In this dissertation an approach using prompt capture gamma rays is explored. Instead of observing neutron capture rate or bulk capture gamma capture rate, isotopic prompt capture gamma rays from hydrogen are observed. The prompt emission introduces a fraction of nanosecond delay in the measurement of the macroscopic neutron capture Σ_a, which is negligible on the microsecond scale. The analysis is described in the next section. Advantages and drawbacks are discussed.

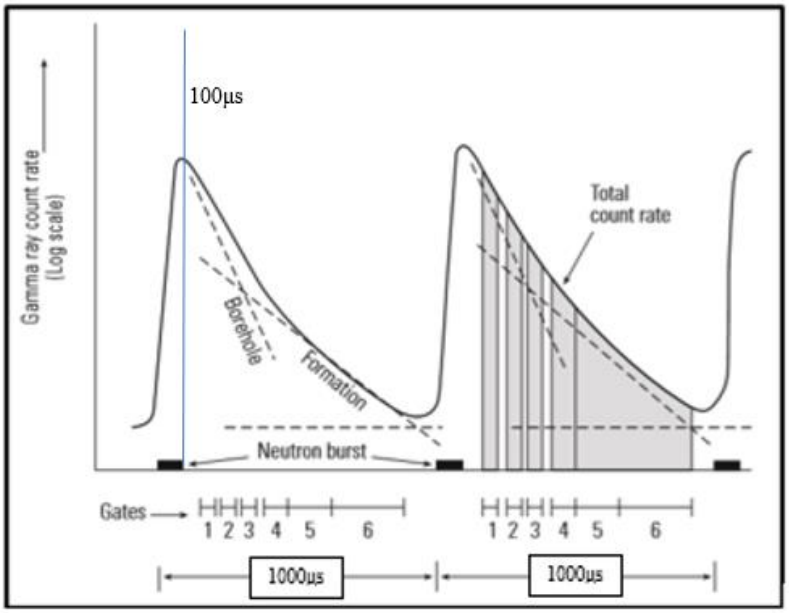

Figure 3.12 Gamma ray time distribution in a short pulse scenario. Figure adapted from source [2]. Original source [59].

3.3 Hydrogen Prompt Capture Gamma Ray Analysis

The intensity of the 2.2 MeV gamma is influenced by the HI and the formation's attenuating characteristics for a location *r* and time *t*. The Figure 3.13 below illustrates how the thermal neutron population migrate as a function of time away from the source. The thermal neutron population *N* at time t_1 reflects the characteristics of the borehole whereas thermal neutron population at time t_2 reflects the characteristic of the formation. The thermal neutron absorption and the subsequent 2.2 MeV gamma emissions from a later time t_2 reflect characteristics of the formation. The 2.2 MeV gamma intensity is less influenced by the borehole effect because of the location of hydrogen in the experiments (hydrogen was only in the matrix and not the borehole).

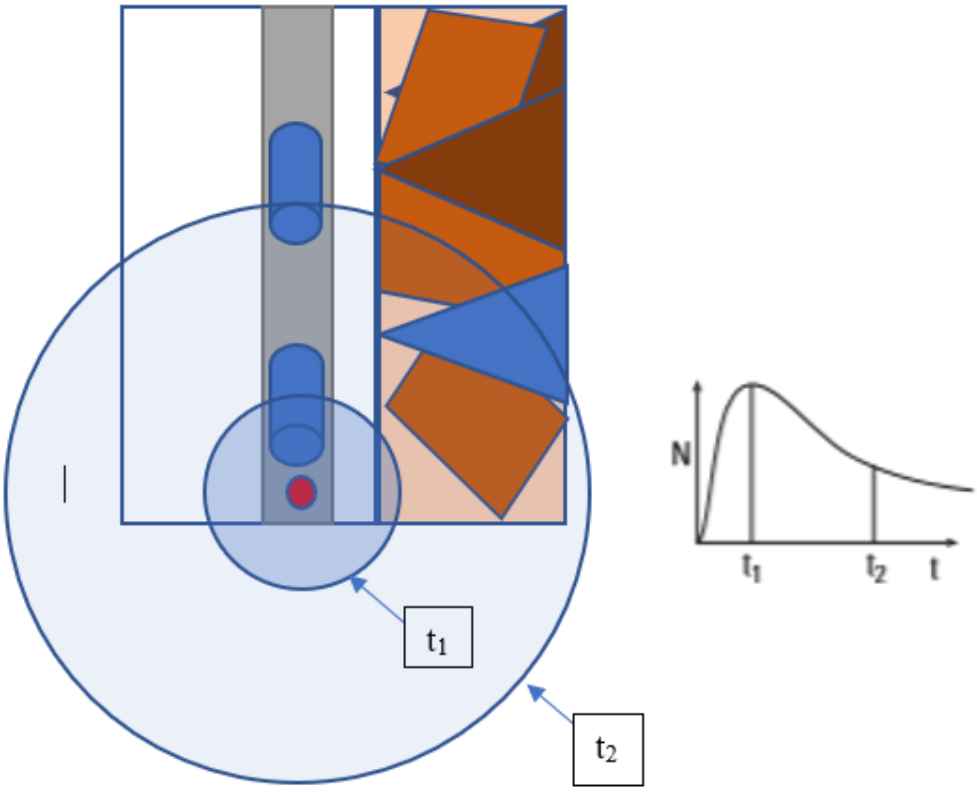

Figure 3.13 Thermal neutron migration at two different time references t_1 and t_2.

This section details the spectral analysis of 2.2 MeV gamma rays from the experimental data collected for RDRS. The hydrogen prompt capture intensity is directly influenced by thermal neutron population and the HI of the formation. The emission of 2.2 MeV gamma depends mainly on the thermal neutron absorption rate in the formation. Prompt emission of 2.2 MeV occurs in a fraction of a nanosecond after neutron capture. The time gamma rays take to arrive at the sensor location is not a concern because gamma rays travel at speed of light, ×100,000 faster than the speed of thermal neutrons. The 2.2 MeV gamma rays were studied in the time frame of 100-900 μs after a neutron burst. Because no other mass in the experiment had hydrogen except in the added water or moisture content. The Σ_a value is a direct measure of the hydrogen atomic density or the amount of water added to the tank.

The following is the process of estimating the capture cross sections using hydrogen prompt gamma. Some of the experimental result from this section were published by the dissertation author in references [63] and [64]. The time-dependent distribution of bulk gamma rays for all the experiments were generated. The responses for the Near NaI(Tl) were plotted in Figure 3.14 below. Visually one could observe that the Saline(3.6%wt) had the highest Σ_a out of all samples.

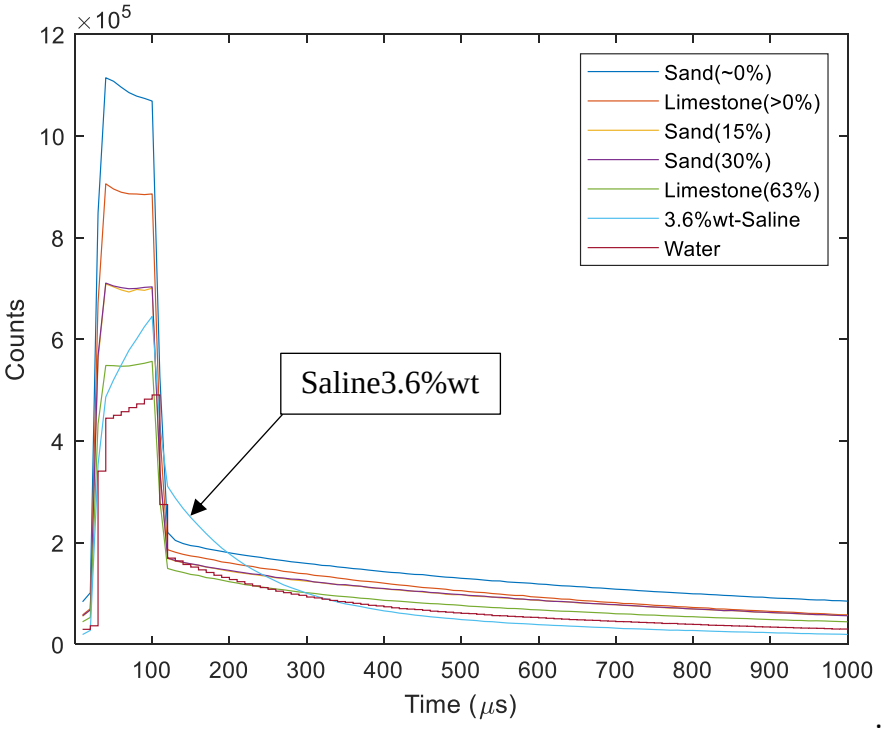

Figure 3.14 The Near NaI(Tl) gross counts time distribution for each sample material.

Instead of using time gates to estimate Σ_a, the 1,000 μs length the neutron burst was discretized into 100 bins of 10-μs width and fitting process was used. The radiation events for all ~3,300,000 neutron bursts were binned into those 100 bins as shown in the Figure 3.15. Those events detected within each 10 μs bin were then used to produce 100 pulse-height spectra. For example, the events within the time bin 90-100 μs were plotted in the Figure 3.16.

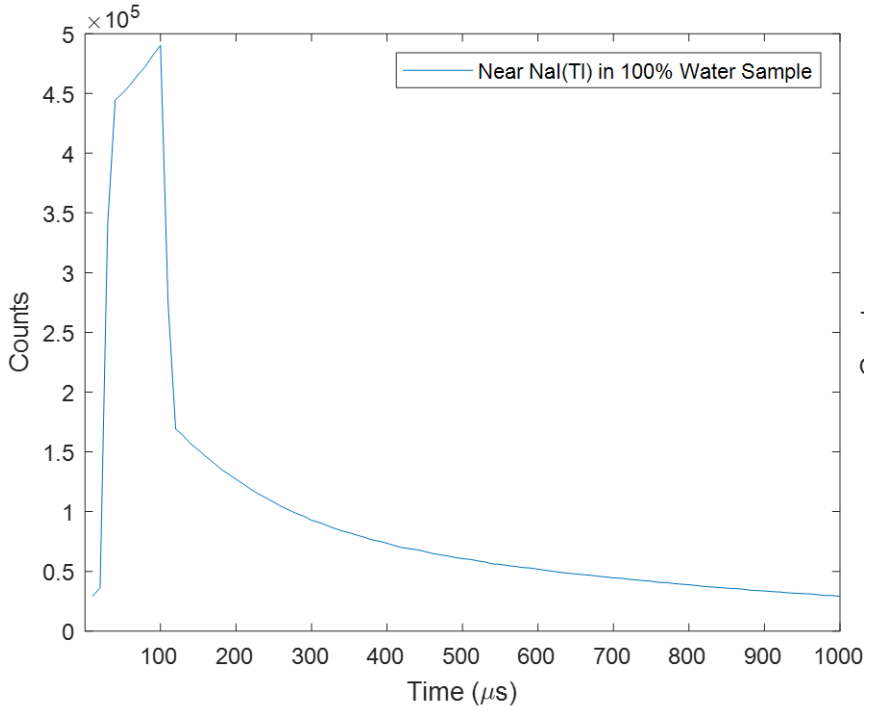

Figure 3.15 The gamma ray time-dependent distribution for the Near NaI(Tl) in 100% water.

These 100 spectra have spectroscopic features that vary with respect to the time within the neutron burst cycle. These spectroscopic features from neutron-induced gamma rays infer information about the bulk materials. Hydrogen content is of special interest in determining hydrocarbons, the hydrogen prompt-capture full-energy peaks were analyzed for those 100 spectra. A Gaussian and a quadratic function were used to fit the data and calculate the 2.2 MeV net peak counts for each of the 100 spectra. An example fit is shown in Figure 3.17.

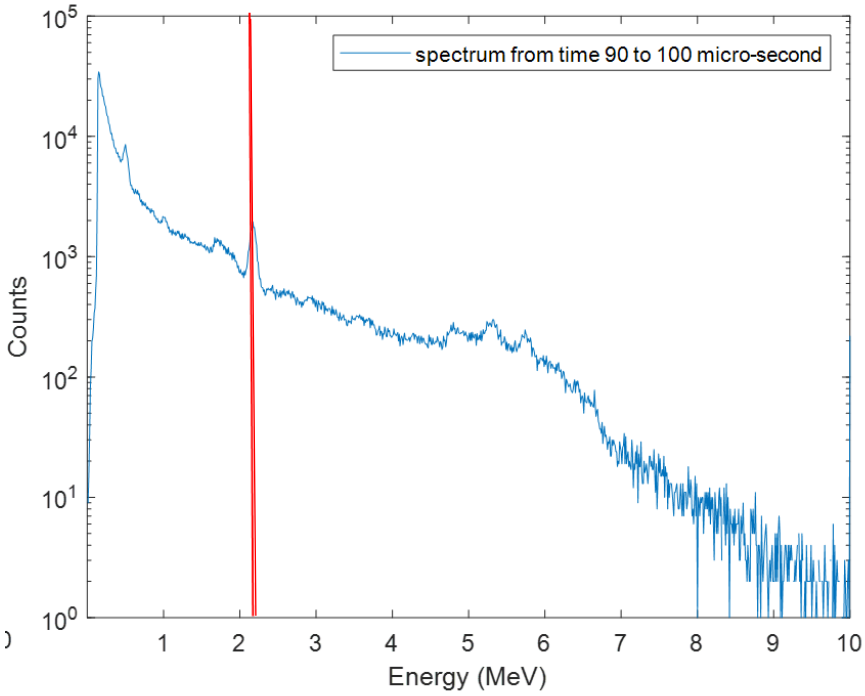

Figure 3.16 Spectrum generated from between 90 and 100 μs

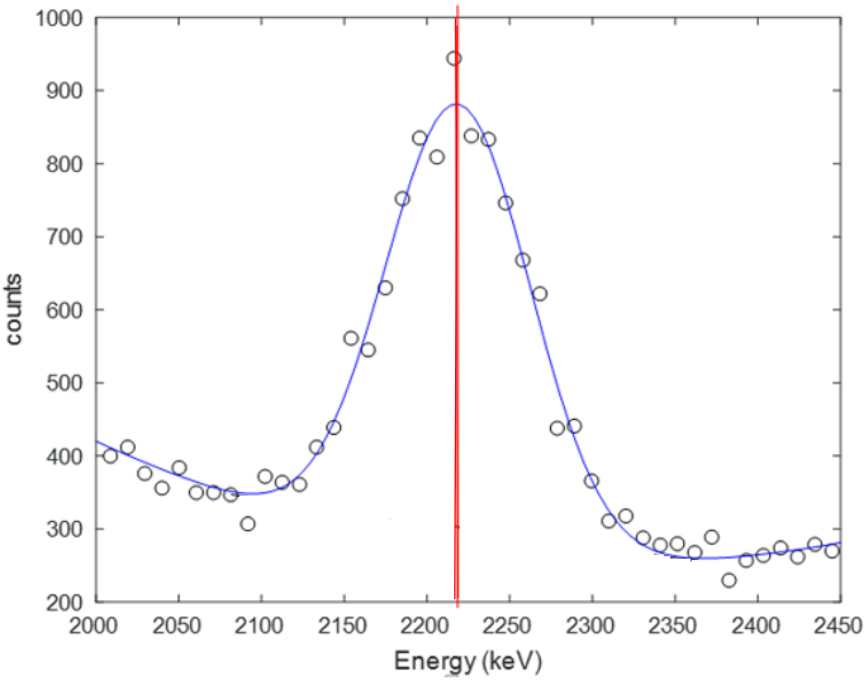

Figure 3.17 Gaussian and quadratic fit to the prompt-capture hydrogen peak.

The general fitting algorithm to calculate the net hydrogen peak is described below.

The fit model for a single peak is:

$$\frac{A}{\sqrt{2\pi\sigma^2}} e^{\frac{-(x-\mu)^2}{2\sigma^2}} + ax^2 + bx + c \qquad (3.10).$$

The quadratic function estimates the background. *A* is a scaling factor or counts in the Gaussian function. Using Trust Region algorithm, the equation (3.10) is least squares fit to the measured data in the range (195 to 240 ADC channels) with the parameters *A, σ, μ, a, b,* and *c*. Trust-Region algorithm is a simple and powerful concept in optimization. Trust Region allows users to input initial values of the fit parameters. MATLAB Trust Region approximates the minimizing function *f* with a simpler function *q* that reflects the behavior of *f* in a neighborhood surrounding a point *x*. The neighborhood surrounding *x* is the trust region.

The result of *σ, μ, a, b,* and *c* are then inserted into the model in equation (3.10) another time—this time leaving *A* as the only fitting parameter as a new model. The new model with only *A* as a fit parameter is least squares fitted using Levenberg-Marquardt algorithm. the value *A* and its 68% confidence interval were calculated. The Levenberg-Marquardt and Trust Region are both described by the MathWorks Help Center document titled "Equation Solving Algorithms" [65]. The resulting net peak counts plotted against time was shown in the Figure 3.18.

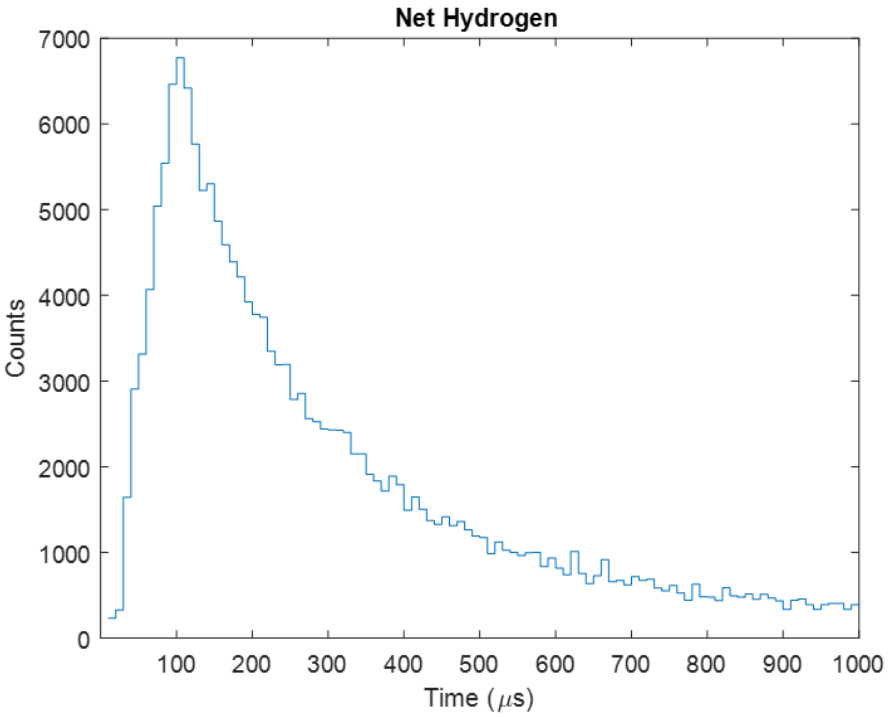

Figure 3.18 Prompt-capture hydrogen counts *A* as a function of time *t*.

The counts decay from 120 to 1,000 μs were studied. The die away was fitted with an equation:

$$(M - m)e^{\frac{-t}{\tau_a}} + m \qquad (3.11).$$

M is the counts value at 120 μs, and *m* is the value at 1,000 μs. τ_D is the time for the 2.2 MeV intensity to reduce by 63%, and *t* is the time after a neutron pulse is initiated. Refer to Figure 3.19 for the fit from 100% water experiment. The decay time constant τ_a is approximately $\tau_a = \frac{1}{\nu\Sigma_a} = \frac{4550}{\Sigma_a}$ (μs). This fit model in equation (3.11) produces the time decay constant value τ_a.

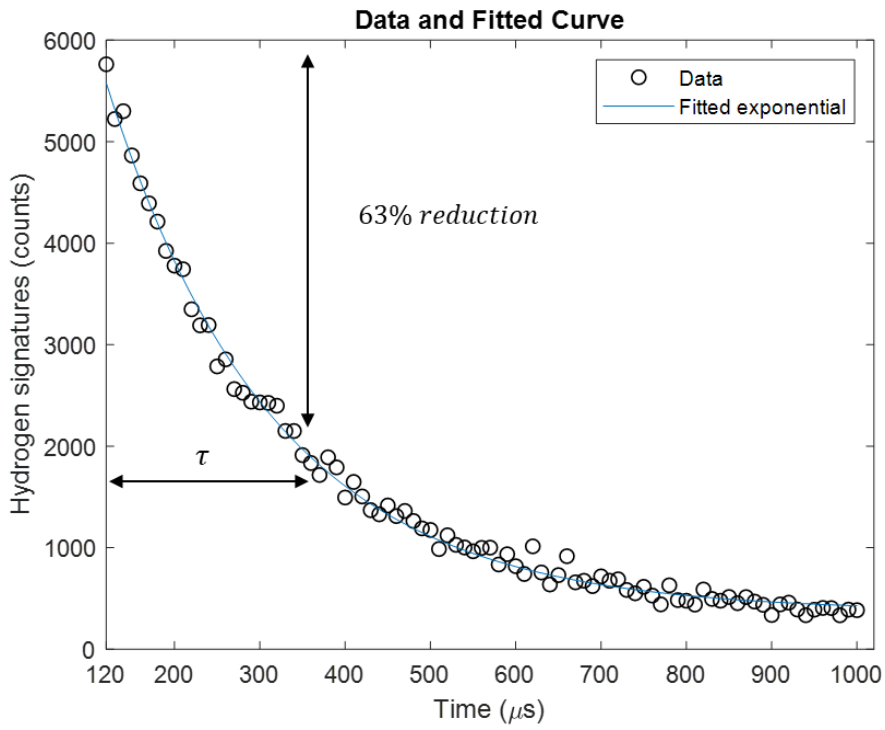

Figure 3.19 Prompt-capture decay constant τ_a estimate for the 100% water sample at Near NaI(Tl) sensor.

Table 3.3 Decay τ and moisture content relationship

Experiment	Moisture content (%volume)	2.2 MeV counts	Measured τ_a (μs)	Measured $\nu\Sigma_a$ (us^{-1})	68% Confidence in τ_a (%)
Nearly Dry Sand	5	24,567	1,171	0.000854	182%
Nearly Dry Limestone	10	55,545	710	0.001408	76%
Partially Saturated Sand	15	78,145	427	0.002341	17%
Fully Saturated Sand	30	76,995	351	0.002849	12%
Fully Saturated Limestone	63	53,092	227	0.004405	11%
Water	100	173,025	195	0.008000	1.5%
Saline (3.6%wt)	98.3	107,038	125	0.005128	5.6%

The measured decay constant τ_a for Near NaI(Tl) in each experiment was tabulated in Table 3.3. Table 3.3 also listed measured values of $\nu\Sigma_a$. The $\nu\Sigma_a$ and τ_a values exhibited a distinguishable relationship with moisture content. As moisture content increases, the τ_a value

decreases. The 68% confidence interval τ_a is much larger for low porosity scenarios indicating the small presence of hydrogen. An exponential decay process is fit best with a larger population of hydrogen. The expression $v\Sigma_a$ has a response curve that is nearly linear with respect to HI, as seen Figure 3.20. As discussed in Chapter 1, the added moisture content percentage here is HI.

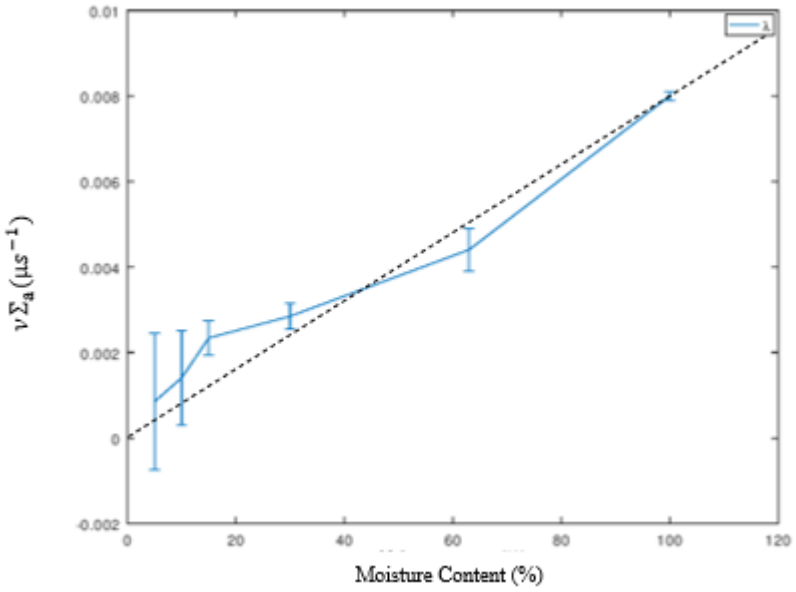

Figure 3.20 Moisture content linear correlation with $v\Sigma_a$.

The calculated values τ_{int} and Σ_a in reference [2] and measured values in this dissertation were compared. The Table 3.4 listed those said values, where similarities were observed in the "Nearly Dry Sand" sample and Ellis' sand sample, as well as the "Nearly Dry Limestone" sample and Ellis' limestone sample. The values for water were also close. A range of Σ_a was listed in Table 3.4 also. In practice the formations are complex and can vary greatly depending on the mineral composition of the rock matrix.

Table 3.4 Comparison between τ_D and $\nu\Sigma_a$ listed in reference [2] and experimentally derived values

From Ellis [2]			**Experimental values**			**Range of Σ_a** [66]	
Material	$\Sigma_a(c.u.)$	$\tau_{int}(\mu s)$	**Materials**	$\Sigma_a(c.u)$	$\tau_a(\mu s)$	**Materials**	$\Sigma_a(c.u.)$
Sand	4.26	1,086	**Sand(5%)**	3.89	1,171	**Sands**	4.55 to 18
Limestone	7.07	643	**Limestone(10%)**	6.41	710	**Calcite**	7.08 to 7.50
Limestone (20% water)	10.06	452	**Limestone(63%)**	20.0	227	**Dolomite**	4.7 to 8.0
Water	22	206	**Water**	23.3	195	**Anhydrite**	15 to 25
Saline (26%wt)	125	36	**Saline (3.6%wt)**	36.4	125	**Clay Minerals**	15 to 60
			Saline (7.2%wt)	40.1	111		

The experimental saline 3.6%wt have a $\Sigma_a = 36.4\ c.u.$—a value that was predicted earlier from the Figure 3.5 to be 36 c.u.. The $\Sigma_a = 40.1$ for the sample saline labeled 7.2%wt suggested that the salt content was only around 5%wt for that saline sample, off by 2.6wt%. This suggests that as salinity increases the estimate is more influenced by diffusion and borehole effects.

Measured $\nu\Sigma_a$ values are normalized and plotted against moisture content and salinity in Figure 3.21. The blue data points are data points without thermal neutron absorber and the orange data points are with thermal absorber. Presence of salt or other thermal absorbers in pockets of formations would result in larger apparent Σ_a which affects the HI and sigma estimates.

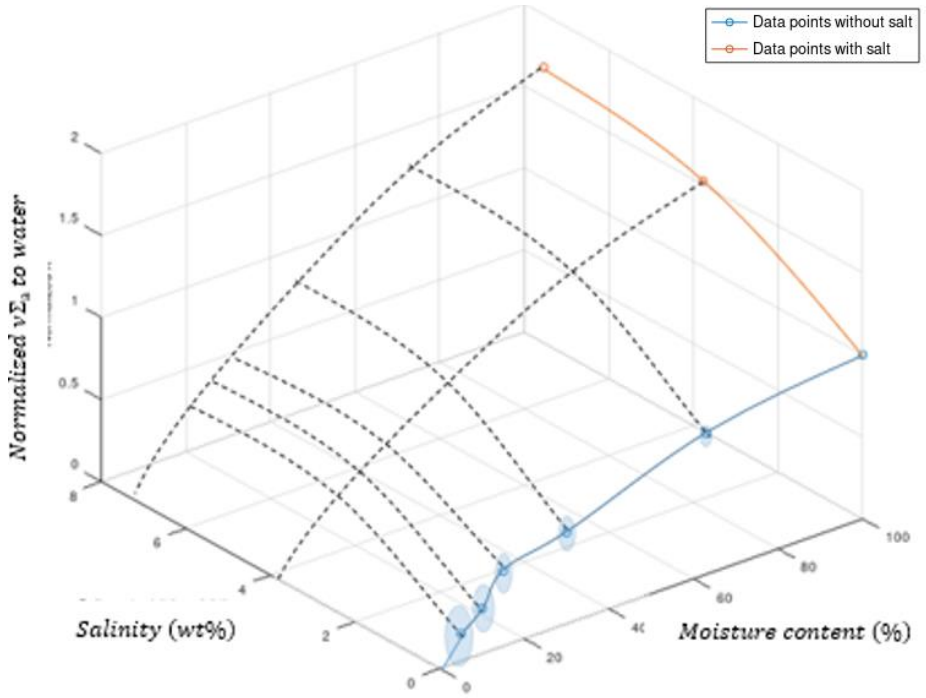

Figure 3.21 Salinity effects on $\nu\Sigma_a$.

3.4 Porosity and Moisture content

CNPL was discussed earlier as a method to infer porosity of a formation, equation (1.14). CNPL was formulated from two-group approach that described the thermal neutron flux $\emptyset$ at any location r:

$$\emptyset(r) = \frac{1}{4\pi Dr}\frac{L_t^2}{L_e^2 - L_t^2}\left(e^{-\frac{r}{L_e}} - e^{-\frac{r}{L_t}}\right) \tag{3.12}$$

, where L_e is the slowing-down length and L_t is the diffusion length of thermal neutrons. The counts N registering in a thermal sensor at the Near location r_N can be expressed by the following

$$N(r_N) = \frac{\varepsilon}{4\pi Dr_F}\frac{L_t^2}{L_e^2 - L_t^2}\left(e^{-\frac{r_N}{L_e}} - e^{-\frac{r_N}{L_t}}\right) \tag{3.13},$$

where ε is the efficiency of said sensor. Similarly, for the Far sensor at location r_F

$$N(r_F) = \frac{\varepsilon}{4\pi D r_F} \frac{L_t^2}{L_e^2 - L_t^2} \left(e^{-\frac{r_F}{L_e}} - e^{-\frac{r_F}{L_t}}\right) \quad (3.14),$$

where $r_F = r_N + \Delta r$. The ratio expressed in equation (1.7) can be written as

$$R = \frac{N(r)}{N(r+\Delta r)} \quad (3.15).$$

The sensitivity *S* to porosity *p* can then be written as

$$S = \frac{1}{R} \frac{\partial R}{\partial p} \quad (3.16).$$

The components that affects the sensitivity of CNPL was studied by Wu and published in the reference [67]. The result of that study identified the rate of change in L_e and L_t as function of porosity resulted in poor porosity sensitivity of D-T in CNPL tools. By placing the sensors at longer distances from the source, the component related to the rate of change of L_e and L_t yielded better porosity sensitivity [21]. The rate of change of L_e and L_t are influenced greatly by the starting neutron energy and the HI. The thermal neutron counts detected at the Near and Far neutron sensors are listed in Table 3.5.

Because thermal neutrons directly influence the population of 2.2 MeV gamma rays from hydrogen capture, CNPL was theoretically applicable to the 2.2 MeV net counts. Table 3.5 listed the neutron counts in each sensor and the associated errors. Table 3.6 listed the 2.2 MeV counts and the associated errors. Notice that 2.2 MeV counts are attenuated more in dense materials, , e.g. the limestone at 63% moisture has fewer 2.2 MeV counts than other matrices at lower moisture content. Hydrogen 2.2 MeV intensity increases with HI but the formation matrix also attenuates the 2.2 MeV. The associated ratio *R* is plotted in Figure 3.21.

Table 3.5 Thermal neutron counts at Near and Far sensor location and their ratio.

Experiment	Moisture content (%volume)	Near Neutron (counts)	Far Neutron (counts)	Near to Far Ratio
Nearly Dry Sand	~0	2,097,295 ± 1,448	660,896 ± 813	3.17 ± 00.045
Nearly Dry Limestone	>0	2,543,311 ± 1,595	415,450 ± 645	6.12 ± 0.0102
Partially Saturated Sand	15	3,555,483 ± 1,886	408,168 ± 639	8.71 ± 0.0144
Fully Saturated Sand	30	3,754,396 ± 1,938	411,631 ± 642	9.12 ± 0.0150
Fully Saturated Limestone	63	2,479,554 ± 1,575	406,712 ± 638	6.10 ± 0.0103
Water	98.3	2,746,577 ± 1,657	288,283 ± 537	9.53 ± 0.0187

Table 3.6 Hydrogen prompt capture counts at Near and Far sensor location and their ratio.

Experiment	Moisture content (%volume)	Bulk Density (g/cc)	2.2 MeV at Near (counts)	2.2 MeV at Far (counts)	Near to Far Ratio
Nearly Dry Sand	~0	1.6	24,567 ± 735	4,307 ± 270	5.70 ± 0.40
Nearly Dry Limestone	>0	2.5	55,545 ± 702	5,448 ± 241	10.19 ± 0.47
Partially Saturated Sand	15	1.7	78,145 ± 670	6,971 ± 227	11.21 ± 0.38
Fully Saturated Sand	30	1.8	76,995 ± 667	7,057 ± 225	10.91 ± 0.36
Fully Saturated Limestone	63	3.2	53,092 ± 693	6,068 ± 246	8.75 ± 0.37
Water	100	1	173,025 ± 628	13,960 ± 204	12.39 ± 0.19

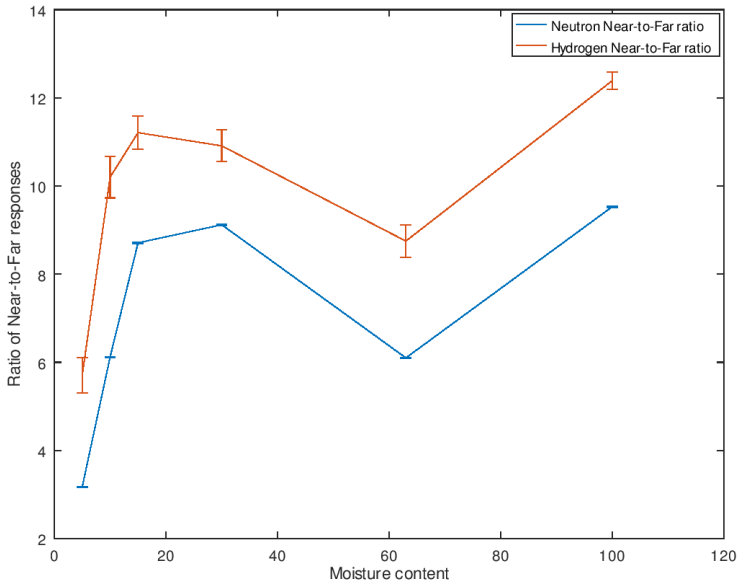

Figure 3.22 The ratio *R* from neutrons and 2.2-MeV gamma.

The profile of *R* matches that of the simulated results from references [15], [16], and [22]— except for the data point from limestone with 63% added moisture . The CNPL method result was appropriate in predicting the porosity to be around 10%. The limestone was very fine aggregate and porosity of 63% was not possible. Water was added to the limestone samples in two separate occasions. The first occasion, water was added until the formation was completely saturated with water as seen in Figure 3.23.

Figure 3.23 Water saturated limestone after the first fill.

A day after the first fill, the water disappeared from the test chamber and hence the second fill began. A total water volume of 63% of the test chamber was added to the limestone but the void fraction should remain relatively the same or less, as the extra weight and water movement could have packed the limestone tighter. The water disappearing could be explained by the limestone cycle of interaction with water, as depicted in the Figure 3.24. Clay minerals are known to form in the presence of water [68].

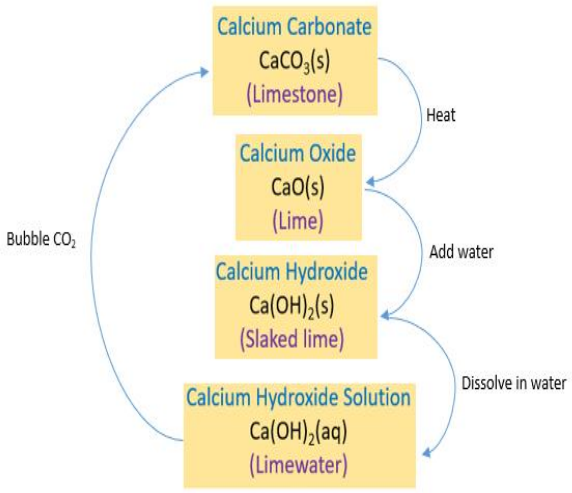

Figure 3.24. Limestone interaction cycle.

The actual density of each individual components in the limestone cycle within the test chamber was unknown. CNPL was a good method for low porosity estimates. Moisture content (or HI) added to the tank was best estimated by the sigma value $\nu\Sigma_a$, as shown in Figure 3.20. A comparison of CNPL and $\nu\Sigma_a$ were illustrated by plotting the normalized responses from each method against moisture content in Figure 3.25. Because the no other sources of hydrogen were present in the test chamber, the water volume added per test chamber volume is equivalently hydrogen index or hydrogen density. Combining the two methods, porosity and hydrogen index could be obtained with two NaI(Tl) sensors. Theoretically, the isotopic macroscopic cross section can be measured at various neutron speed ν, e.g. the 6.1 MeV oxygen inelastic scatter emission with neutron energy threshold at 8.5 MeV.

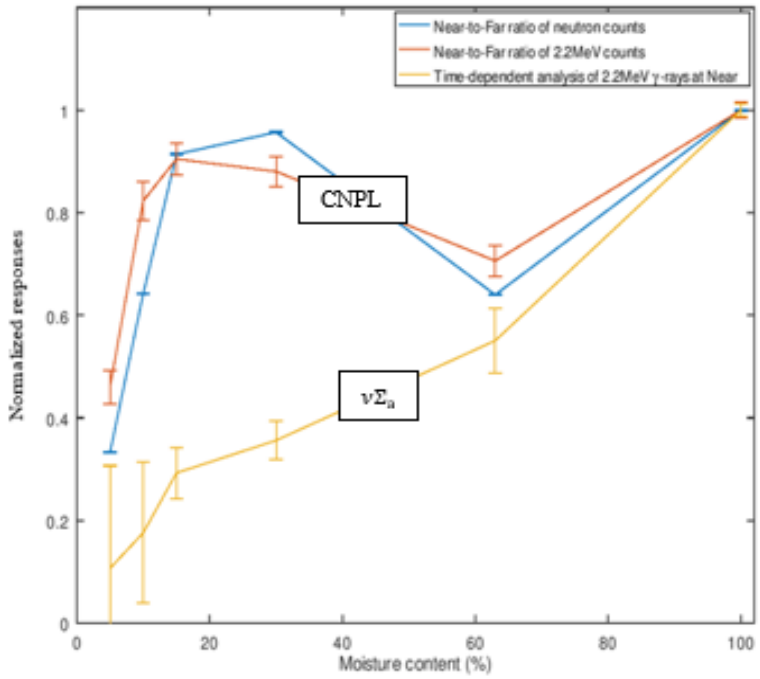

Figure 3.25 Comparison of CNPL and $\nu\Sigma_a$ vs. moisture content.

3.5 Lithology and Density: Distinguishing Sand and Limestone

Dry sand and dry limestone also influenced the thermal neutron population, but the effects from dry sand and dry limestone was not as significant as hydrogenous materials. The capture cross section value for sand was 4 c.u. and limestone was 7 c.u. compared to oil at 18 c.u., water at 22 c.u. and saline3.6%wt at 36 c.u. To distinguish between sand and limestone formation, the (n,p) reactions are observed instead of thermal capture (n,γ).

The reaction $^{28}Si(n,p)^{28}Al$ with a gamma ray at 1.78 MeV was observed in the Figure 3.26 denoted by the vertical red line. Silicon is present in sand but not much in limestone. The (n,p) reaction gamma appeared to be persistent through time. However, the gamma emission from $^{28}Si(n,p)^{28}Al$ was convoluted with another reaction $^{27}Al(n,\gamma)^{28}Al$. The aluminum capture reaction was a product of thermal neutrons. The total counts from each reaction were calculated and plotted against moisture content of each sample, as shown in Figure 3.27.

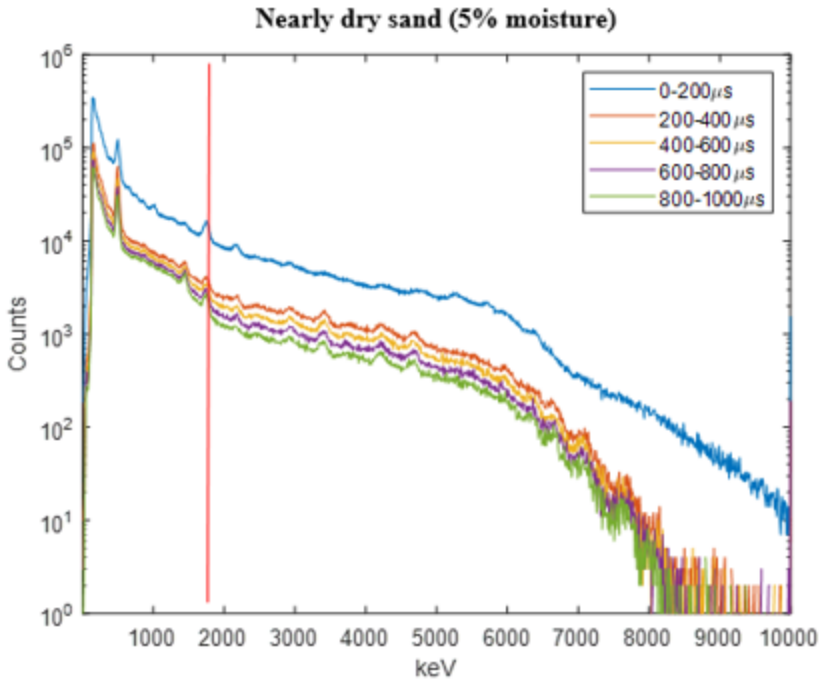

Figure 3.26 Spectra generated from five time gates.

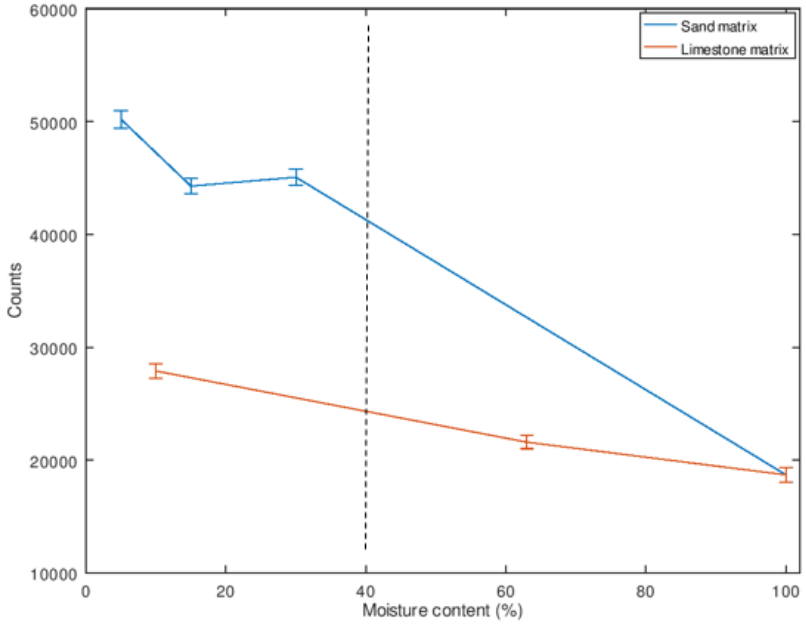

Figure 3.27 Gross counts from 1.78 MeV peak versus moisture content.

The gamma emission from ^{28}Al product has a half-life of 134.5 seconds. The decay time constant τ_a was not estimable in the 1,000 μs window between neutron bursts. Because the ^{28}Si(n,p)^{28}Al reaction was dependent on life-time neutrons, increasing presence of hydrogen

decreased the probability of ^{28}Si(n,p)^{28}Al occurring. Vice versa, the increased presence of hydrogen increases the ^{27}Al(n,γ) ^{28}Al. The cross section for the two reactions were plotted in Figure 3.28. Typical formations in the field have porosity much less than 40% so 1.78 MeV was concluded to be a good discriminator for sand and limestone. Cross section data for borehole logging and mineral analysis was published by IAEA [4].

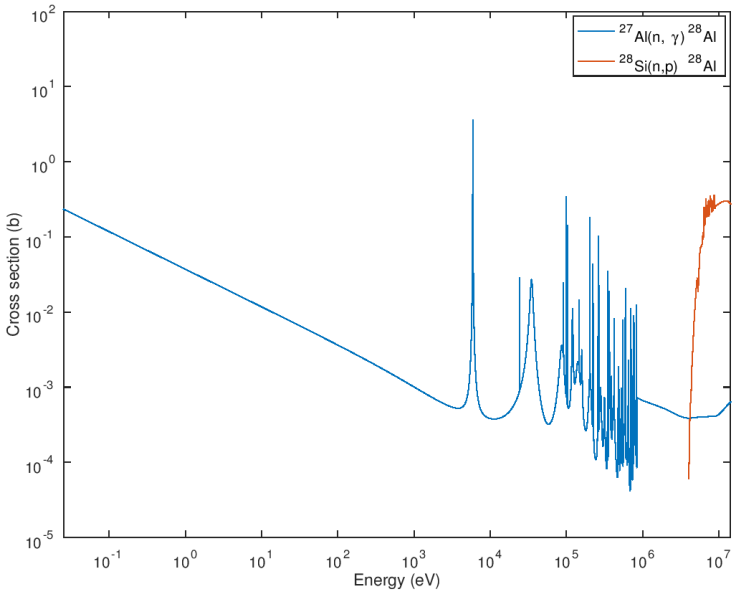

Figure 3.28 Cross sections for the ^{27}Al(n,γ) ^{28}Al and ^{28}Si(n,p)^{28}Al reactions. Data obtained from the National Nuclear Data Center (NNDC).

In theory, the isotopic macroscopic cross section for the silicon (n,p) reaction can be measured at various neutron speeds v. At 14.1 MeV, the cross section for ^{28}Si(n,p) ^{28}Al is $\Sigma_{(n,p)} =$ 0.28 barns and the neutron speed at 14.1 MeV is 52,000 km/s. This reaction rate is very fast compared to that of thermal neutrons at 2.2 km/s. However, the gamma emission of ^{28}Al has a half-life of 134.5 seconds which is outside of the observation window of 1,000 µs.

4 Simulations and MCLLS result

Simulations were performed to benchmark the prototype logging tool and facilities. The purpose of benchmarking the tool and facilities were to validate the experimental results. Once benchmarked the transport codes generated can be used to produce simulation studies with various neutron sources and configurations. MCNP was used in preliminary studies [57] and Geant4 was used toward the end of the five-year project. The use of MCLLS and machine learning for automated variable selection were demonstrated in section 4.2. As machine learning and computing power have advanced in recent years, machine learning algorithms have been employed by well log analyst to obtain unknown well parameters from known parameters [69] [70] [71].

4.1 Geant4 Simulations

Geant4 simulations were executed for the materials tested. The earlier model included the experimental room, the test chamber, the borehole, the sensor's detection material and the shielding. The simulated result from earlier model did not show agreement between measured data and simulated result. The tool skeleton and the sensors' electronic components were later added to produce an improved model. The D-T generator was modeled as a point isotropic source that was constantly emitting 14.1-MeV neutrons. The actual B322 D-T generator is 10% duty cycle at 1

kHz and 90º dominant emission. The Geant4 model did not model the cables and BNC connectors. Detail of the Geant4 result is described in the reference [72]. The dissertation author is the co-author in the reference [72]. Improvements in the model can be made but current Geant4 outputs presented in Figure 4.1 and 4.2 was encouraging.

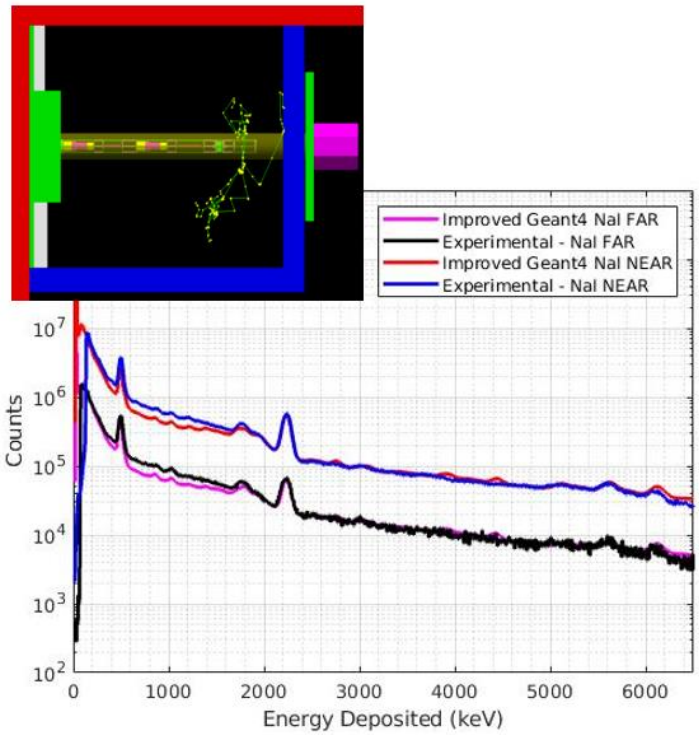

Figure 4.1 Geant4 water simulations vs. experimental response of the NaI(Tl) sensor. Upper left corner: The Geant4 model.

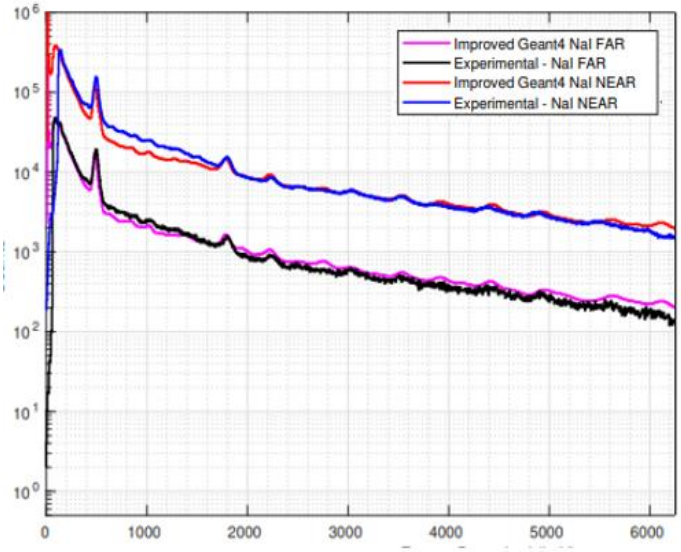

Figure 4.2 Geant4 sand(5%) simulations vs. experimental response of the NaI(Tl) sensor.

The "Nearly Dry Limestone" and "Nearly Dry Sand" samples had moisture contents that were unknown due to weather condition at the time of material delivery and loading. Geant4 simulations for sand sample with 5% moisture content was best matched the data from "Nearly Dry Sand" experiment. Similarly, for the "Nearly Dry Limestone", the experimental data best matched the simulated result for limestone with 10% moisture content.

4.2 MCLLS Results

DiNova from NCSU has published his dissertation on using MCLLS as a tool to solve the inversed MCLLS problem in well logging [73]. Supervised machine learning algorithms (Least Absolute Shrinkage and Selection Operator (LASSO) and Elastic Net) were used to automate the selection the variables (MC-generated elemental standard spectra) to fit experimental data. Vincent evaluated that LASSO generate responses that best fit the experimental data collected here. The linear least squares model is

$$\hat{Y} = \hat{\beta}_o + \sum_{j=1}^{p} \hat{x}_j \hat{\beta}_j \quad (4.1),$$

where $\hat{\beta}_o$ is the intercept, or the bias, and $\hat{Y}$ is the estimated spectrum, or the output. Vectors $\hat{x}_j$ are the standard spectra vectors, or the inputs, and $\hat{\beta}_j$ are the coefficients vector for the inputs. The above may be rewritten in the form:

$$\hat{Y} = \hat{X}^T \hat{\beta} + Error \quad (4.2)$$

where $\hat{X}^T$ is the transpose of $\hat{X}$ matrix that has the form $\hat{X} = [\hat{x}_1, \hat{x}_2, \hat{x}_3, \dots \hat{x}_p]$ and $\hat{\beta}$ is a vector of the form $\hat{\beta} = [\beta_1, \beta_2, \beta_3, \dots \beta_p]$. Fitting the linear model to a training set is possible by selecting β such that the sum of the residuals squared is minimized

$$Sum\ of\ squares\ = \sum_{i=1}^{N} \left(y_i - x_i^T \hat{\beta}\right)^2 \tag{4.3}$$

$$Sum\ of\ residual\ square = \sum_{i=1}^{N} \left(y_i - \beta_o - \sum_{j=1}^{p} x_{ij}^T \beta_j\right)^2 \tag{4.4}$$

,where y_i is counts in the ADC channel *i.* The ordinary least squares estimator can be computed by using the following equation

$$\hat{\beta}_{OLS} = (X^T X)^{-1} X^T Y \tag{4.5}.$$

The assumption is that sum of the weight of each standard is 1. The result research showed that the inverse MCLLS approach produces good agreement between experimental data and calculated results from supervised machine learning approach. DiNoVa found that LASSO gave better results than Elastic Net in selecting the variables [49]. Figure 62 below shows an example of LASSO results for the 100% water scenario. The LASSO and Elastic Net algorithms are in the Appendix C. The fit performance of LASSO can be seen in Figure 4.3 for the Far photon sensor.

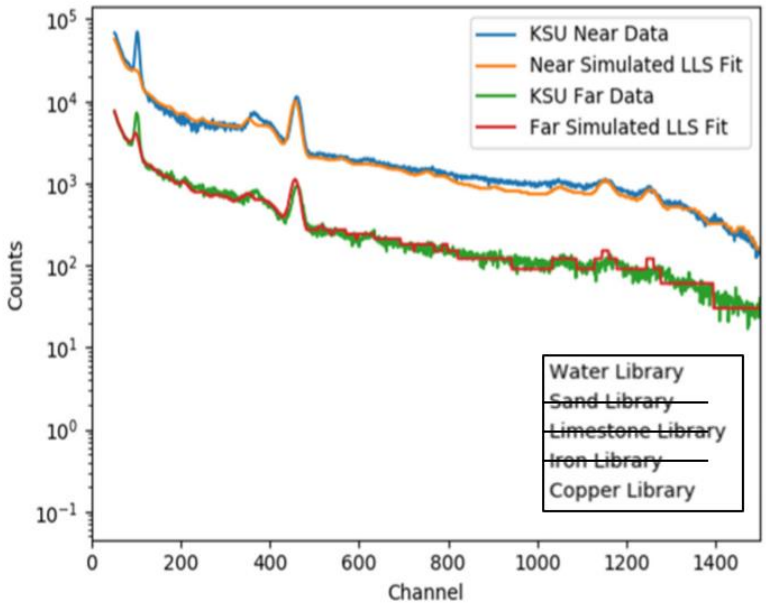

Figure 4.3 The fit for the 100% water data, with library selections from LASSO. Adapted from source [73].

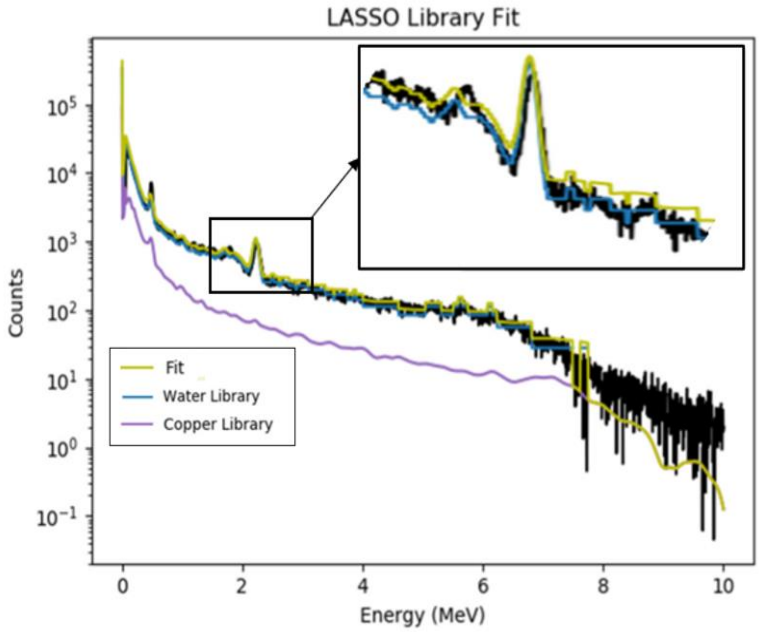

Figure 4.4 Variable selections from LASSO at the far sensor location. Adapted from source [73].

In the low energy range, the predicted intensity from the MCLLS approach was slightly underestimated when compared to that of the measured intensity. It was suspected a combination

of sensor activation, un-modeled scattering media and missing libraries were the causes. Activation of the NaI(Tl) was observed in the experiment. Figure 4.5 displayed the responses of the sensor after the experiments at time interval noted as Post-BG1 to 7.

Of interest in the low energy regime was a peak at approximately 0.5 MeV. The peak was expected to be a sum peak of boron-capture and annihilation gamma, due to the large presence of boron and the direct streaming of neutrons toward the borated sheets. Boron library was needed in LASSO variable selection. The LASSO algorithm predicted copper contribution. the copper contribution might be from the sensor's PMT dynode but did not fully make up for the missing intensity at 0.5 MeV. The next section investigates the "mystery peak" at 0.5 MeV. The identification was performed by breaking down the mystery peak into its possible contributors and their correlation to physical properties were analyzed.

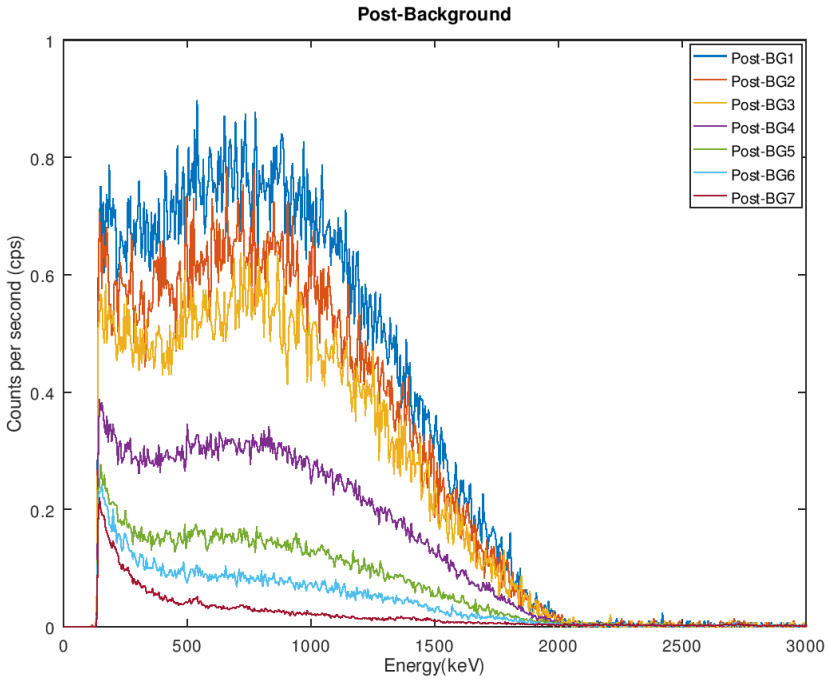

Figure 4.5 Post-irradiation background measurements for the Near NaI(Tl) showed decay activation.

4.3 Analysis of the 0.5 MeV sum peak

A fitting procedure and model were executed, and the result of the fit was plotted in Figure 4.6. The fit model was

$$\sum_{i=1}^{n=3} \frac{A_i}{\sqrt{2\pi\sigma_i^2}} e^{\frac{-(x-\mu_i)^2}{2\sigma_i^2}} + ax^2 + bx + c. \quad (4.6).$$

The value *n=3* denoted that the radiation energies within that sum peak was three (472, 478, and 511 keV). The model in equation (4.6) was used to estimate the contributions listed in Table 4.1.

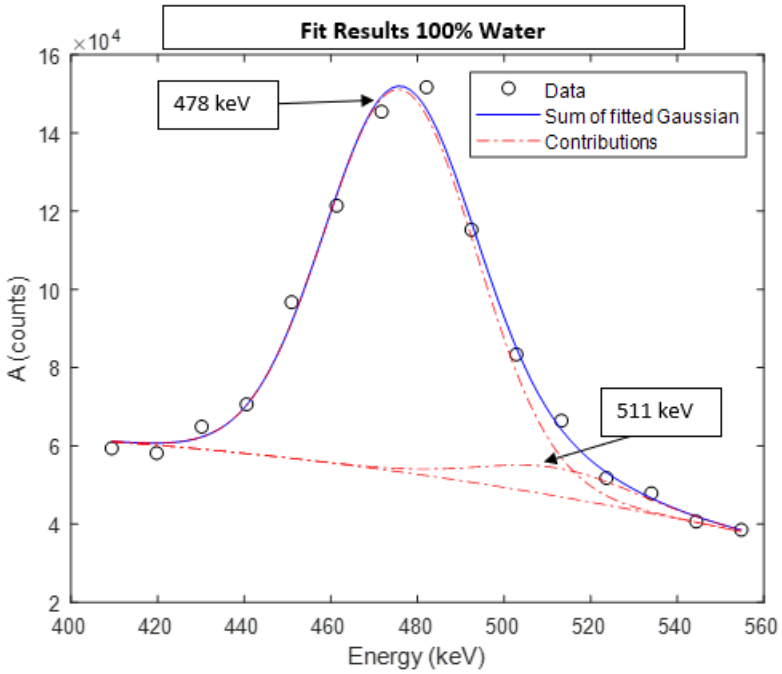

Figure 4.6 Fit for the model in equation (4.6).

Table 4.1 Fit result from the model in equation (4.6) with 95% confidence.

	A (counts)	**μ (keV)**	**FWHM (keV)**
Annihilation (511 keV)	32,400 ± 41,000	513.1 ± 24	39.2
Boron (478 keV)	412,000 ± 38,900	476.3 ± 1.8	38.1

Al-inelastic, Na-capture, Tl-capture (472 keV)	-13 ± 1E27	472.2 ± 1E28	36.9
Calibration (511 keV)		**511**	**36.9**

The major contributor for the 0.5 MeV sum-peak was from boron capture reaction. The second major contributor was from annihilation photons from pair production reaction. The contribution from the 472 keV was deemed insignificant, based on observation of the mean value of *A* and its associated uncertainty. FWHM did not match for the annihilation photon and the calibration reference 511 keV from ^{22}Na check source. Another model was fit to the data

$$\sum_{i=1}^{n=2} \frac{A_i}{\sqrt{2\pi\sigma_i^2}} e^{\frac{-(x-\mu_i)^2}{2\sigma_i^2}} + ax^2 + bx + c \qquad (4.7).$$

This model had *n=2,* denoting that the energies within the sum peak was two (478 and 511 keV). The fit result was plotted in the Figure 4.7. The model in equation (4.7) were used to estimate the contributions listed in Table 4.2.

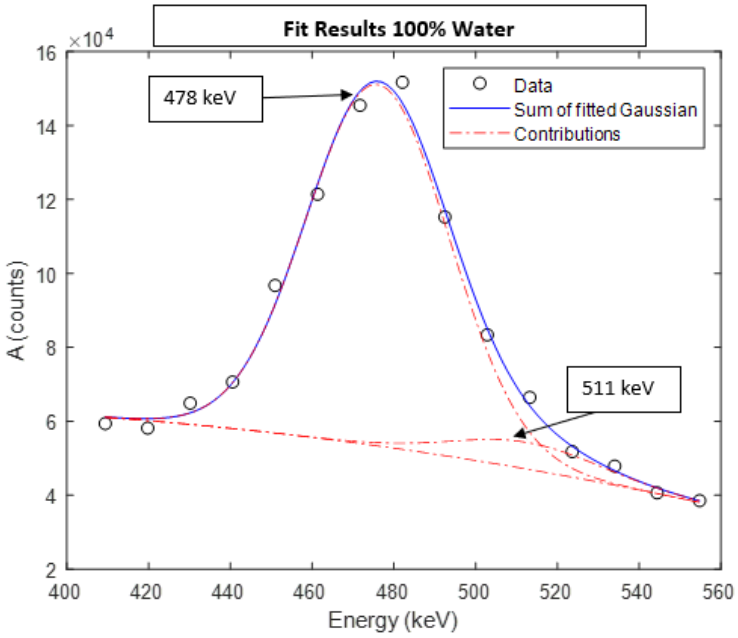

Figure 4.7 Fit for the model in equation (4.7).

Table 4.2 Fit result from the model in equation (4.7) with 95% confidence.

	A (counts)	**μ (keV)**	**FWHM (keV)**
Annihilation (511 keV)	32,600 ± 29,000	511.4	36.9
Boron (478 keV)	407,400 ± 28,980	476.3	37.0
Calibration (511 keV)		**511**	**36.9**

The fit result in from Figure 4.7 and Table 4.2 showed much better result. The FWHM matched for the annihilation photon and calibration 511 keV from ^{22}Na check source. The reduced chi-squared was calculated and equals to 1.25. The presence of boron was confirmed. The next task was to find out if the 511 keV and 478 keV gamma radiations had any correlation well log parameters. The Near NaI(Tl) time distribution of 478 keV from water experiment was plotted in Figure 4.8 for demonstration. Boron prompt capture had a time distribution that was resemblance of the neutron sensors at the Far location. The capture cross section Σ_a for boron was calculated to

be 56 c.u. No distinguishable relation to moisture content via decay time constant was observed due to the location of the boron (at the ends of the borehole).

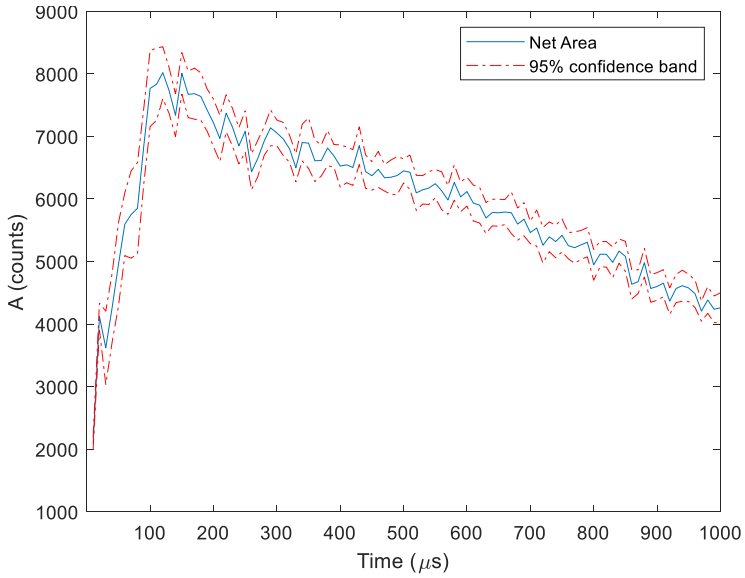

Figure 4.8 Boron capture 478 keV at Near NaI(Tl) in water.

For the annihilation radiation, at the Near NaI(Tl) sensor the counts are effectively zero for the time between 100 to 1,000μs for the 100% water sample. During the "ON" state, 0 to 100 μs, the annihilation photons mean counts and 95% confidence band are positive values, as seen in Figure 4.9. During the "ON" state, high energy neutrons of 14.1 MeV produces 511 keV annihilation photons.

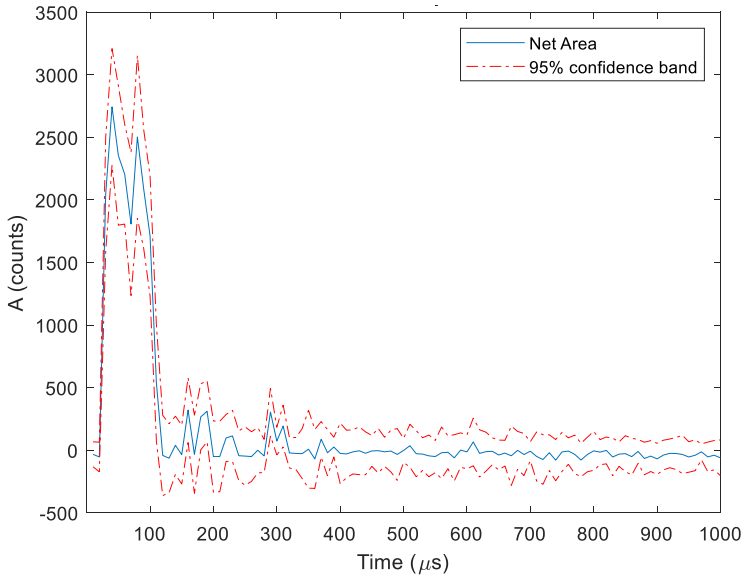

Figure 4.9 Annihilation 511 keV at Near NaI(Tl) in water.

The boron capture 478 keV were coming from the borated sheets used for shielding. These sheets were located around the test chamber. Table 4.3 listed the boron capture and the annihilation counts in each experiment. The data showed that boron capture counts were higher in the sand sample. This was because the mean distance the neutron can travel was larger in sand and more neutrons reached the walls of the test chamber where boron neutron capture occurred. The macro capture cross section for sand was 4 c.u. allowing more neutrons to reach the borated sheets. On the contrary, when the test chamber is filled with water, less boron-capture counts are observed. This was because the mean distance the neutron can travel was significantly less in water and less neutrons reached the borated sheets to produce the 478-keV radiation. The boron counts were a function of thermal neutron population that reached the ends of the test chamber. The test chamber was an effectively infinite medium thus most neutrons reaching the boron-lined walls had to travel through the air-filled borehole. When moisture increased from 5% to 10%, the boron counts dropped significantly.

Table 4.3 Boron and annihilation counts and 68% confidence at the Near NaI(Tl) for each experiment.

Experiment	Moisture content (%volume)	Bulk Density (g/cc)	Boron neutron-capture (counts)	Annihilation photons (counts)
Nearly Dry Sand	5	1.6	734,170 ± 36,782	100,660 ± 36,784
Nearly Dry Limestone	10	2.5	516,910 ± 30,674	127,480 ± 30,642
Partially Saturated Sand	15	1.7	531,610 ± 20,923	74,501 ± 20,918
Fully Saturated Sand	30	1.8	533,070 ± 22,712	79,368 ± 22,719
Fully Saturated Limestone	63	3.2	395,020 ± 14,351	36,241 ± 13,967
Water	100	1	407,400 ± 14,490	32,600 ± 14,500
Saline (3.6%wt)	98.3	1.04	271,010 ± 12,819	84,393 ± 12,833

The boron capture counts were similar for the limestone and sand samples in the moisture range of 10% to 30%. The capture cross section for sand and limestone were close, between 5 to 10 c.u., as compared to water's 22 c.u., thus at low moisture content production of 478 keV were similar. Note that the sand sample at 15% moisture was not homogeneous, adding a complexity to which 478 keV was generated.

High density and low moisture content materials were observed to produce more 511 keV. The data from Table 4.3 showed counts of 511 keV at 100,660 and 127,480 for sand 1.6g/cc and limestone 2.5 g/cc. The data from Table 4.3 also showed that the present of moisture content reduced the number of 511 keV in the same formation. The most drastic difference was in water and saline's 511 keV counts. Saline 3.6%wt produced three times more 511 keV than water. The difference was observed in 478 keV also, where saline3.6%wt produced 140,000 less 478 keV counts than water. The time distribution of 5111 keV for sand and limestone was plotted in the Figure 4.10.

Boron use was reported in the reference [74] in a C/O logging tool to study porosity. In that study two boron lined NaI(Tl) sensors were used to estimate porosity. The CNPL method was used to estimate porosity by taking the ratio of boron capture 478 keV from the two sensors. The Near sensor was 1×4 inch and the Far was 1×6 inch. The 2-mm lining reduced epithermal and thermal neutron current produced from D-T reactions by two orders of magnitude. Like the findings in this section, the study found a sum peak of both 511 keV and 478 keV. The two signatures were not isolated in the referenced study, and the sum peak counts were used in estimating porosity.

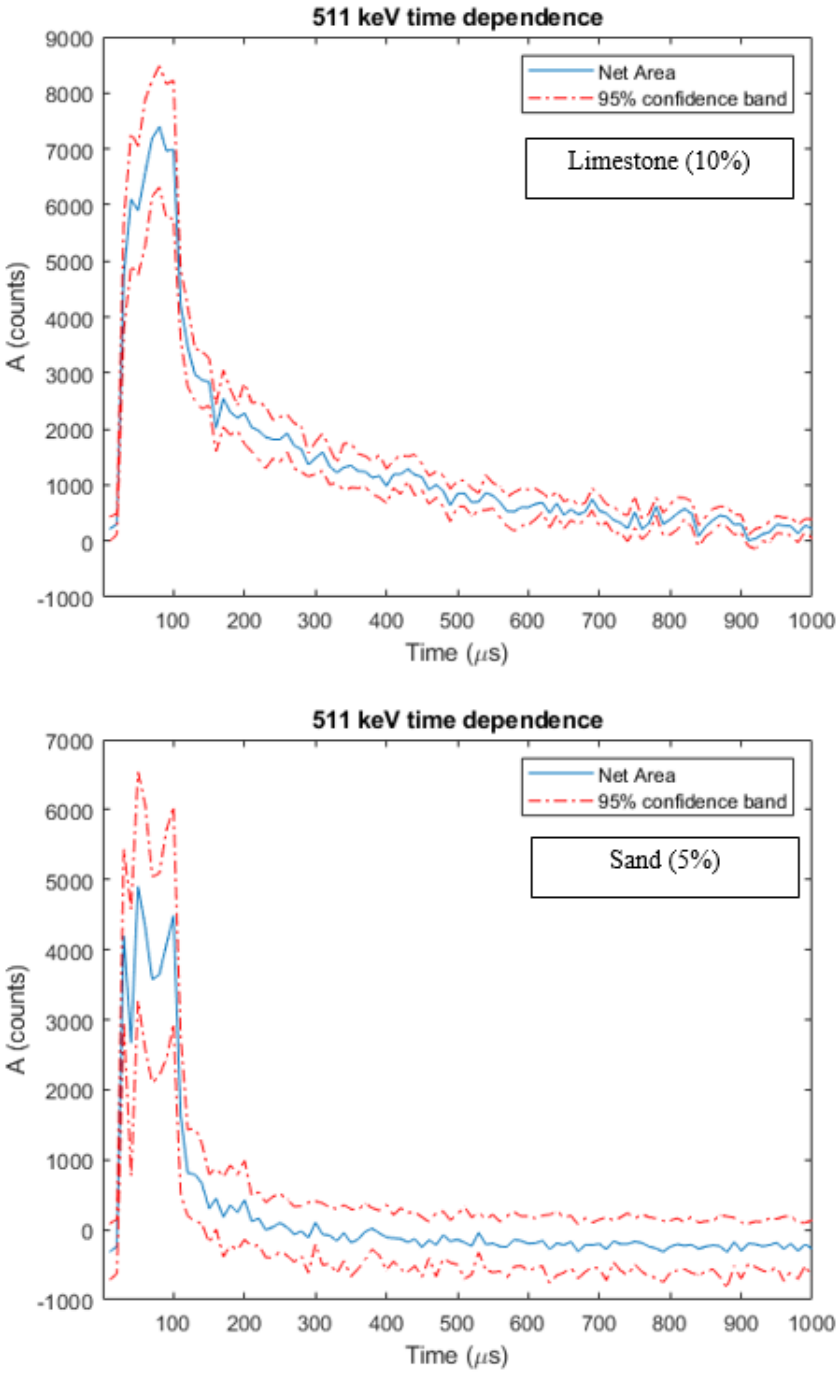

Figure 4.10 The time distribution of 511 keV for sand and limestone at Near NaI(Tl).

5 Summary and Conclusion

5.1 Summary

The Consortium for Nonproliferation of Enabling Capabilities (CNEC) was established to investigate four thrust areas. One of those thrust areas was the Replacement of Dangerous Radiological Sources. The term “dirty bomb” refers to a conventional explosive coupled with one or more radionuclides. When denotated, “dirty bombs” cause immediate injuries and expose the intended targets as well as bystanders to radiation. After 9/11, the United States Congress initiated a series of action to assess the nation’s vulnerabilities. One vulnerability was associated with the advancement in technologies involving radiation. Congressed asked the National Research Council (NRC) to form a committee that would conduct studies to consider the current radionuclide source uses. The committee set out to hear from experts on the radiation source applications and examined the hazards associated, including both accidentals and malevolent acts. The result of the NRC study was published in 2008 in a comprehensive report. This report identified two radiological sources, ^{137}Cs and Am-Be, as among the most dangerous due to their widespread use, particularly in well logging and gauging applications.

^{137}Cs is the most important contributor to environmental dose received by human. Cesium chloride salt can be easily dispersed in dirty bombs. When in solution, it can be taken up by plants

and assimilated by animals because of its chemical similarity to the essential nutrient Potassium. In most applications, highly dispersible CsCl can be replaced with other forms of radionuclides or non-radionuclides such as particle accelerators but feasibility is a concern in those situations. In recent years, researchers in the industry and academia have started to examine the potential of compact accelerator sources as alternatives to radionuclides ^{137}Cs and Am-Be.

Kansas State University (KSU) was a member CNEC and was studying the replacement of dangerous radiological sources (RDRS) in well logging. RDRS prioritized search for the replacements or alternatives sources in well logging. Well logging industry employs a method called Compensated Neutron Porosity Logging (CNPL) in conjunction with Am-Be to obtain porosity estimates. The CNPL method was expected to underperform with a D-T neutron source. On the other hand, D-T had proven to be a viable neutron source in other geochemical logging tools for multi parameter estimates. The same characteristics that made D-T neutron sources attractive in elemental composition analysis also made D-T less attractive in porosity estimates. The 14.1 MeV neutrons from D-T have undesirable slowing down characteristics for the CPNL measurement at short source-to-sensor distances.

This dissertation explored the utility of D-T accelerator as a neutron source for estimating well log parameters and how various source-to-sensor and environmental effects influenced those parameters. The efforts included the construction of a test facilities and prototype logging tool. The construction of the test facilities and tool was detailed in Chapter 2. The prototype logging tool was used to collect measurements from experiments at the test facilities. Experiments were performed at King Hall Annex facilities, where a large 2,500-gallon test chamber was filled with materials such as sand, limestone, water and saline. Measurement were collected at various moisture levels where water was a surrogate for hydrocarbons. The prototype logging tool

employed two standard NaI(Tl) sensors (Near and Far) and two thermal neutron sensors (one is ^{3}He and the other is BF_3).

5.2 Conclusions

The results from the experiments confirmed the poor porosity estimates of D-T when CNPL at Am-Be source-to-sensor distances (reduced range of sensitivity to porosity). The poor porosity range can be improved by increasing source-to-sensor distances. A novel approach was introduced in this work to estimate hydrogen index—An analysis that quantified several reaction rates and correlated those reactions with salinity, density, and moisture content. Detail experimental analyses, observations and drawn conclusions could be found in Chapter 3. Theorical formalisms of the neutron interactions in well logging were also described in Chapter 3. Fast neutron slowing down directly influenced the gamma (e.g. thermal capture and inelastic scatter) population in each sample and observations of those samples reflected that. Diffusion of thermal neutrons also affected the gamma ray count rates. Thermal neutrons cloud stayed closer to the D-T source in water samples because of small diffusion coefficient and the thermal neutrons were also reflected into the borehole where the sensors were. Moreover, the low absorption cross section of the borehole accumulated neutrons inside the boreholes. The result was that the borehole acted as neutron sink and influenced the decay rate of thermal neutron observed by the neutron sensors. The macroscopic capture cross section Σ_a or the decay time τ_a from the Near and even Far neutron sensor was strongly influenced by the borehole effect.

To overcome the borehole effect, the macroscopic capture cross section Σ_a of samples was measured from hydrogen 2.2 MeV decay time τ_a. The experimentally derived Σ_a agreed with the theoretical values of Σ_{int} and appeared to be free of borehole effects. The borehole effect was less

influential because the borehole contains no hydrogen. In practice, the borehole sometimes contains mud and fluids that has hydrogen. Considerations needed to separate those hydrogen signatures from the borehole fluids and mud.

The result introduced the novel use of 2.2 MeV gamma to infer macroscopic capture cross sections of bulk media. The result can be found in Chapter 3. The Σ_a values showed a nearly linear relationship with moisture content of the test chamber. The measured macroscopic cross section from hydrogen has a drawback which was its large uncertainty in low HI environment. Salinity of a formation was the most influential on sensor responses due to the large thermal capture cross section of salt. Capture cross section of saline at various salt concentrations was studied. High salinity solution resulted in more dominant borehole component and poor macroscopic capture estimate when using neutrons. The saline3.6%wt concentration was correctly estimated by the measured Σ_a from 2.2 MeV decay. Matrix types were observed via silicon (n,p) reaction and the emitted gamma signature were deemed a good discriminator between sand and limestone matrices up to 40% moisture content. In theory, the decay of silicon (n,p) and (n,γ) at 1.78 MeV can be used to estimate the fast and thermal capture cross section if the time window of observation were longer and at much larger source intensity.

5.3 Outlook

The generator was operating at 1% of its maximum capability producing approximately 10^6 neutrons per second. The lower neutron yield was compensated by a longer measurement of 3,300 seconds. The same result could be obtained in 5 minutes if the generator were operating at 10^8 neutron per second.

The low resolution of NaI(Tl) sensor resulted in limited number of peaks that could be studied. Three peaks from for five reactions were studied in this dissertation. The sensor low resolution required deconvolution of the sum peaks. In future work, high resolution should be considered. Another limiting factor for hydrogen time analysis is the counting rate limit of NaI(Tl) at approximately 500,000 counts per second. The counting rate limit of NaI(Tl) is a constraint for the fast logging speed of Logging-While-Drilling tools at 2ft/s. Even in slower speed, the measurement time is typically in seconds. To apply time analysis for hydrogen successfully, a detector of counting rate limit needs to be at least $\times 1000$ times faster than NaI(Tl) to reduce uncertainty (especially in the low HI environments). In low HI environment, source intensity should be at least 10^{10} neutron per second to obtain enough 2.2 MeV counts (with net peak counts error less than 1%) for measurement duration of few seconds.

D-T is a promising accelerator-based neutron generator for bulk material characterization. The tools employing D-T can provide a wide range of parameters. Increased utilization and research efforts of the accelerator-based options appear to have significant impact and align with the United States of America mission to reduce the radionuclide source uses.

6 Works Cited

[1] B. D. Berger and K. E. Anderson, Modern Petroleum: A Basic Primer of the Industry, Tulsa: PennWell Books, 1992.

[2] D. V. Ellis and J. M. Singer, Well Logging for Earth Scientists, Springer, 2007.

[3] O. Serra, Fundamentals of well-log interpretation, Amsterdam, Netherlands: Elsevier, 1984.

[4] IAEA, Handbook on Nuclear Data for Borehole Logging and Mineral Analysis, Vienna: IAEA, 1993.

[5] IAEA, "Neutron Generators for Analytical Purposes," *International Atomic Energy Agency*, 2012.

[6] J. K. Shultis, Fundamentals of Nuclear Science and Engineering, CRC Press, 2017.

[7] N. Tsoulfanadis, Measurement & Detection of Radiation, CRC Press, 2010.

[8] R. Garrels and F. MacKenzie, Evolution of sedimentary rocks, New York: W. W. Norton, 1971.

[9] R. Evans, The Atomic Nucleus, New York: McGraw-Hill, 1967.

[10] J. H. Hubbell and S. M. Seltzer, "X-Ray Mass Attenuation Coefficients," 29 7 1996. [Online]. Available: https://physics.nist.gov/PhysRefData/XrayMassCoef/ComTab/water.html.

[11] J. R. Lamarsh and A. J. Baratta, Introduction to Nuclear Engineering, Upper Saddle River: Prentice-Hall, 2001.

[12] R. J. e. a. Radtke, "A New Capture And Inelastic Spectroscopy Tool Takes Geochemical Logging Tool To The Next Level," *Society of Petrophysicists and Well Log Analyst,* 2012.

[13] A. Badruzzaman, "An Assessment of Fundamentals of Nuclear-based Alternatives to Conventional Chemical Source Bulk Density Measurement," *Petrophysics,* p. 55, 2014.

[14] L. S. Allen, "Dual-Spaced Neutron Logging for Porosity," *Geophysics,* vol. 32, no. 1, 1967.

[15] C. M. Frankle and G. E. Dale, "Unconventional Neutron Sources for Oil Well Logging," *Nuclear Instrumentations and Methods in Physics Research A,* 2013.

[16] C. R. Peeples, "On Replacing Am-Be Neutron Sources in Compensated Neutron Porosity Logging tools," *Applied Radiation and Isotopes,* pp. 926-931, 2010.

[17] W. Wu, "Porosity Sensitivity Study of the Compensated Neutron Logging Tool," *Journal of Petroleum Science and Engineering,* 2013.

[18] A. Mohamed, "A dense plasma focus device as a pulsed neutron source for material identification".

[19] A. Badruzzman, "The ubiquitous neutron/density tool response in petro-free mud," in *Proc. 46th SPWLA Annual Symposium*, New Orleans, 2005.

[20] J. Liu, "A Method to Improve the Sensitivity of Neutron Porosity Measurement Based D-T Source," *Journal of Natural Gas Science and Engineering*, pp. 879-884, 2016.

[21] L. Xu, "A Comprehensive Investigation of Source Effects on Neutron Porosity Response for Logging-While-Drilling Measurements," *Petrophysics*, pp. 185-198, 2010.

[22] A. X. Chen, "Electronic neutron sources for compensated porosity well logging," *Nuclear Instrumentations and Methods in Physics Research A*, pp. 52-56, 2012.

[23] A. Badruzzaman, "An assessment of Fundamentals of Neutron Porosity Interpretation: Americium-Beryllium Source versus Neutron Gnerator-Based Alternatives," *SPWLA 58th Annual Logging Symposium*, 2017.

[24] M. Evans, "A Sourceless alternative to conventional LWD nuclear logging," *Society of Petroleum Engineer Annual Technical Conference and Exhibition*, 2000.

[25] J. A. Grau, "Absolute Elemental Concentrations Estimated from Geochemical Well Logging Using Neutron-Induced Gamma-Ray Spectrometry and a Geological Model," *AAPG*, vol. 71, 1987.

[26] J. S. Wahl, "The Thermal Neutron Decay Time Log," *Society of Petroleum Engineers*, vol. 10, 1970.

[27] E. Ortega, "Multidetector LWD SIgma Logging Principles, Petrophysical Applications, and Environmental Effects," *SPWLA 54th Annual Logging Symposium,* 2013.

[28] D. Rose, "An innovative slim pulsed neutron loggign tool," *SPWLA 56th Annual Logging Symposium,* 2015.

[29] T. Zhou, "Fast neutron cross-section measurement physics and appications," *SPWLA 57th Annual Logging Symposium,* vol. 2016.

[30] A. C. Kak, "Principles of Computerized Tomographic Imaging," *IEEE Vol 33,* 1988.

[31] A. Dhawan, Medical Image Analysis, Wiley, 2011.

[32] B. P. Fairand, Radiation Sterilzation for Health Care Products, CRC Press, 2001.

[33] S. Lerouge and A. Simmons, Sterilisation of biomaterials and medical devices, Woodhead Publishing, 2012.

[34] J. Presas and C. G. Krishnadas, Non-Destructive Test and Evaluation of Materials, New Delhi, India: Tata McGraw Hill, 2008.

[35] W. E. Gardner, Improving the Effectiveness and Reliability of Non-Destructive Testing, Pergamon Press, 1992.

[36] R. P. Gardner and R. L. Ely, Radioisotopes Measurement Applications in Engineering, Reinhold Publishing, 1967.

[37] W. L. Dunn and T. L. Davis, "Tracer measurement of service water flow rates at an operating power plants," *Nuclear Methods in Environmental and Energy Research,* 1977.

[38] NRC, "Radiation Use and Replacement," *National Academies Press,* 2008.

[39] NCRP, "Cesium-137 in the Environment: Radioecology and Approaches to Assessment and Management," 2006.

[40] S. C. Vogel, "Short Pulse Laser Driven Moderated Neutron Source," *EPJ,* 2020.

[41] W. L. Dunn and J. K. Shultis, "Monte Carlo methods for design and analysis radiation detectors," *Radiation Physics and Chemistry 78,* 2009.

[42] W. L. Dunn, "Inverse Monte Carlo analysis," *J. Comput. Phys.* , pp. 154-166, 1981.

[43] W. L. Dunn, "Inverse Monte Carlo solutions for radiative transfer in inhomogeneous media," *J. Quant. Spectrosc. Radiat. Transfer 29,* pp. 19-26, 1983.

[44] W. L. Dunn and J. Womersley, "Solutions of inverse and optimization problems in high energy and nuclear physics using inverse Monte Carlo," *International conference Monte Carlo Simulation in High Energy and Nuclear Physics. World Scientific,* 1994.

[45] R. P. Gardner, "Status of software for PGNAA bulk analysis by the Monte Carlo-Library Least Squares (MCLLS) approach," *Journal Radioanalytical and Nuclear Chemistry 264,* pp. 221-228, 2005.

[46] C. J. Werner, "MCNP User Manual," LA-UR-1729981, Los Alamos National Laboratory, 20017.

[47] Agostinelli, "GEANT4 a Simulation Toolkit," *Nuclear Instrumentations and Methods in Physics Research A,* vol. 506, no. 3, pp. 250-303, 2003.

[48] M. Pinilla, "Shielding Design for Kansas State University Material Interrogation Facility," *The 3rd International Conference on Dosimetry and Its Applications,* 2019.

[49] A. Nikitin and S. Bliven, "Needs of Well Logging Industry in New Nuclear Detectors," *IEEE Nuclear Science Symposium & Medical Imaging Conference,* 2010.

[50] A. Pemper, "A New Pulsed Neutron Sonde for Derivation of Formation Lithology and Mineralogy," *SPE Annual Technical Conference and Exhibition,* 2006.

[51] J. Galford, "A New Neutron-Induced Gamma Ray Spectroscopy Tool for Geochemical Logging," *SPWLA 50th Annual Logging Symposium,* 2009.

[52] G. Hou, "Development of Sensor Physics for a Nuclear Oil Well Logging Tool," ProQuest Dissertation and Theses, 2017.

[53] D. McGregror, "Materials for Gamma-Ray Spectrometers: Inorganic Scintillators," *Annual Review of Materials Research,* pp. 245-277, 2018.

[54] P. Mitra, "Application of SPectrum Shifting Methodology to REstore NaI(Tl) Recorded Gamma Spectra, Shifted Due to Temperature Variations in the Environment," *Applied Radiation and Isotopes,* vol. 107, pp. 133-137, 2016.

[55] M. Ellis, "Activation of Sodium Iodide Detectors in an Active Interrogation Environment," *IEEE Nuclear Science Symposium and Medical Imaging Conference Record,* pp. 11-17, 2012.

[56] R. P. Gardner, "NaI Detector Neutron Activation Spectra for PGNAA Applications," *Applied Radiation and Isotopes,* pp. 483-497, 2000.

[57] M. Pinilla, "An MCNP simulation study of an oil well logging benchmarking tool and a test enclosure," Kansas State University, Manhattan, KS, 2019.

[58] R. Gardner and A. Sood, A Monte Carlo simulation approach for generating NaI detector response functions (DRFs) that accounts for non-linearity and variable flat continua, Nuclear Instrumentation and Methods in Nuclear Physics B, 2004.

[59] W. E. Schultz, "Experimental basis for a new borehole corrected pulsed neutron capture logging system," *Trans SPWLA/CWLA 24th Annual Logging Symposium,* 1983.

[60] P. D. Wraight, "Thermal decay time loggign method and apparatus". US Patent US4721853A, 1987.

[61] M. Mahdavi and S. Sitaraman, "Thermal decay time logging method and tool". US Patent US497040A, 1989.

[62] T. Zhou, "System and methods to determine relative elemental concentration from nuclear spectrosopy". Sugar Land, TX Patent 10473813, 2019.

[63] L. Vo, Development of Test Facilities for Studies Relevant to Replacing Dangerous Radiological Sources, AIP Proceedings, 2019.

[64] L. Vo, TIme dependent signatures: Moisture content interpretation in well logging applications with a D-T neutron generator, Nuclear Instrumentations and Methods in Physics Research B, 2020.

[65] MATLAB, "Equation Solving Algorithms," MATLAB, [Online]. Available: https://www.mathworks.com/help/optim/ug/equation-solving-algorithms.html. [Accessed July 2020].

[66] R. David, "Solving for reservoir saturations using multiple formation property measurements from a single pulsed neutron logging tool," *SPWLA 58th Annual Logging Symposium*, 2017.

[67] W. Wu, Porosity Sensitivity Study of the Compensated Neutron Porosity Logging Tool, Journal of Petroleum Science and Engineering, 2013.

[68] P. F. Kerr, "Formation and Occurrence of Clay Minerals," *Clays and Clay Minerals,* no. http://www.clays.org/journal/archive/volume%201/1-1-19.pdf.

[69] T. Deng, "A comparative study of three supervised machine learning algorithms for classifying carbonate vuggy facies in Kansas Arbuckle formation," *SPWLA* , 2019.

[70] L. Lawal, "Total Organic Carbon Characterization Using Neural Network of XRF data," *SPWLA,* 2019.

[71] Y. Orunganti, "Role of Machine Learning in building models for gas saturation prediction," *SPWLA,* 2019.

[72] S. Sharma, Bulk material interrogation experimental results and validation for replacement of dangerous radiological sources in well logging industries, Submitted Non-Destructive Testing.

[73] V. DiNoVa, Automated Variables selections of Gamma Ray Spectra by Utilization of LASSO and Elastic Net Techniques for Use in Nuclear Security Applications, ProQuest Dissertation and Theses, 2019.

[74] W. Metwally, Porosity Calculations using a C/O logging tool with boron-lined NaI detectors, Applied Radiation and Isotopes, 2011.

6.1 Appendix A – Applications of neutron generators

Field	Category	Neutron Generator	Existing Applications	Isotopes
Security	Explosives detection	D-T	Cargo/Luggage inspection	C,O,N
	Chemical weapon	D-T	Inspection	N,P
	Drugs	D-T, DPF	Border Inspection	C,O,N
Safeguards	Nuclear material detection	D-D	Fission products detection	U
Industrial	On-line analyzer	D-T, D-D	Cement process monitoring, coal and mining	Ca, Si, Fe, Al
	Metal cleanliness and impurity quantification	D-T	Oxide detection Contaminant detection	Mg, Al, Al, Steel,
Medical	Body screening	D-T	Body indexing	C, O, N, Ca, Na, Cl, P
Nutrition	Protein content	D-T	Nitrogen detection	N
Environmental	Recycled Materials	D-D	Inspection	Cd, Hg, Br, Cl
	Radiography	D-D	Water content	H
	Pesticides	D-D	Halogen detection	Br, Cl
Geological	Analyzer	D-T, D-D	Ash value of coal	Si, Al, C, H, Fe, Ca, S
	Oil exploration	D-T, D-D	Lithology, porosity	H, C, O, Ca, Si

6.2 Appendix B – Some signatures of interest when using 14.1 MeV neutrons for irradiation.

Element	Reaction	Half-life	Gammas (MeV)	Sensitivity (10^6 decay $s^{-1}g^{-1}$)
B	$^{11}B(n,p)^{11}Be$	13.8 s	2.13	15
O	$^{16}O(n,p)^{16}N$	7.13 s	6.13, 7.12	1.3
N	$^{14}N(n,2n)^{13}N$	9.97 min	0.511	15
Al	$^{27}Al(n,p)^{27}Mg$	9.46 min	0.844	1.6
Si	$^{28}Si(n,p)^{28}Al$	2.25 min	1.78	4.5
P	$^{31}P(n,\alpha)^{28}Al$	2.25 min	1.78	2.3
Cu	$^{63}Cu(n,2n)^{62}Cu$	9.74 min	0.511	3.6
Br	$^{79}Br(n,2n)^{78}Br$	6.5 min	0.614	3.7
Ag	$^{109}Ag(n,2n)^{108}Ag$	2.37 min	0.633	2.3
Ba	$^{138}Ba(n,2n)^{137}Ba$	2.55 min	0.662	3.7

6.3 Appendix C – LASSO algorithm

LASSO methods utilize tuning parameters to shrink and select variables and LASSO is defined as:

$$\hat{\beta}^{lasso} = \underset{\beta \in \mathbb{R}^p}{argmin} \, ||y - X\beta||_2^2 + \lambda \sum_{j=1}^{p} |\beta_j|$$

$$= \underset{\beta \in \mathbb{R}^p}{argmin} \, ||y - X\beta||_2^2 + \lambda ||\beta||_1$$

Where,

- $||y - X\beta||_2^2$ is the loss function
- $\lambda ||\beta||_1$ is a tuning parameter that serves as a penalty

6.4 Appendix D – Elastic Net algorithm

The Elastic Net method select variables using the penalty terms used in LASSO and Ridge Regression as:

$$\hat{\beta}^{ElasticNet} = \underset{\beta \in \mathbb{R}^p}{argmin} \, ||y - X\beta||_2^2 + \lambda_2 ||\beta||_2^2 + \lambda_1 ||\beta||_1$$

Where,

- $||y - X\beta||_2^2$ is the loss function
- $\lambda_1 ||\beta||_1$ is a tuning parameter that serves as a penalty from LASSO
- $\lambda_2 ||\beta||_2^2$ is a quadratic tuning parameter that serves as a penalty from Ridge Regression

6.5 Appendix E – Time Dependent plots the 478 keV

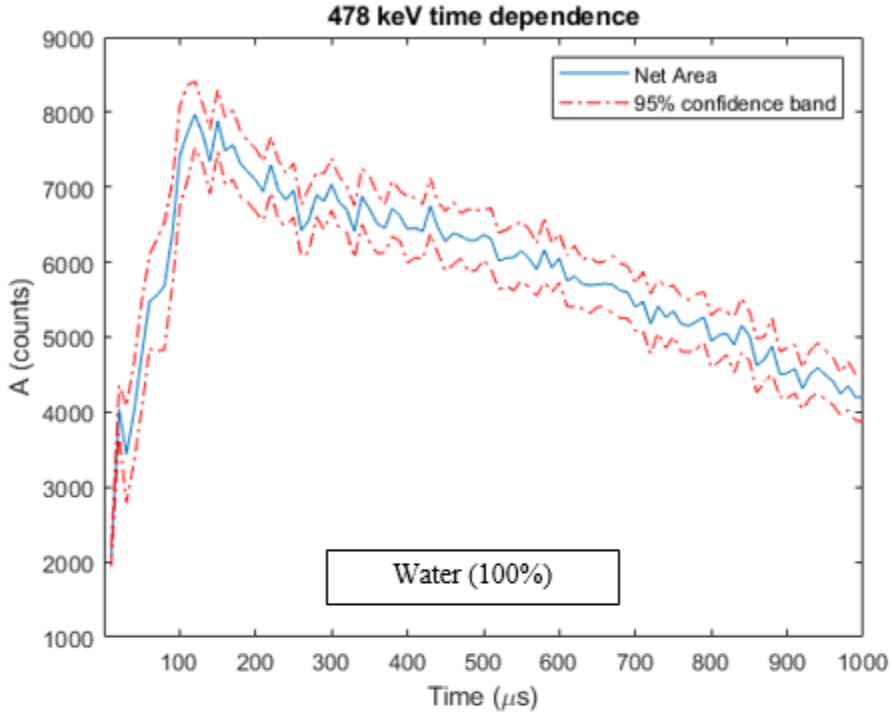

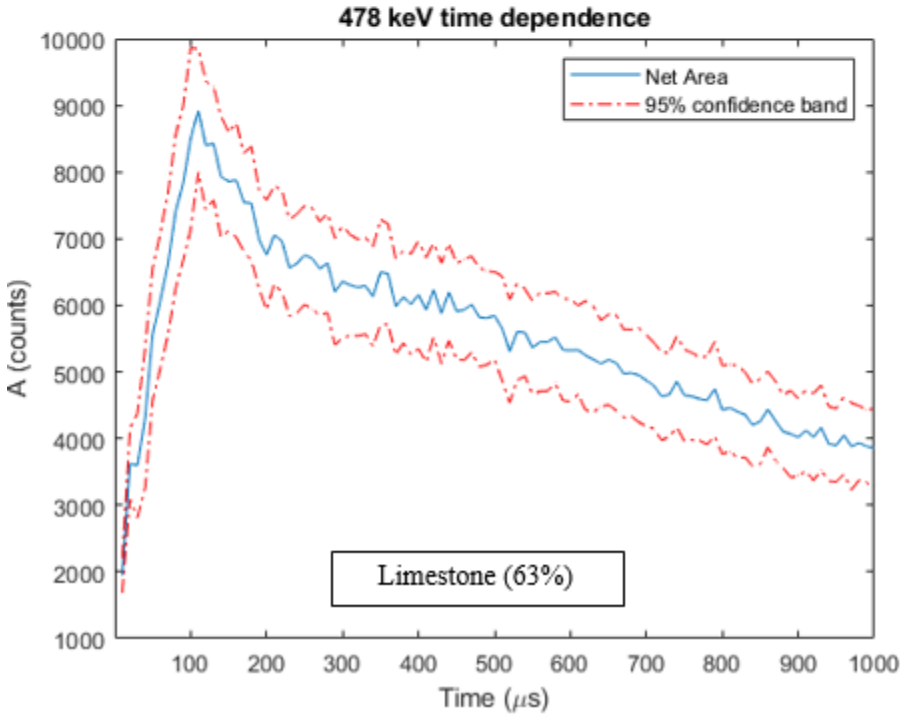

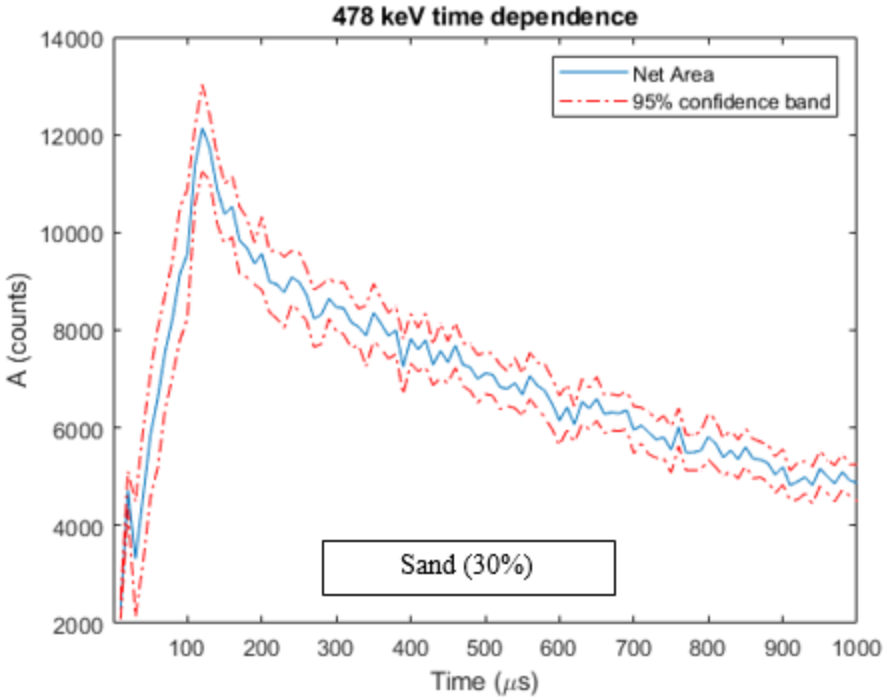
478 keV time dependence
Net Area
95% confidence band
Sand (30%)
A (counts)
Time (μs)
14000
12000
10000
8000
6000
4000
2000
100
200
300
400
500
600
700
800
900
1000

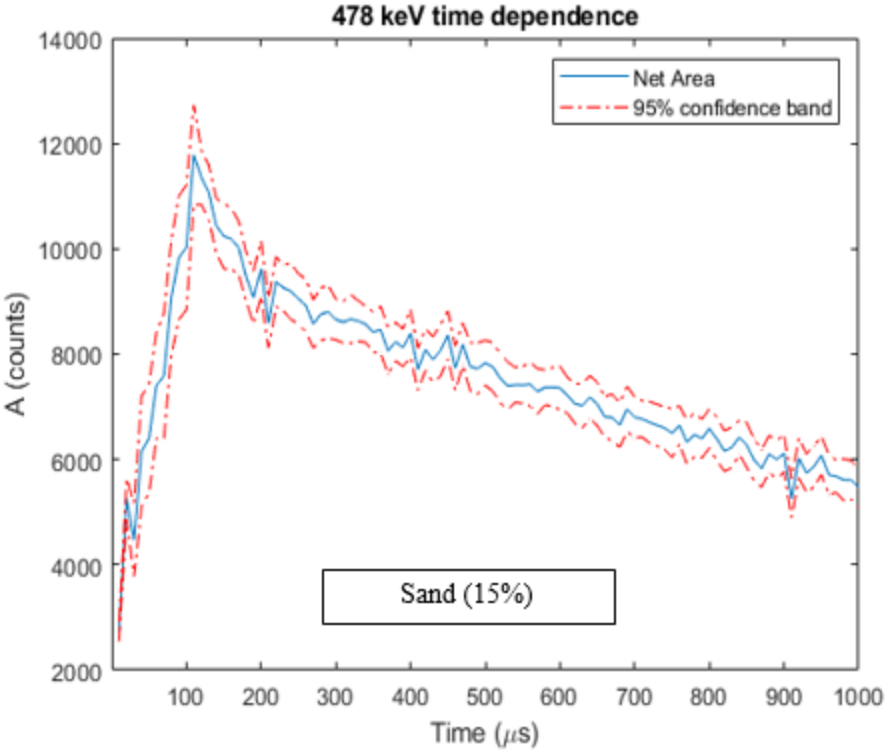
478 keV time dependence
Net Area
95% confidence band
Sand (15%)
A (counts)
Time (μs)
14000
12000
10000
8000
6000
4000
2000
100
200
300
400
500
600
700
800
900
1000

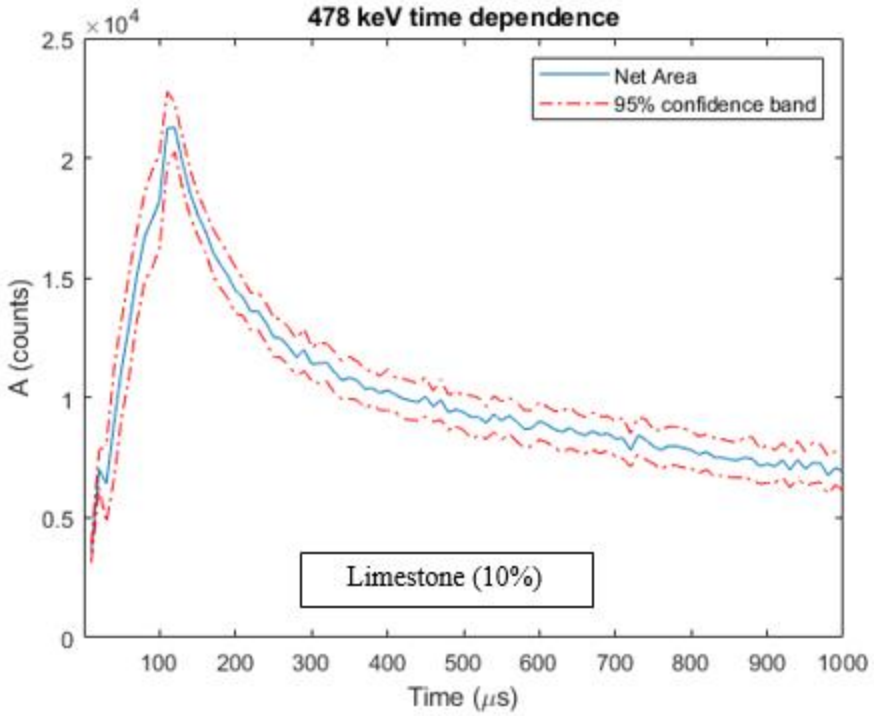
478 keV time dependence
×10^4
2.5
2
1.5
1
0.5
0
A (counts)
Net Area
95% confidence band
Limestone (10%)
100
200
300
400
500
600
700
800
900
1000
Time (μs)

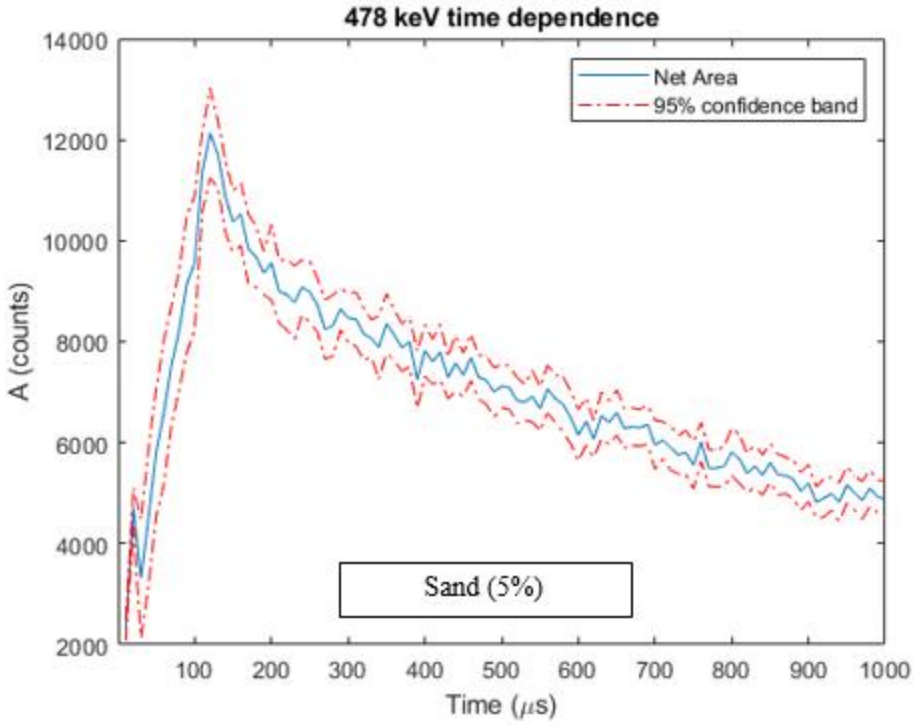
478 keV time dependence
14000
12000
10000
8000
6000
4000
2000
A (counts)
Net Area
95% confidence band
Sand (5%)
100
200
300
400
500
600
700
800
900
1000
Time (μs)

6.6 Appendix F – Time Dependent plots the 511 keV

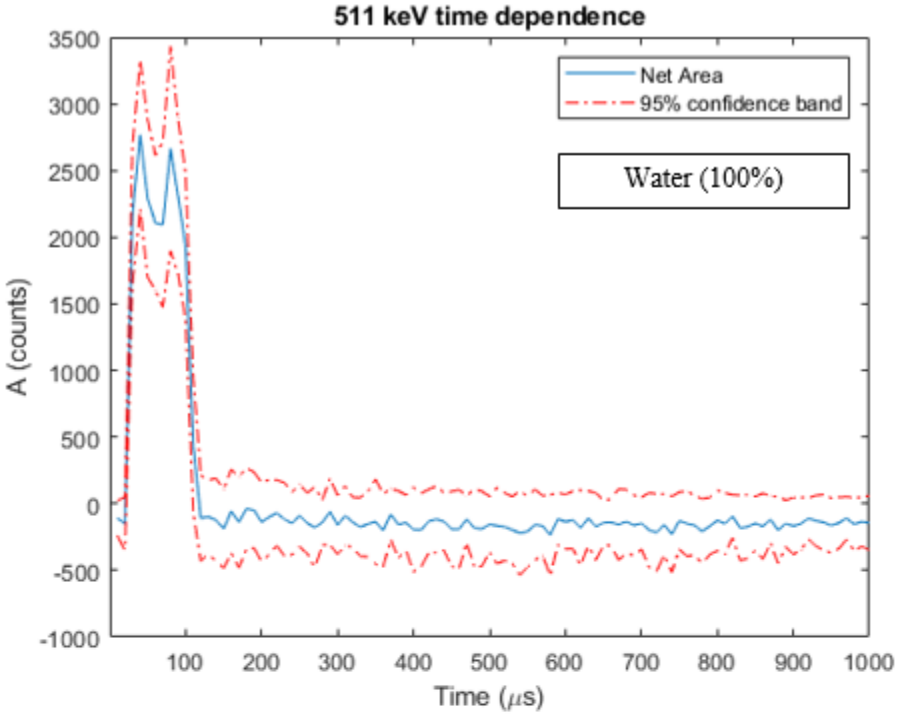

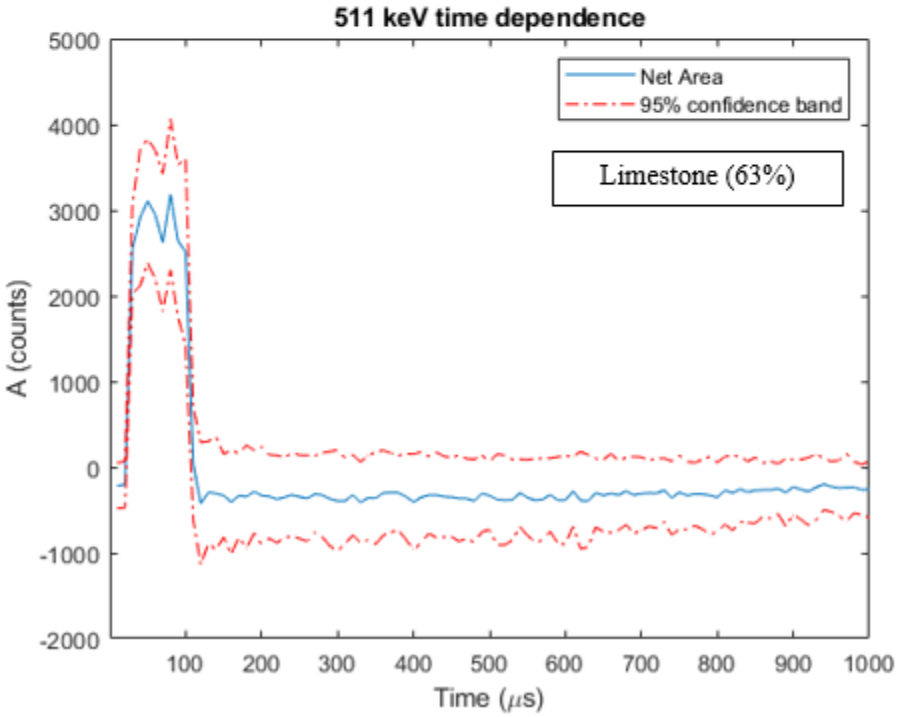

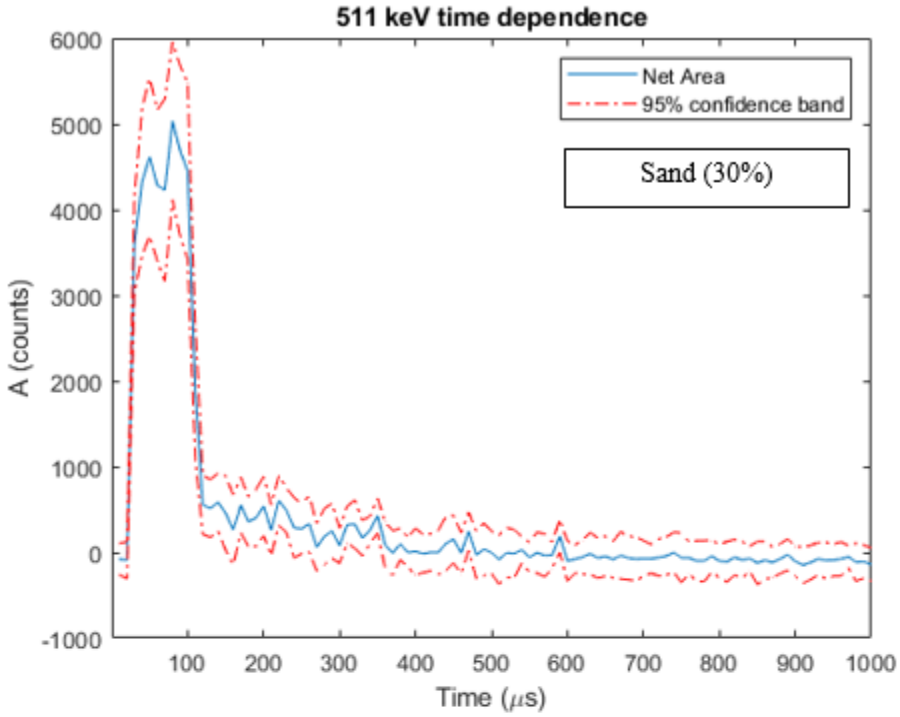
511 keV time dependence
Net Area
95% confidence band
Sand (30%)
A (counts)
Time (μs)
6000
5000
4000
3000
2000
1000
0
-1000
100
200
300
400
500
600
700
800
900
1000

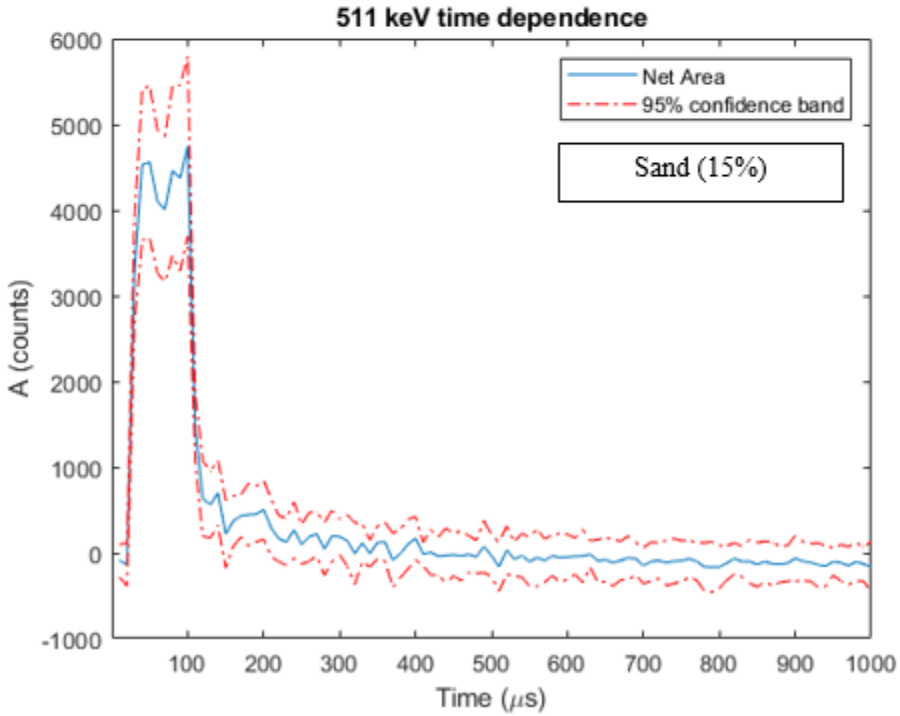
511 keV time dependence
Net Area
95% confidence band
Sand (15%)
A (counts)
Time (μs)
6000
5000
4000
3000
2000
1000
0
-1000
100
200
300
400
500
600
700
800
900
1000

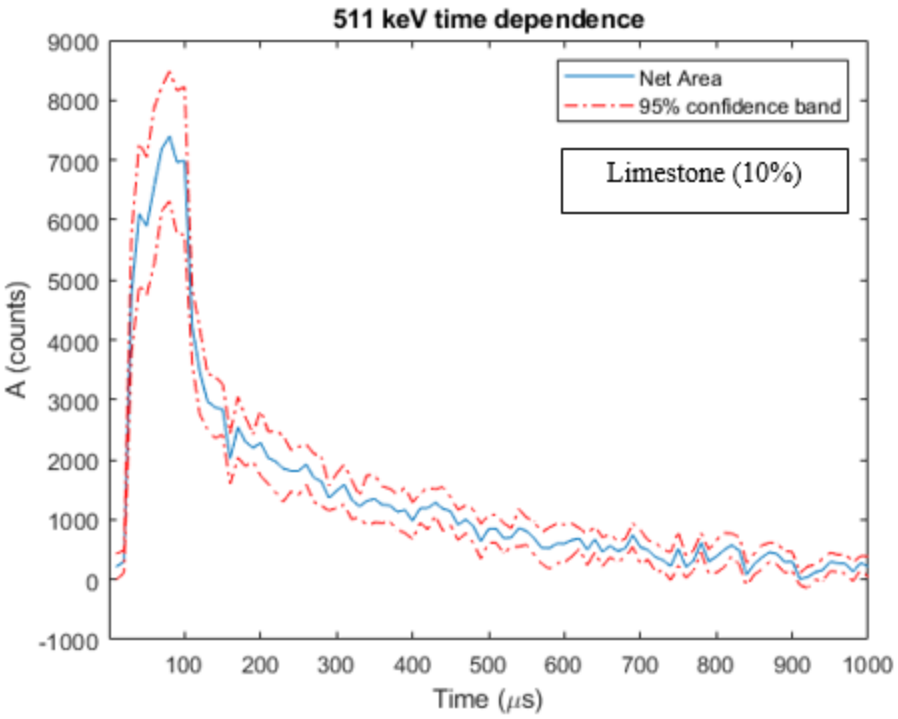
511 keV time dependence
Net Area
95% confidence band
Limestone (10%)
A (counts)
Time (μs)
9000
8000
7000
6000
5000
4000
3000
2000
1000
0
-1000
100
200
300
400
500
600
700
800
900
1000

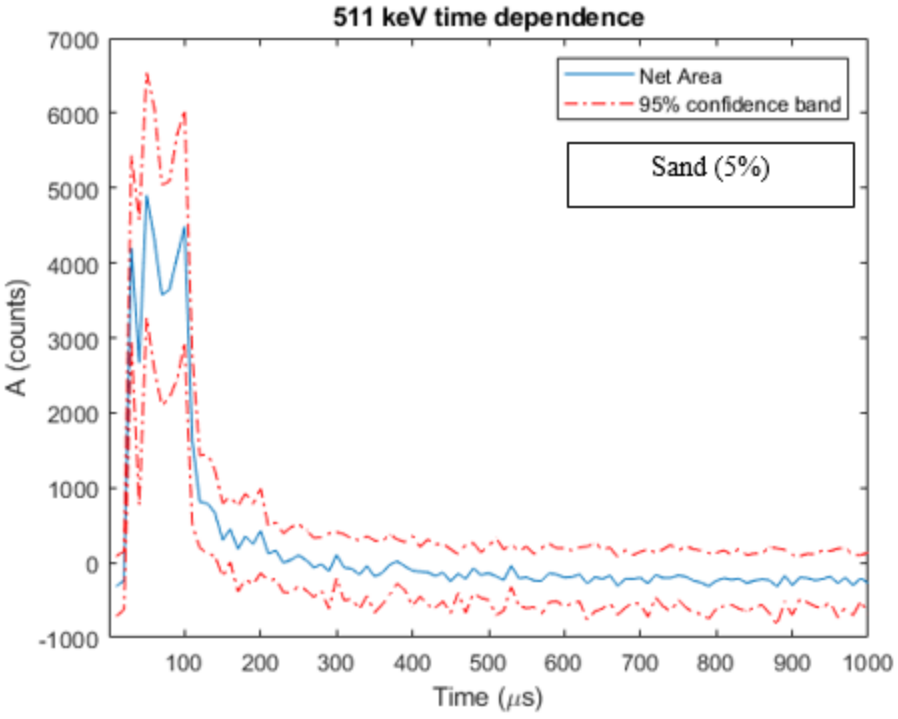
511 keV time dependence
Net Area
95% confidence band
Sand (5%)
A (counts)
Time (μs)
7000
6000
5000
4000
3000
2000
1000
0
-1000
100
200
300
400
500
600
700
800
900
1000

6.7 Appendix G– Time Dependent plots the 511 keV and 478 keV from the 3.6%wt saline sample.

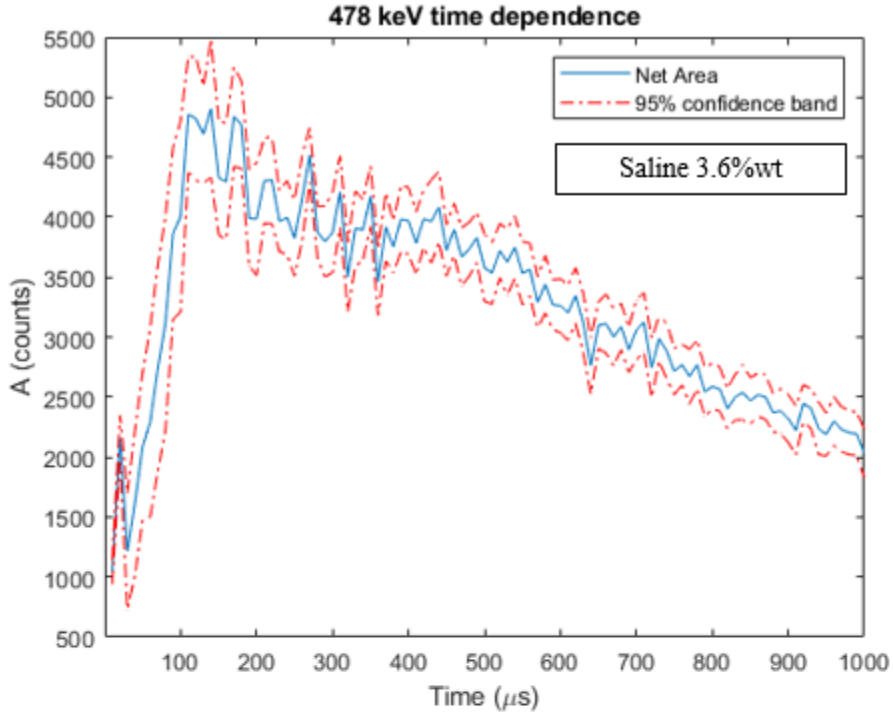

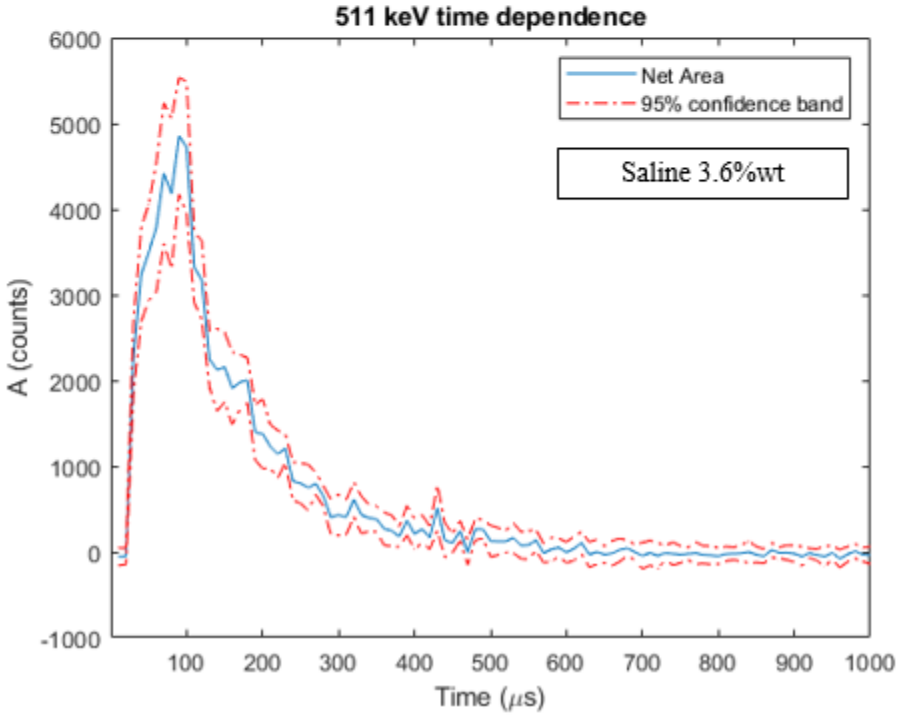

6.8 Appendix H– Signature-Based Radiation Scanning Algorithm

Signature Based Radiation Scanning Method, a template matching technique by calculating a figure of merit ζ_l and $\sigma(\zeta_l)$. ζ_l would take the value approach unity if the drum in question is a match with compliant drum and ζ_l would take a larger value if the drum in question contains impurities or illicit drugs

$$\zeta_l = \sum_{i=1}^{N} \alpha_i \frac{(\beta R_i - S_{li})^2}{\beta^2 \sigma^2(R_i) + \sigma^2(S_{li})}$$

$$\alpha_i = \frac{w_i}{\sum_{i=1}^{N} w_i}$$

$$\sigma(\zeta_l) = 2\left[\sum_{i=1}^{N} \alpha_i^2 \frac{(\beta R_i - S_{li})^2}{\beta^2 \sigma^2(R_i) + \sigma^2(S_{li})}\right]^{0.5}$$

R_i is the measured full-energy peak amplitude signature of the object in question.

i^{th} is the signature of the l^{th} template.

N is the number of photo-peak amplitude signatures.

β is the scaling factor accounting for different measurement time.

$\sigma^2(R_i)$ is the variance of the measured signature i^{th}.

α_i is the normalized weighted factor of each signature i^{th}.

6.9 Appendix I– Sensor 3-D responses, counts with respect to time and energy.

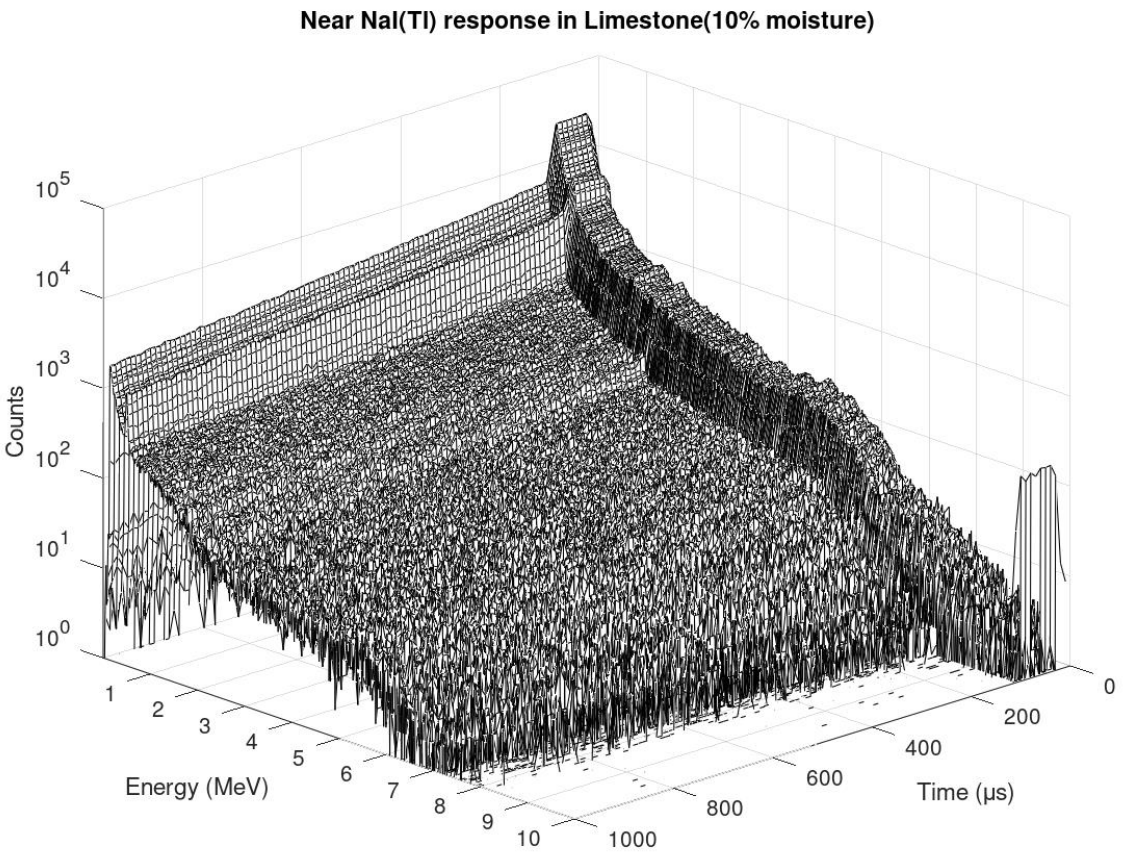

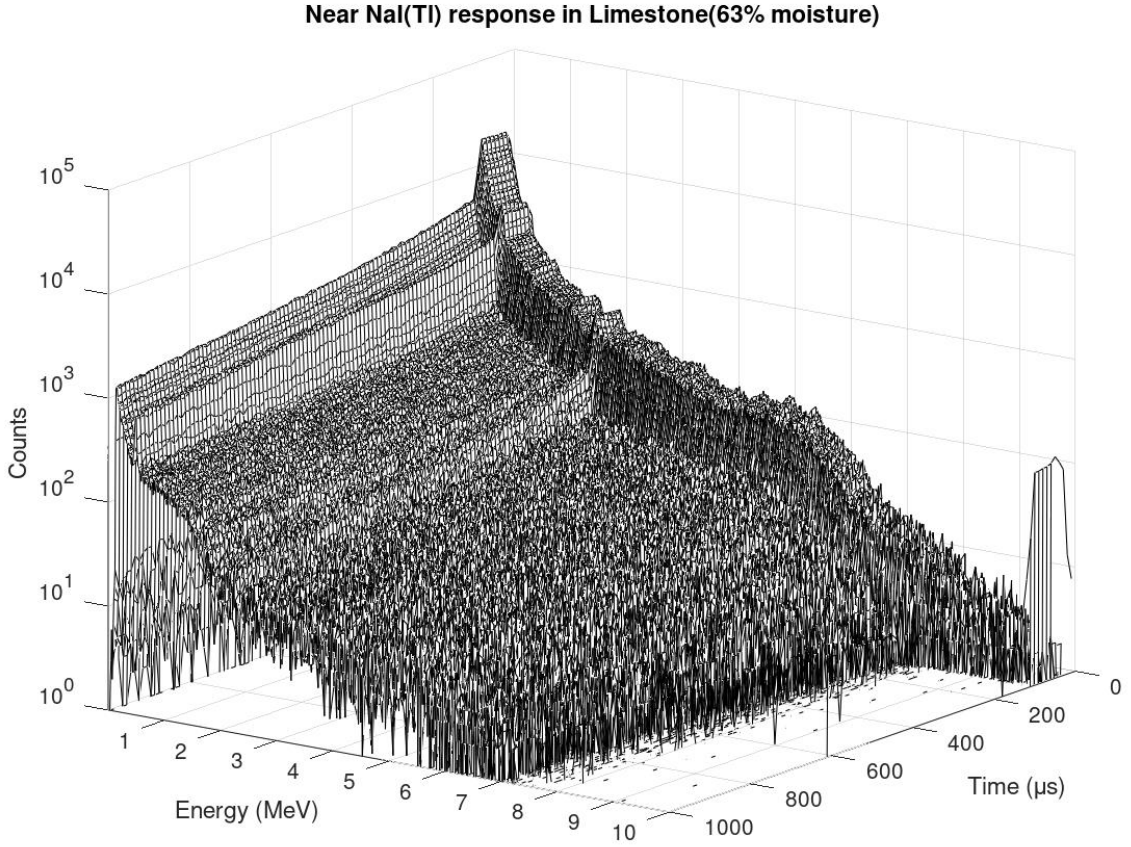
Near NaI(Tl) response in Limestone(63% moisture)
Counts
10^5
10^4
10^3
10^2
10^1
10^0
Energy (MeV)
1
2
3
4
5
6
7
8
9
10
Time (μs)
0
200
400
600
800
1000

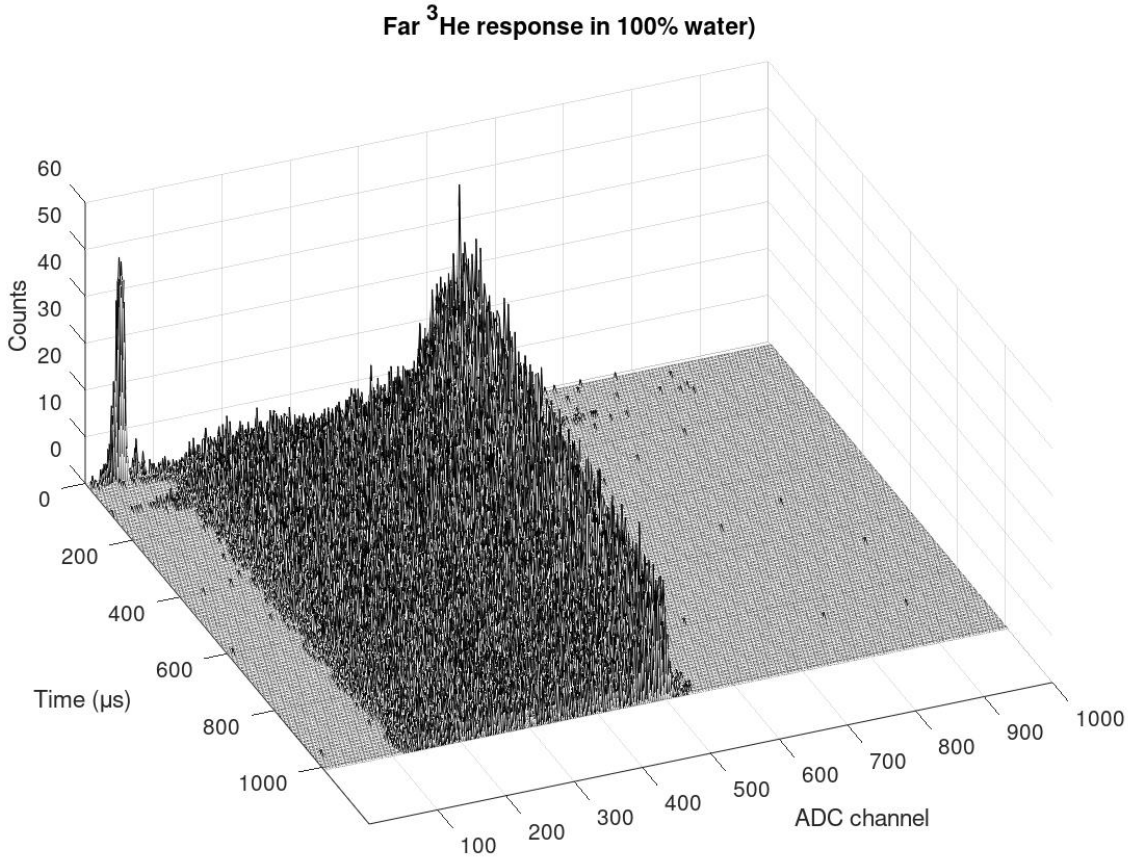
Far 3He response in 100% water)
Counts
60
50
40
30
20
10
0
0
200
400
600
800
1000
Time (μs)
100
200
300
400
500
600
700
800
900
1000
ADC channel

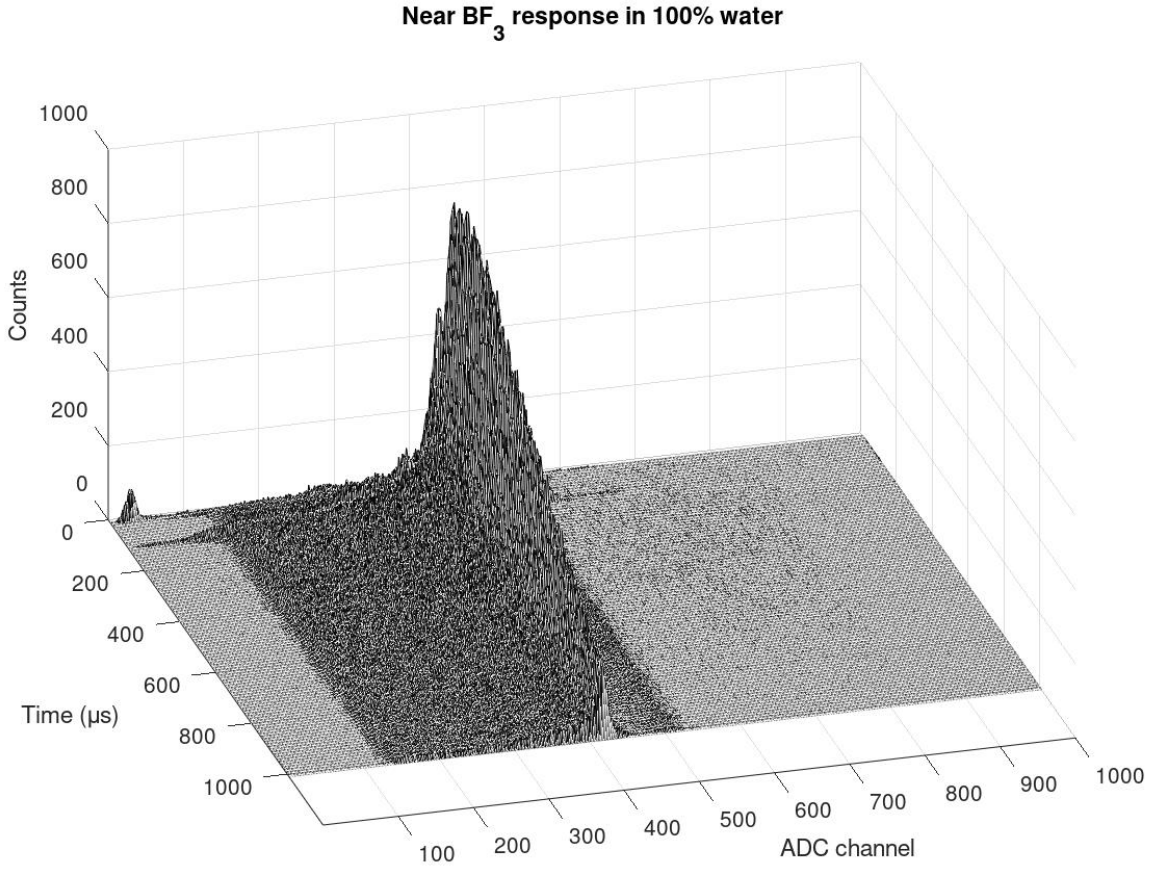
Near BF3 response in 100% water
Counts
1000
800
600
400
200
0
Time (μs)
0
200
400
600
800
1000
ADC channel
100
200
300
400
500
600
700
800
900
1000

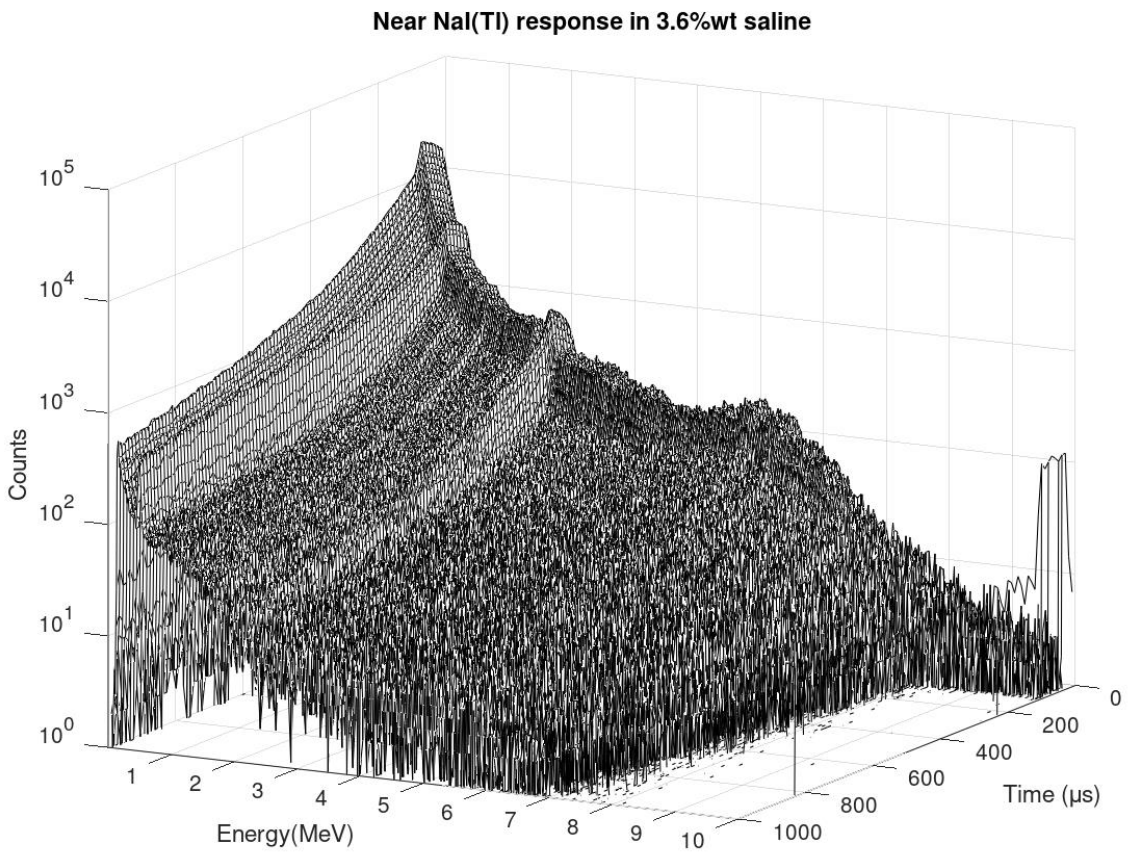
Near NaI(Tl) response in 3.6%wt saline
Counts
10^5
10^4
10^3
10^2
10^1
10^0
1
2
3
4
5
6
7
8
9
10
Energy(MeV)
0
200
400
600
800
1000
Time (μs)

6.10 Appendix J – Prompt Thermal Capture Gamma Rays

Target element	Energies (MeV)	Cross-section (milli-barns)
^{23}Na	0.09	235
	0.50	14.3
	0.781	17.5
	0.869	108
	0.874	76
	2.81	17
	2.86	31
^{35}Cl	0.44	309
	0.508	108
	0.517	**7,580**
	0.786	3,420
	0.788	5,420
	1.16	**8,910**
	1.60	1,210
	1.95	**10,430**
	2.84	1,820
	3.06	1,130
^{1}H	2.22	332
^{12}C	1.26	1.24
	3.68	1.22
	4.95	2.61
^{16}O	0.87	0.17
	1.09	0.16
	2.18	0.16
	3.27	0.035
^{28}Si	1.273	28.9
	2.092	33.1
	3.538	119
	4.933	112
	6.379	20.7
	7.199	12.5
^{40}Ca	0.519	50.3
	2.001	65.9
	2.009	40.9
	3.584	10.0
	3.609	28.3
	4.418	70.8
	6.419	176

6.11 Appendix K -Background radiations

Natural radiations in the pre-background for ^{40}K and ^{208}Tl.

Experiment	Moisture content (%volume)	^{40}K cps and FWHM	^{208}Tl cps and FWHM
Nearly Dry Sand	~0	13.27 (4.75%)	0.6364 (3.74%)
Nearly Dry Limestone	>0	4.747 (4.83%)	1.017 (3.69%)
Partially Saturated Sand	15	11.03 (4.75%)	0.5463 (3.70%)
Fully Saturated Sand	30	10.86 (4.77%)	0.5207 (3.67%)
Fully Saturated Limestone	63	4.077 (4.77%)	0.08971 (3.75%)
Water	100	0.02333 (3.59%)	N/A
Saline (3.6%wt)	98.3	0.02514 (4.52%)	N/A